A HIGH EFFICIENCY AND CLEAN COMBUSTION STRATEGY FOR COMPRESSION IGNITION ENGINES: INTEGRATION OF LOW HEAT REJECTION CONCEPTS WITH LOW TEMPERATURE COMBUSTION

A Dissertation

by

TINGTING LI

Submitted to the Office of Graduate and Professional Studies of
Texas A&M University
in partial fulfillment of the requirements for the degree of

DOCTOR OF PHILOSOPHY

Chair of Committee,	Timothy J. Jacobs
Co-Chair of Committee,	Jerald A. Caton
Committee Members,	Eric L. Petersen
	Mark T. Holtzapple
Head of Department,	Andreas A. Polycarpou

August 2017

Major Subject: Mechanical Engineering

ABSTRACT

Reciprocating engines are pervasively used in the transportation industry. The transportation industry is centered on achieving two important but often conflicting goals: 1) improved energy efficiency and 2) decreased pollution. Advanced engine technology seeks to accomplish these two goals, but there are technical barriers to implementation. For example, implementing an advanced combustion technology known as low temperature combustion (LTC) results in substantially decreased oxides of nitrogen and particulate matter emissions, but increased unburned hydrocarbons and carbon monoxide emissions that can also decrease engine efficiency. This study proposed a technology aiming to develop a solution to achieve improved energy conversion efficiency and lower emissions of internal combustion engines.

The basic idea is to integrate low heat rejection (LHR) concepts with low temperature combustion engine. A comprehensive analysis of engine performance and fuel consumption was conducted to study low heat rejection concepts in the light-duty diesel engine under both conventional and low temperature combustion modes. From most previous studies on LHR diesel engines, thermal-barrier coatings (TBCs) have been recognized as a conventional way to insulate engine parts. The LHR concept proposed in this study, however, is realized by altering engine coolant temperature (ECT). In previous experiments, the studied engine was overcooled to low ECTs and then increased to 100˚C in an effort to get trend-wise behavior without exceeding safe ECTs. This study uses a 1-D engine simulation of the conventional multi-cylinder, four-

stroke, 1.9-L diesel engine operating at 1500 rpm to examine the engine performance and emissions at different ECTs. From the comparative study between conventional-LHR and LTC-LHR modes, it is found that implementing LHR yields more significant improvements in fuel conversion efficiency with LTC mode than it does for the conventional mode, pointing to a higher sensitivity to variations in ECT. The potential reasons causing the difference in engine performance are addressed mainly by comparing the effects of ECT on the combustion phasing between two modes. The results indicate that the integration of LHR with LTC leads the phasing of combustion toward favorable changes, which partly contributes to the significantly improved efficiency.

DEDICATION

To Mom, Dad, and the most inspirational band Radiohead

ACKNOWLEDGEMENTS

After a beautiful and intensive period of three years and seven months, today is the day: writing this note of thanks is the finishing touch on my dissertation. One of my favorite "funny translations" of PhD is "Probably hard to Describe," and that is how I feel about my PhD journey at this moment. Once the journey is over you will not remember how you made it through, how you managed to survive. But one thing is certain. When you come out you are not the same person who walked in. So, I would like to reflect on the people who supported and helped me throughout this personal transmutation and refinement.

I would first like to thank my committee chair, Dr. Tim Jacobs, for all of his encouraging guidance. Sometimes I did think that he is too supportive as an advisor to be true, he continually offered me good opportunities to discover the nature of research and possibilities of future career. He also convincingly conveyed a spirit of professionalism in regard to mentoring.

I also want to particularly thank my committee co-chair, Dr. Jerald Caton, who has provided me with great support since I came to Texas A&M University. He also opened up the door of my studying with internal combustion engine. I really appreciate all his contributions of ideas to make all this happen. My committee members – Dr. Mark Holtzapple and Dr. Eric Petersen – are thanked for their assistance and efforts in supporting this research.

I am thankful for the opportunity to work with my lab mates, former and present, in the AERL group. Jiafeng Sun, Jue Li, Cole Frazier, and Tim Kroger are particularly thanked for their assistance in the experimental tasks.

I am forever grateful for my amazing parents. Their open-mindedness helped me understand the value of adventure, and their patience and love have given me the courage to overcome the obstacles, fears, and confusions all along the way. Special thanks go to Bo, who saw the fire in my weird little world, and his sincerity always inspires me to dig into the invincible essence and magic of life.

CONTRIBUTORS AND FUNDING SOURCES

Contributors

This work was supported by a dissertation committee consisting of Dr. Tim Jacobs (chair), Dr. Jerald Caton (co-chair), Dr. Eric Petersen of the Department of Mechanical Engineering and Dr. Mark Holtzapple of the Department of Chemical Engineering.

The experimental data analyzed for Chapters 4 and 5 were measured by Mr. Michael Penny, former student of Advanced Engine Research Laboratory, Texas A&M University. The injection rate maps shown in Chapter 3 were provided by Dr. Stephen Busch, researcher at Sandia National Laboratories.

Funding Sources

This work was supported by National Science Foundation (Award #1343255) and General Motors Research & Development.

NOMENCLATURE

A	Cross-sectional flow area
A_s	Heat transfer surface area
a	Chen & Flynn model constant
A_1	Activation temperature multipliers for N_2 oxidation
A_2	Activation temperature multipliers for N oxidation
A_f	Soot model constant
A_c	Soot model constant
B_m	Spalding mass transfer number
B	Cylinder bore
b	Chen & Flynn model constant
B1090	Burn duration of 10-90% mass fraction burned
C_p	Pressure loss coefficient
C_f	Skin friction coefficient
C_d	Nozzle discharge coefficient
C_{ent}	Entrainment rate multiplier
C_{pm}	Premixed combustion rate multiplier
C_{df}	Diffusion combustion rate multiplier
C_{ign}	Ignition delay multiplier
C_{ign2}	Ignition delay constant dependent on the fuel
C_{ign3}	Ignition delay constant dependent on the apparent activation energy
C_1	Woschni model constant
C_2	Woschni model constant
C'	Friction model constant

C''	Friction model constant
C'''	Friction model constant
c	Chen & Flynn model constant
$c_{p,c}$	Heat capacity of coolant
c_v	Specific heat at constant volume
c_p	Specific heat at constant pressure
$c_{p,d}$	Specific heat capacity of the droplet
CA10	Crank angle at 10% of mass fraction burned
CA50	Crank angle at 50% of mass fraction burned
D	Equivalent diameter
d	Chen & Flynn model constant
dx	Length of mass element in the flow direction (discretization length)
d_n	Nozzle diameter
e	Total specific internal energy (internal energy plus kinetic energy)
EVC	Exhaust valve close
EVO	Exhaust valve open
F_1	Oxidation rate multiplier
F_2	Oxidation rate multiplier
F_3	Oxidation rate multiplier
H	Total specific enthalpy, $H = e + p/\rho$
h	Heat transfer coefficient
$\Delta H_{v,d}$	Latent heat of vaporization of the droplet
h_c	In-cylinder heat transfer coefficient
h_{exh}	Enthalpy of exhaust gas
h_{air}	Enthalpy of air

h_{fuel}	Enthalpy of the fuel
h_{02}	Stagnation enthalpy at compressor exit
h_{01}	Stagnation enthalpy at compressor inlet
IVC	Intake valve close
IVO	Intake valve open
k	Kinetic rate constant
k_1	Reaction rate constant of extended Zeldovich mechanism
k_2	Reaction rate constant of extended Zeldovich mechanism
k_3	Reaction rate constant of extended Zeldovich mechanism
k_A	Rate constant of Nagle & Strickland-Constable model
k_B	Rate constant of Nagle & Strickland-Constable model
k_T	Rate constant of Nagle & Strickland-Constable model
LHV	Lower heating value
k_Z	Rate constant of Nagle & Strickland-Constable model
m	Mass
$\dot{m}$	Boundary mass flux into the discretized volume, $\dot{m} = \rho A u$
m_{inj}	Initial mass of injected fuel packet
m_d	Mass of the droplet
m_s	Mass of soot, vapor
m_{sf}	Mass of formed soot
m_{sc}	Mass of oxidized soot
m_{fg}	Mass of fuel vapor
$\dot{m}_{air}$	Mass flow rate of air
$\dot{m}_{exh}$	Mass flow rate of exhaust gas
$\dot{m}_f$	Mass flow rate of injected fuel

$\dot{m}_{cool}$	Mass flow rate of coolant
$m_{f,cv}$	Mass of fuel burned during the constant volume process
m_f	Total mass of the burned fuel
MFB	Mass fraction burned
N	Crankshaft rotational speed
$[O_2]$	Oxygen concentration
p	Pressure
Δp	Pressure difference
p_r	Cylinder gas pressure at intake valve closing
p_m	Motored cylinder pressure
$p_{\max}$	Peak in-cylinder pressure
p_{o_2}	Partial pressure of the oxygen
P_1	Cylinder pressure at IVC
P_5	Cylinder pressure at EVO
Q_c	Convective heat transfer
Q_e	Heat evaporated from the droplet
$\dot{Q}_{cool}$	Heat losses to the coolant
$\dot{Q}_{unac}$	Unaccounted energy
$\dot{Q}_{HT}$	In-cylinder heat transfer rate
Q_{hv}	Reaction heat of fuel
R	Gas constant
r_c	Compression ratio
s	Spray penetration length
Sh	Sherwood number for mass transfer
$\overline{S}_p$	Mean piston speed

SFC	Specific fuel consumption
t	Time
t_b	Spray breakup time
t_0	Time of the start of injection
t_{ign}	Time of the start of combustion
τ_{ign}	Ignition delay
T_{wall}	Wall temperature
T_d	Temperature of the droplet
T_g	Temperature of the hot entrained gas
T	Bulk gas temperature
T_r	Cylinder gas temperature at intake valve closing
T_b	Temperature of burned zone mixture
T_e	Coolant temperature at radiator exit
T_i	Coolant temperature at radiator inlet
T_1	Gas temperature at the start of compression stroke in an ideal dual cycle
T_2	Gas temperature at the end of compression stroke in an ideal dual cycle
u	Velocity
u_{inj}	Spray tip velocity
V	Volume
V_{cyl}	Cylinder volume
V_d	Displaced volume
V_r	Cylinder volume at intake valve closing
VE	Volumetric efficiency
v_1	Specific volumes at the start of compression stroke in an ideal dual cycle
v_2	Specific volumes at the end of compression stroke in an ideal dual cycle

w	Average cylinder gas velocity
W_{tf}	Friction work per cycle
$\dot{W}_b$	Brake power
$\dot{W}_{i,net}$	Net indicated power
$W_{i,net}$	Net indicated work
W_f	Friction work
W_C	Compressor work
x_r	Residual gas fraction
ρ	Density
ρ_l	Liquid fuel density
ρ_g	Gas density
ρ_{air}	Air density
α_g	Thermal diffusivity of the entrained gas
λ	Air-fuel equivalence ratio
β	Cutoff ratio of diesel engine
β_{RGF}	Parameter defined in [98]
γ	Ratio of specific heats
ω	Parameter defined in [98]
ϕ	Equivalence ratio
η_c	Carnot efficiency
$\eta_{i,g}$	Indicated fuel conversion efficiency of Otto cycle
η	Fuel conversion efficiency

TABLE OF CONTENTS

Page

LIST OF FIGURES

Page

LIST OF TABLES

Page

1. INTRODUCTION

1.1 Background

1.1.1 High Efficiency Combustion

An internal combustion (IC) engine uses a collection of thermodynamic processes to convert chemical energy of fuel to mechanical work, providing the power to drive vehicle wheels via the drive train in most transportation applications. There is a great need to improve the engine efficiency to decrease consumption of limited fossil fuel energy sources. IC engines distinguish themselves from other types of engines, e.g., heat engines, by the fact that their efficiency is defined by the Carnot efficiency (i.e., $\eta_c = 1 - (T_L / T_H)$). Thus, the potentials of gaining higher efficiency with an IC engine seem to be more plentiful; the IC engine is still limited, of course, by second law considerations such as irreversible processes [1].

The combustion efficiency of a modern IC engine is recognized to be well optimized, with more than 95% of the energy contained within the fuel being released [2], whereas the effective energy delivered to the shaft (termed 'brake work') is usually less than 50% of the input fuel energy. For this to be achieved efficiently, a variety of solutions have been attempted to assess their merits on engine efficiency or fuel economy. This section attempts to introduce some representative developments in improving IC engine fuel conversion efficiency.

The efficiency of an IC engine relates to multiple factors, one of the most important parameters is compression ratio. Increasing compression ratio has long been a strategy employed to improve engine efficiency. In the case of spark ignition (SI)

engine, the compression ratio is typically between 6 and 10. The compression ratio of diesel engines or compression ignition (CI) engines is much higher than SI engine values, which is in the range of 12 to 24 [2]. Diesel engines are generally more efficient than SI engines in large part because of their higher compression ratio helps to extract more of the energy generated from the combustion process before the exhaust stroke. Smith et al. [3] studied the variations in gross indicated efficiency, net indicated efficiency, and brake efficiency of a SI engine as the compression ratio changes, their work shows that increasing the compression ratio from 10 to 13 yields relative increase of 5.1% in brake efficiency, 4.6% in gross indicated efficiency and 4.5% in net indicated efficiency. Funayama et al. [4] reported 8% improvements of gross indicated efficiency in a single-cylinder diesel engine by the combination of higher compression ratio, raising from 17 to 26, and higher specific heat ratio.

It is known that increased ratio of specific heats benefits engine efficiency based on the theoretical Otto cycle (ideal gas constant-volume cycle). Low temperature combustion (LTC) and highly diluted mixture techniques therefore have been exploited to achieve high-efficiency engines. There are a variety of LTC versions achieving the targets of improved fuel economy and clean combustion, which will be further introduced in Section 2.2. The dilution is typically attained by the use of exhaust gas recirculation (EGR), the equivalence ratio is lowered. Consequently, lean combustion leads to higher ratio of specific heats. Furthermore, heat losses transferred from cylinder gases to the walls are also reduced as the combustion temperature decreases under the lean operation. These favorable thermodynamic features contribute to the improvement

in thermal efficiency. Caton [5] presented a thermodynamic engine cycle simulation study on a 5.7-liter automotive engine. The results indicated that lean operation increases the thermal efficiencies due to the associated gains in reduced heat transfer, reduced pumping losses, and the increase of the ratio of specific heats.

Another strategy for a high-efficiency engine, developed by previous researchers, is using multiple injections designed to generate one of the injection pulses near the cool flame region to properly phase the main combustion process. In the work of Osada et al. [6], the use of after-injection and higher EGR rate reduces the flame temperature and suppresses gas temperature near the cavity wall, which confirmed that controlling the flame propagation close to the cavity wall improves the fuel consumption. Nathen et al. [7] also reported that multiple-pulse injection helps in attaining better mixture formation and effective fuel utilization, the main combustion was effectively altered to achieve higher thermal efficiencies by using multiple injections with the last pulse around the formation of the cool flame.

The “adiabatic engine,” or perhaps more appropriately called the low heat rejection (LHR) engine, has been extensively studied since 1980s aiming to improve engine efficiency with partial/complete suppression of heat loss. As a result, the heat transfer from cylinder gases to the combustion chamber walls can be reduced in a low heat rejection engine. As a result, less useful energy is rejected to the engine coolant. In theory, more mechanical work will be extracted from the fuel combustion and therefore improving engine thermal efficiency. More details regarding the development and technical features of LHR engines will be discussed in Section 2.1 along with a different

version of the low heat rejection concept proposed in this study. In addition to the techniques mentioned above, there are still many other technologies developed to improve fuel conversion efficiency, such as increasing boost pressure (e.g., turbocharging) [8, 9], high fuel injection pressure [10], variable valve timing [11, 12], waste energy recovery, and blends of different fuels.

1.1.2 Clean Combustion

As pressure increases to minimize the burden that IC engines place on the environment, improving emission quality has been demanded from IC engines to meet more stringent emission standards. As mentioned in the previous section, diesel engines generally benefit from their inherently superior thermal efficiency because of having higher compression ratios. Nevertheless, the optimal efficiency is still restrained by the emission after-treatment systems to comply with emission regulations. These after-treatment systems such as diesel particulate filters (DPF) and selective catalytic reduction (SCR) systems often incur fuel conversion efficiency penalties [13]. In an effort to develop diesel engine combustion systems for emissions mitigation while minimizing the compromise in fuel conversion efficiency, many compression ignition combustion strategies have been investigated by researchers. The previously discussed LTC strategy is a widely used in-cylinder emission reduction technique. LTC targets to simultaneously reduce NO_x and soot emissions by suppressing the combustion flame temperature.

The contrary effects of changing combustion temperature on NO_x and soot formation cause the difficulty in simultaneously reducing both emissions during the

combustion process. The principal nitrogen oxides pollutants emitted from engine exhaust gases are nitric oxide (NO) and nitrogen dioxide (NO_2). Bowman [14] reported that the chemical equilibrium considerations indicate that the ratio of NO_2 to NO should be negligibly small for typical flame temperatures, and several studies on combustion kinetics [15, 16] also suggest that conversion of NO to NO_2 can be neglected in practical combustion devices. Both Bowman's work [14] and the extended Zeldovich mechanism [17] show the strong dependence of the NO formation rate on the reaction temperature, elevated temperatures and high oxygen concentrations in the post-combustion gases result in relatively high NO formation rates.

Soot formation and oxidation, the difference between which yields "net soot release," are also strongly coupled to reaction temperature. In general, soot is formed from unburned fuel, which nucleates from the vapor phase to a solid phase in fuel-rich regions at elevated temperatures. The soot formation can be depicted by a sequence of five identified processes: pyrolysis, nucleation, coalescence, surface growth, and agglomeration [18]. Solid soot particles can also go back to gas-phase products as oxidation process occurs, which means hydrocarbons are converted to carbon monoxide (CO), carbon dioxide (CO_2), and water (H_2O) in this process. The combination of soot formation and oxidation is termed "net soot formation," and results in how much soot will be emitted as a pollutant. It is reported in [18] that temperature has the greatest effect of any parameter on the sooting process by increasing both the rate of soot formation and oxidation. Unlike the effects of temperature on NO_x, Glassman's study [19] shows that the rate of oxidation increased more rapidly than the rate of formation as

temperature increases, yielding the reduced net soot formation at higher reaction temperatures. Ciajolo [20] further found that in the flame near the low-temperature soot threshold (~1520 K), the polycyclic aromatic hydrocarbons (PAHs), which are considered to be soot precursors, are formed in larger amounts, but low temperature hinders the PAHs coagulation into tar and the subsequent transformation of tar into soot. These results indicate a decrease in soot emissions can be achieved at low temperatures because of the inability of soot formation, which also provides the possibility to simultaneously reduce both NO_x and soot emissions in this combustion region without the commonly existing NO_x–soot tradeoff issue. Soot particles are typically generated in the fuel-rich regions and mostly burnt off at high-temperature near-stoichiometric reaction zones with entrainment of ambient air, whereas the formation of NO_x emissions are produced in the high-temperature zones where soot particles being burnt off [21]. This is the namely the NO_x–soot tradeoff in conventional diesel combustion.

As a tool to help understand the formation of NO and soot in relation to local equivalence ratio (ϕ) and adiabatic flame temperature (T), the T–ϕ map was first introduced by Kamimoto and Bae [22]. Fig. 1 shows the regions of soot formation and NO formation, which clearly indicates that high-level soot formation occurs in the rich parts of combustion. As the ϕ decreases and temperature increases, the combustion moves towards the NO formation region. For conventional diesel engines, combustion largely locates in regions where both pollutant formations intersect with each other. When the temperature is kept below approximately 1650 K, both NO and soot formation areas are completely avoided regardless of the equivalence ratio [23]. This concept is

referred to as the previously mentioned low temperature combustion, the region of which is indicated in Fig. 1.

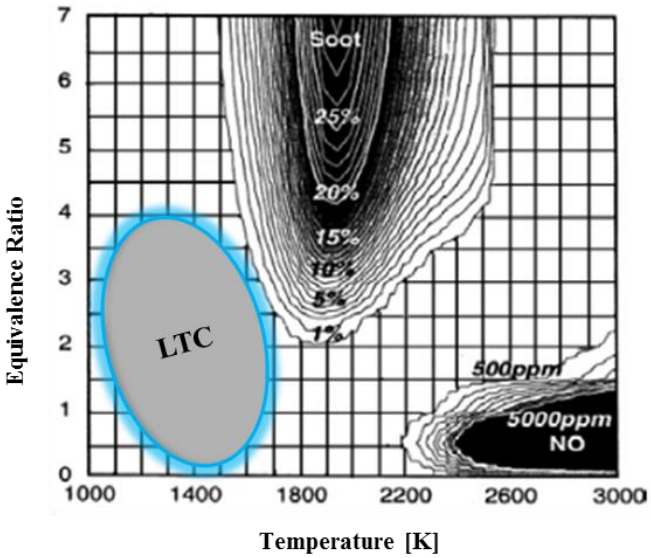

Fig. 1 Formation of NO_x and soot, adapted from [24].

1.2 Objective

As previously mentioned, the focus of this dissertation work is motivated by the desire to address the two barriers concerned with diesel engine, i.e., engine efficiency and combustion emissions, through the integration of LHR and LTC techniques. It has been discussed in Section 1.1 that LHR concepts are designed to improve engine thermal efficiency. Typically, LHR operation promotes the combustion to move toward completeness because of the reduced in-cylinder heat transfer and therefore higher gas temperatures. In the meantime, the additional thermal energy contained in the cylinder is considered to be converted to useful work and leads to better fuel economy. It is also found in conventional LHR engines that the undesirable change in thermodynamic properties, i.e., decreased ratio of specific heats, may not result in as much efficiency

improvements as theoretical gains. In addition, the associated issues with LHR engines also include high NO_x emissions as a result of higher combustion temperatures.
It is thought that coupling LHR with LTC engine provides a solution for these issues. Introducing LTC technique can counteract the undesirable increase in specific heats ratio caused by LHR operation, and low temperature conditions also help in reducing NO_x emissions. As opposed to LHR operation, low temperature combustion is likely to cause relatively higher levels of unburned hydrocarbons; the lower exhaust temperatures also pose another challenge to the after-treatment systems, the inherent catalytic materials cannot be activated if the exhaust gas temperature is lower than the light-off temperature (usually above 200˚C). As a result, the LHR correspondingly helps eliminate these associated problems involved in low temperature combustion. As depicted in Fig. 2, the proposed study of integrating LHR with LTC in a diesel engine attempts to verify an advanced combustion strategy by leveraging the advantages of both techniques while minimizing their unfavorable impacts on engine efficiency and emissions.

The recent experimental investigations of LHR with LTC engines [25-27] also indicate that the combination of LHR and LTC may provide a combustion strategy enabling both high efficiency and clean combustion in light-duty diesel engines. This dissertation work attempts a proof-of-concept that realizes such an LTC-LHR combustion strategy in a compression ignition engine in an effort to improve engine efficiency and reduce combustion emissions.

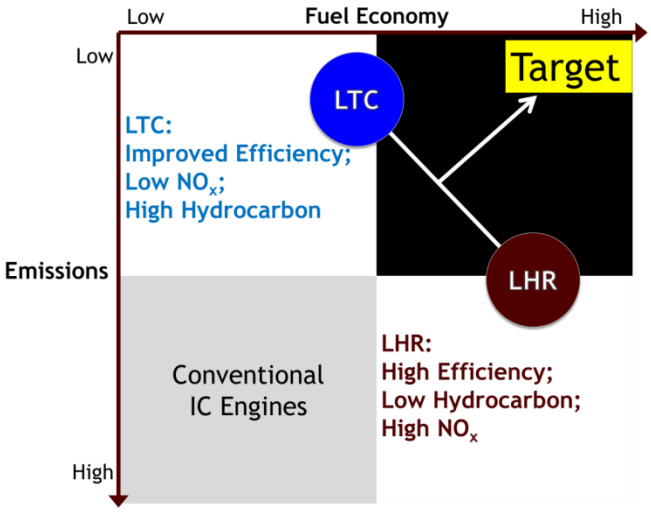

Fig. 2 Illustration of LHR-LTC combustion strategy.

2. LITERATURE REVIEW

2.1 Low Heat Rejection Engines

A number of programs were conducted in the 1980s to develop an "adiabatic engine" [28-30]. As it is stated in Section 1.1, the basic idea of low heat rejection engine is to improve engine efficiency with partial/complete suppression of heat loss. Also, low heat rejection tends to cause the combustion gas temperature to be higher than that of a conventional engine, which in turn promotes chemical oxidation and complete combustion. Theoretically, thermal insulation would bring promising advantages of improved fuel conversion efficiency, higher exhaust gas temperature to support exhaust catalysis, and lowered hydrocarbon (HC) emissions.

Reddy et al. [31] pointed out that all of the simulation work (before 1990) proved the fuel economy superiority of LHR engines over conventionally cooled engines; however, this is not the case with experimental work where the results are mixed. This section will review the previous studies on LHR engines and examine the potential causes for these seemingly contradictory results observed in experimental investigations.

2.1.1 Computational Investigations

Table 1 has summarized the previous simulation studies on the performance of low heat rejection engines compared to conventionally cooled engines, most of which are done on turbocharged diesel engines and some of them are developed for turbo-compound and heat recovery systems. In general, the simulation results consistently show insulated engines having higher thermal efficiency than their baseline engines.

Table 1 Comparison of simulation results between LHR engines and their baseline engines

Investigators	Engine Type	Performance of LHR engines compared to conventionally-cooled engines	
Pawar et al., 2004 [32]	Single-cylinder diesel	Better performance	Insulated engines have higher thermal efficiency than baseline engine for the entire load range.
Islam et al., 1997 [33]	Single-cylinder diesel	Better Performance	A marginal improvement in engine power for all operating conditions.
Miyairi, 1988 [34]	Single-cylinder diesel	Better performance	2.1–2.7% improvement in brake thermal efficiency, which increases as adiabaticity is increased.
Tovell, 1983 [35]	Single-cylinder diesel	Better Performance	7.5% and 4.6% improvement in fuel economy for fully-insulated engine and partially insulated engine, respectively.
Morel et al., 1986 [36]	Single-cylinder diesel	Better Performance	10.6% and 6.3% better brake thermal efficiency for superinsulated engine and PSZ insulated engine, respectively.
Savliwala et al., 1986 [37]	Six-cylinder diesel	Better Performance	Lower BSFC for insulated engine, LHRE-EERS combination would yield much more improvements.
Gatowski et al., 1987 [38]	Six-cylinder diesel	Better Performance	6% and 13% better fuel economy for LHR turbocharged engine and LHR turbocompounded engine, respectively.
Sharma et al., 1990 [39]	Diesel	Better performance	Lower ISFC for PSZ coated engine, turbocompound-LHR configuration gained much more improvements.
Kamo et al., 1984 [40]	Diesel	Better Performance	4% fuel consumption improvement with insulated turbocompound engine and 2% in turbocharged configuration.

Pawar et al. [32] simulated a single-cylinder LHR diesel engine insulated by two different thermal insulating materials, partial stabilized zirconia (PSZ) and silicon nitride. The thermal efficiency of LHR engine having 1-mm and 0.5-mm zirconia coating is higher by about 3.3–6.4% and 2.6–4.9% respectively than the baseline engine. Islam et al. [33] used a computation simulation model to develop parametric studies on a

single cylinder direct injection engine for different fuel operations. In the low heat rejection model, 2-mm insulation resulted in 2.89% improvement in power output and 50% reduction in soot emissions, along with 9.5% increase in NO_x emissions. Similar studies for turbocharged LHR engines are also reported in [34-36] showing 2–10% improvements in thermal efficiency.

Savliwala and Hakim [37] reported a performance assessment study of the combination of low heat rejection engine (LHRE) and exhaust energy recovery system (EERS). Three different levels of insulation and additional EER via turbocompounding, bottoming cycle and both were investigated. The results indicate that insulation can improve the brake specific fuel consumption (BSFC) for all considered LHRE-EERS configurations. A conventionally cooled engine can attain 3.4% and 5.0% improvement in BSFC for insulation levels of 40–50% and 80–100%, respectively. Gatowski et al. [38] analyzed the fuel economy for different engine configurations with using computational simulation, a water-cooled turbocharged diesel engine, a LHR turbocharged diesel engine and a LHR turbocompounded engine. The addition of an idealized power turbine increased the combined schedule fuel economy by 7% relative to the turbocharged LHR engine and by 13% relative to the water-cooled engine. Sharma and Gaur [39] examined the fuel economy of naturally aspirated LHR engines using diesel cycle simulation, the results showed that the PSZ coated engine gained 7.4% improvement in indicated specific fuel consumption (ISFC) under naturally aspirated (NA) conditions. A turbocompound-LHR configuration showed about 18.4% improvement in BSFC over NA-LHR mode and 8.1% improvement in BSFC over

turbocharged-LHR configuration. Hoag et al. [41] developed the diesel cycle simulation program and demonstrated the feasibility of the adiabatic engine. For the fully insulated case, the results indicated an approximately 4% and less than 2% fuel consumption improvements in turbocompound configuration and turbocharged configuration, respectively.

2.1.2 Experimental Investigations

Contrary to the simulation studies consistently showing better performance in LHR engines, the experimental results show to be somewhat mixed. Likewise, a summary of past experimental studies performed to evaluate LHR engines is shown in Table 2.

Cole and Alkidas [42] designed an air-gap-insulated piston to study the low heat rejection in a single-cylinder diesel engine. The LHR piston resulted in total coolant heat rejection reduction ranging from 3% at light load to 5–7% at full load, and reductions in HC, CO, and smoke emissions, along with a general increase in the NO emissions. Significant improvement in BSFC was observed at light loads only. Schwarz et al. [43] designed a LHR engine configuration having zirconia-coated piston and without liner cooling, the performance results were mixed. At full load conditions, 3% improvement and 5% deterioration in ISFC were observed at high speeds and low speeds, respectively. At part load conditions, the LHR engine showed to have equal ISFC at high speed compared to the baseline engine, but higher ISFC at low and mid speeds. Woschni and Spindler [44] developed a modified equation to calculate the heat transfer of an insulated diesel engine with measured combustion chamber wall temperatures, showing that

insulation of combustion chamber yields savings in fuel consumption only at low load. Because the heat transfer coefficient rises rapidly at higher surface temperatures, which limited the beneficial effects on fuel consumption of combustion chamber insulation.

Table 2 Comparison of experimental results between LHR engines and their baseline engines

Investigators	Engine Type	Performance of LHR engines compared to conventionally-cooled engines	
Cole et al., 1993 [42]	Single-cylinder diesel	Mixed results	A significant improvement in BSFC at light loads only.
Schwarz et al., 1993 [43]	Single-cylinder diesel	Mixed results	Higher ISFC at low speed conditions; better or equal ISFC at high-speed conditions.
Woschni et al., 1988 [44]	Single-cylinder diesel	Mixed results	Reduced fuel consumption only at low load.
Alkidas, 1989 [45]	Single-cylinder diesel	Better performance	The fuel consumption of uncooled engine was equal or superior to that of cooled engine.
Mahmoud et al., 1992 [46]	Single-cylinder diesel	Better performance	11% improvement in brake thermal efficiency for engine having ceramic-topped piston.
Kawamura et al., 1996 [47]	Single-cylinder diesel	Better performance	5–10% lower fuel consumption for insulated engine having pre-combustion chamber.
Kamo et al., 1999 [48]	Six-cylinder diesel	Better performance	5–6% improvement in fuel conversion efficiency at all speeds and loads.
Modi et al., 2010 [49]	Multi-cylinder diesel	Better performance	5–10% lower SFC for insulated engine using pure diesel fuel.

Alkidas [45] analyzed the performance and emissions characteristics of a thermally insulated diesel engine having an optimized injector-tip configuration, the results appear to disagree with the hypothesis of [44]. Alkidas compared the uncooled and water-cooled engines with equal airflow and brake mean effective pressure (BMEP).

It was found that the fuel consumption of the uncooled engine was superior or at least equal to that of the water-cooled engine, and no performance deterioration in uncooled engine was observed at high loads. The performance tests conducted by Mahmoud et al. [46] also show that ceramic-topped piston can improve the brake thermal efficiency by 11% over that of the baseline engine having ordinary aluminum-alloy piston. Similar to the emission results reported in [42], the carbon monoxide emissions were found to be reduced by 15% in LHR engine while the NO_x increased up to 100%. LHR engines having better fuel economies are also demonstrated in [47-49].

There could be a number of possible causes to explain those seemingly contradictory results reported in the past experimental studies on LHR engines, some of which may result from the operational constraints involved in experimental investigations. Namely, the investigations were not always conducted at the same operating conditions. In the engine experiments, it is not easy to maintain some operating parameters (e.g., air/fuel ratio, peak conditions) constant in both the LHR engine and its baseline engine. Maintaining the same operating conditions, however, can be very easily set up in a simulation program.

In addition, the interactions among various engine parameters could also likely be a factor influencing the conclusions on their comparative studies. For instance, reduced heat rejection can negatively affect the volumetric efficiency because of the higher operating temperature conditions where the hotter cylinder walls and residual gas decrease the density of the inducted air. In addition, reported work shows that the resulting high gas temperatures in LHR engines yield lower values of the specific heats

ratio, which cause less effective conversion of thermal energy to work [50-52]. Load condition [44, 48] and physical properties of the insulation materials [53] also have impacts on the fuel conversion efficiency of LHR engines. Nevertheless, the previous studies on LHR engines did consistently show that insulation helps in reducing HC and CO emissions, and a general increase in NO_x emissions.

2.1.3 Proposed LHR Concept

Most low heat rejection engines employ thermal barrier coatings (TBCs) to increase the thermal resistance of surfaces interacting with the mixture gas. The conflicting results discussed in the previous section are mostly concluded based on ceramic-coated engine research. A different means of achieving LHR engine used in this study is by varying engine coolant temperature.

It is expected that the heat rejection to the coolant can be altered by changing engine coolant temperature, causing differing temperature differences between the mixture gas and the wall. Similar strategies for investigating heat transfer of internal combustion engines have been reported elsewhere [54-56]. Hoag [54] analyzed the heat flux through the cylinder wall for different water/ethylene glycol coolant temperatures. Torregrosa et al. [55] presented an experimental study on the influences of the coolant temperature and inlet charge temperature on diesel engine performance, for coolant temperature over a range between 65°C and 97°C. Burke et al. [56] investigated how the emissions and fuel economy vary with coolant temperature ranging from 50°C to the maximum 98°C. From the perspective of an experimental study, there are some technical difficulties in operating the engine at higher ECTs. For example, nucleate boiling, a type

of boiling heat transfer, may happen when the wall surface temperature goes beyond the coolant saturation temperature, which increases the heat energy rejected to the coolant.

So far, relatively little attention has been devoted to investigating the possibility of LHR engines with the approach of altering coolant temperature, which does not require significant modifications of the engine configuration. This study seeks to explore the feasibility of LHR concept by altering ECT, and to assess the potential improvements in engine performance for a light-duty diesel engine. Another problem to be addressed is to correlate various engine parameters including volumetric efficiency, combustion and heat transfer to fuel conversion efficiency by the use of the simulation.

2.2 Low Temperature Combustion Engines

Highly diluted charge and premixed charge are usually implemented to reduce emissions. Dilution is typically realized by lean operation or the use of high-level exhaust gas recirculation (EGR), the common characteristic of these techniques is decreased flame temperature. In an effort to reduce NO_x and soot emissions while maintaining high thermal efficiency, many advanced compression ignition combustion strategies have been proposed by previous researchers. According to different types of methods, the LTC techniques can be generally divided into three classifications, which are homogeneous charge compression ignition (HCCI), premixed charge compression ignition (PCCI), and reactivity controlled compression ignition (RCCI). The principles of HCCI, PCCI, and RCCI will be reviewed along with their typical features in this section.

2.2.1 Homogeneous Charge Compression Ignition

As the name implies, the fuel-air charge in HCCI engines is premixed like spark ignition engines prior to being compression ignited. The well-mixed charge, however, is highly diluted either by operating with a substantially lean equivalence ratio or through the use of high levels of EGR diluting the oxygen in the incoming air flow. The combustion temperatures are consequently lowered which helps in reducing NO_x emissions; meanwhile, the homogeneous-like mixture hinders the formation of soot. Although the engine is operating at low temperature conditions, the high compression ratio and lack of throttling losses offer HCCI engines the ability to achieve high efficiencies comparable with conventional diesel engines. These features make the HCCI engine one of the early LTC concepts attracting attention; beyond that, substantial research and development efforts on HCCI were conducted with using different fuels in addition to usual diesel fuel [57-59]. Christensen et al. [57, 58] studied a variety of fuels, including pure diesel fuel, iso-octane, *n*-heptane, gasoline, and mixtures of gasoline and diesel fuel. Their experimental results show that almost any liquid fuel can be used in a HCCI engine using variable compression ratio. Yao et al. [59] investigated the controlling strategies of HCCI fueled by dimethyl ether (DME) and methanol, ignition timing and combustion duration were regulated in their study by adjusting the DME percentage and EGR rate. Compared to diesel fuel, gasoline and iso-octane have relatively higher volatility, which is advantageous for mixture formation; the inherent two-stage ignition process of diesel fuel makes it difficult to prevent early auto-ignition during the premixing [60].

It can be inferred from the features discussed above that HCCI is indeed thermodynamically attractive, while there are a few technical hurdles with extended application of HCCI engines. Given that HCCI uses a premixed charge that is compression ignited, heat release rates are typically more rapid than in conventional diesel engines so that the combustion approaches an almost constant-volume combustion [13]. Such high heat release rates and pressure rise rates restrict the extension of HCCI engine operating map to higher loads due to the needs of avoiding ringing [61], which is the occurrence of abnormal engine noise resulting from pressure waves in extreme cases. Another controllability challenge of HCCI engines is the ignition timing control. Unlike conventional SI engine having the spark timing or CI engine having the injection timing to aid in dictating the start of combustion, the premixing process and subsequent auto-ignition timing can be affected by a variety of factors in real HCCI engines, which leads to the difficulty in the control of combustion phasing. These issues have prompted a trend in the study on premixed charge compression ignition (PCCI).

2.2.2 Premixed Charge Compression Ignition

Similar to HCCI concept, premixed charge compression ignition also aims at a fully premixed and sufficiently lean air-fuel mixture before the start of combustion. The ultimate objective is to suppress the local flame temperature and reduce NO_x emissions. In the meantime, thoroughly mixing air and fuel can avoid forming locally rich regions so that soot formation rates are lowered. The difference between PCCI and HCCI largely lies in the degree of homogeneity of the premixed charge. Fuel is injected very early before top dead center (TDC) in HCCI engines to provide abundant time for air-fuel

mixing, while in the case of PCCI the fuel is injected early during the compression stroke causing minor stratification. In this case, it is possible to realize a sufficient but not excessive separation between the end of injection and start of combustion [62]. Therefore, controlling the combustion phasing is relatively less difficult than in HCCI where the link between injection event and combustion event is lost. One successful control method is the strategy of two separate injections explored by Hasegawa et al. [63] and Kook et al. [64], the basic idea is to achieve premixed mixture by using the first (very early) injection, and then the second injection occurs at the desired start-of-combustion timing to trigger the ignition of premixed mixture.

Operating PCCI at high engine loads, however, is still difficult to realize in that it is, with reasonable effort, not possible to attain sufficiently long ignition delay such that all the fuel has been injected once ignition takes place [62]. Noehre et al. [65] proposed that increasing inlet pressure and use of high EGR rates can broaden the operating range, the reason is that higher in-cylinder pressure at the moment of injection aids in the combination of better fuel vaporization and air entrainment. The PCCI is restricted to low and medium engine loads partly due to the very high pressure rise and heat release rates, which likely cause ringing. Okude et al. [66] combined PCCI combustion with a normal diffusion burn to avoid high pressure rise rates for high loads. Also, this issue could be solved by using fuels having lower cetane number [62].

In addition to solving the NO_x–soot tradeoff, PCCI also improves thermal efficiency because of the reduced combustion duration and lower heat transfer losses. But both HCCI and PCCI combustion generally suffer from high levels of CO and

unburned HC emissions [67, 68], because the long ignition delay likely causes fuel jet impinging on cylinder walls.

2.2.3 Reactivity Controlled Compression Ignition

Reactivity controlled compression ignition (RCCI) concept was proposed to investigate the potential of controlling HCCI and PCCI strategies through varying fuel reactivity. RCCI is also a LTC technology that uses fuel blending with at least two fuels of different reactivity to control combustion phasing and pressure rise rates at both low and high engine loads.

Most HCCI and PCCI researches have been conducted using either neat gasoline or neat diesel fuel, both of which carry the disadvantages for premixed compression ignition operation. The poor auto-ignition qualities of gasoline make it difficult to achieve combustion at low engine loads. Diesel fuel, however, has superior auto-ignition qualities, which also causes concerns with combustion phasing control at sufficiently high loads. Thus, the fuel reactivity can be tailored through fuel blending to create reactivity stratification and therefore accommodate the changes of engine load. Previous studies by Kokjohn et al. [69] demonstrated that the combustion phasing is determined by the zones of reactivity sequentially igniting from the most to least reactive. The process of RCCI generally includes two steps, low reactivity fuel (gasoline) is injected through port into cylinder to form a well-mixed charge, and the high reactivity fuel (diesel) is then directly injected into combustion chamber before the ignition of premixed charge.

Given that RCCI is a variant of premixed compression ignition technology (HCCI and PCCI), many studies have demonstrated that RCCI is a promising combustion strategy for reducing both NO_x and soot emissions but with more efficient control over the combustion process [70-72]. However, similar to HCCI and PCCI engines, CO and unburned HC emissions of RCCI combustion are also found to be significantly higher than in conventional diesel engines [73]. The lower exhaust temperatures with these types of LTC concepts also pose a challenge to the oxidation catalyst of an after-treatment system where the light-off temperatures required by CO and HC emissions treatment are typically higher than 200˚C.

3. ENGINE MODEL DESCRIPTION AND CALIBRATION PROCEDURE

This study is a simulation-based analysis of low heat rejection concepts applied to a low temperature combustion diesel engine, and complements prior experimental studies [25-27]. The work relies mostly on a one-dimensional simulation using a pseudo-predictive combustion approach to predict the engine performance, emissions (mainly NO formation) along with in-cylinder combustion behaviors for a multi-cylinder, four-stroke, 1.9-L diesel engine. This section begins with a brief introduction on prior experimental methodology of LTC-LHR operation, which is followed by the simulation strategy and related modeling descriptions. Then, a systematic calibration procedure will be detailed to show the process of determining model constants.

3.1 Summary on Prior Experimental Study

The test engine for this LTC-LHR study is a four-cylinder light-duty diesel engine, the specifications of which are listed in Table 3. A high-pressure common rail fuel system allows the electronic control of injection timings, cooled EGR system and a variable-geometry turbocharger are used to realize low temperature combustion in this study. More information regarding the measurements and data acquisition has been reported in [25]. The fuel used in the test is standard Diesel #2. Table 4 gives the fuel properties.

A sweep of injection timings and EGR levels were completed by Penny [25-27] to determine the test conditions necessary to attain LTC using PCCI techniques. In general, the LTC was achieved by the use of high-level EGR and retarded injection timing. In this study, conventional combustion mode has no EGR and the LTC mode is

Table 3 Engine specifications

Engine type	DI Diesel Engine
Displaced volume	1.9 L
Bore	82 mm
Stroke	90.4 mm
Connecting rod	145.5 mm
Compression ratio (nominal)	18:1
Number of valves	16
Number of cylinders	4
Exhaust valve open	112° ATDC
Exhaust valve close	356° ATDC
Intake valve open	361° ATDC
Intake valve close	–132° ATDC

Table 4 Summarized properties of Diesel #2 under the study

Density	825.5 kg/m^3
Net Heat Value	43.008 MJ/kg
Carbon (%mass)	85.81
Hydrogen (%mass)	13.41
Viscosity	2.247 cSt
Cetane Number	51.3

[a]Measured or calculated by Southwest Research Institute (San Antonio, TX).

using a high level of EGR (~35%), which is driven by adjusting the turbocharger to its full boost position. Based on previous experimental work on a medium-duty diesel engine, 8˚bTDC and 1.5˚bTDC were chosen for conventional combustion mode and LTC mode, respectively. For each combustion mode, the engine coolant temperature was varied among five values up to the maximum temperature of 100˚C. The coolant temperature ranges from 56.5 to 100˚C at conventional combustion mode, the minimum value is restricted by the amount of heat that can be rejected into the environment. The lowest temperature for LTC mode is relatively higher (75˚C) and is limited by combustion instabilities. The engine was maintained at an operating speed of 1500 rpm,

a rail pressure of 425 bar, and a low load condition of approximately 2 bar BMEP. The test matrix is summarized for clarity in Table 5. Cases 1–5 are conventional combustion mode, and the rest are operated at LTC mode.

Table 5 Summary on operating conditions in the experimental investigations

Parameters	Conventional Mode	LTC Mode
Speed (RPM)	1500	1500
Injection Timing (˚bTDC)	8	1.5
Rail Pressure (bar)	425	425
EGR Level (%)	0	~35
BMEP (bar)	2	2
Fueling Rate (mg/cycle)	~35	~35
ECT (˚C)	**Case #1**: ECT = 56.5	**Case #6**: ECT = 75
	Case #2: ECT = 65	**Case #7**: ECT = 82.5
	Case #3: ECT = 75	**Case #8**: ECT = 90
	Case #4: ECT = 90	**Case #9**: ECT = 95
	Case #5: ECT = 100	**Case #10**: ECT = 100

Although the engine coolant temperature was varied within a small range in this study and substantially higher temperatures would be seemingly desirable to accentuate the effects of LHR, there are some technical difficulties in operating the engine at higher ECTs. For example, nucleate boiling, a type of boiling heat transfer, may happen when the wall surface temperature goes beyond the coolant saturation temperature, which could result in increased heat energy transferred to the coolant. In addition, the operation conditions with ECT beyond 110°C are unlikely to be realized due to the needs of avoiding excessive oil temperature [74]. The thermal stresses must be kept below levels that would cause fatigue cracking on an actual engine. The metal temperature limits are 400°C for cast iron and 300°C for aluminum alloys [2].

3.2 Model Description

The major activities of this model-based work are to develop engine simulations that can provide the capability of exploring the combined LTC-LHR technology on a computational basis. The simulation can vary engine parameters that cannot be adjusted experimentally under the current test bench conditions, such as engine compression ratio and the previously mentioned significantly higher ECTs, etc. In this study, *GT-Power* [75] is the primary tool providing the platform for model-based combustion investigations of the LTC-LHR concept.

In general, the engine simulation software is used to predict engine performance quantities such as airflow, volumetric efficiency, power, torque, fuel consumption, a few types of emissions, in-cylinder gas pressures and temperatures, turbocharger performance, and so on. At its core, the simulation solver is based on the 1-D gas dynamics solution of fully unsteady, nonlinear Navier-Stokes equations, namely the conservation of continuity, momentum and energy equations. All quantities are averages across the flow direction due to the use of 1-D flow model. The conservation equations solved by the engine simulation software [75] are listed below, where the left-hand side represents the derivatives of the primary variables.

Eqs. (1) and (2) are the continuity equation and momentum conservation, respectively. Eqs. (3) and (4) are the energy conservation equations for implicit solver and explicit solver, respectively. The primary solution variables in the explicit method are mass flow, density and internal energy. For implicit method, the primary solution variables are mass flow, pressure and total enthalpy.

$$\frac{dm}{dt} = \sum_{boundaries} \dot{m} \tag{1}$$

$$\frac{d\dot{m}}{dt} = \frac{dpA + \sum_{boundaries} \left(\dot{m}u\right) - 4C_f \frac{\rho u|u|}{2}\frac{dxA}{D} - C_p\left(\frac{1}{2}\rho u|u|\right)A}{dx} \tag{2}$$

$$\frac{d\left(me\right)}{dt} = -p\frac{dV}{dt} + \sum_{boundaries} \left(\dot{m}H\right) - hA_s\left(T_{fluid} - T_{wall}\right) \tag{3}$$

$$\frac{d\left(\rho HV\right)}{dt} = \sum_{boundaries} \left(\dot{m}H\right) + V\frac{dp}{dt} - hA_s\left(T_{fluid} - T_{wall}\right) \tag{4}$$

In GT-Power, a typical engine layout consists of several primary component objects, i.e., EngCylinder" (engine cylinder) and "EngineCrankTrain," the latter is used to model the kinematics and rigid dynamics of common reciprocating IC engine crank train configurations. It should be noted that "Compressor" and "Turbine" are also two primary components when simulating a turbocharged engine, which are not included in this study because of the lack of turbocharger performance characteristic curves. Therefore, the conditions at the intercooler outlet and turbine inlet were set at the boundaries of the engine cycle simulation to resolve the issue. Apart from these three major components, the remaining parts of an engine model are mainly connection objects, such as pipes, flow splits, orifices, intake/exhaust valves, injectors, environments, and the fluid properties. Fig. 3 is the GT-Power model for the studied engine under the conventional combustion mode, the intake and exhaust ports are modeled geometrically with pipe and flow split parts. Each object involved in the model

also consists of several reference objects for more detailed modeling information on pertinent aspects such as flow, heat transfer, etc. In general, built-in templates of both engine parts and sub-models that describe the physical processes taking place in the engine, such as combustion, heat transfer and friction, are used to establish the system-level engine model. The engine model for LTC mode is slightly different from that shown in Fig. 3, which will be further discussed in Section 5.

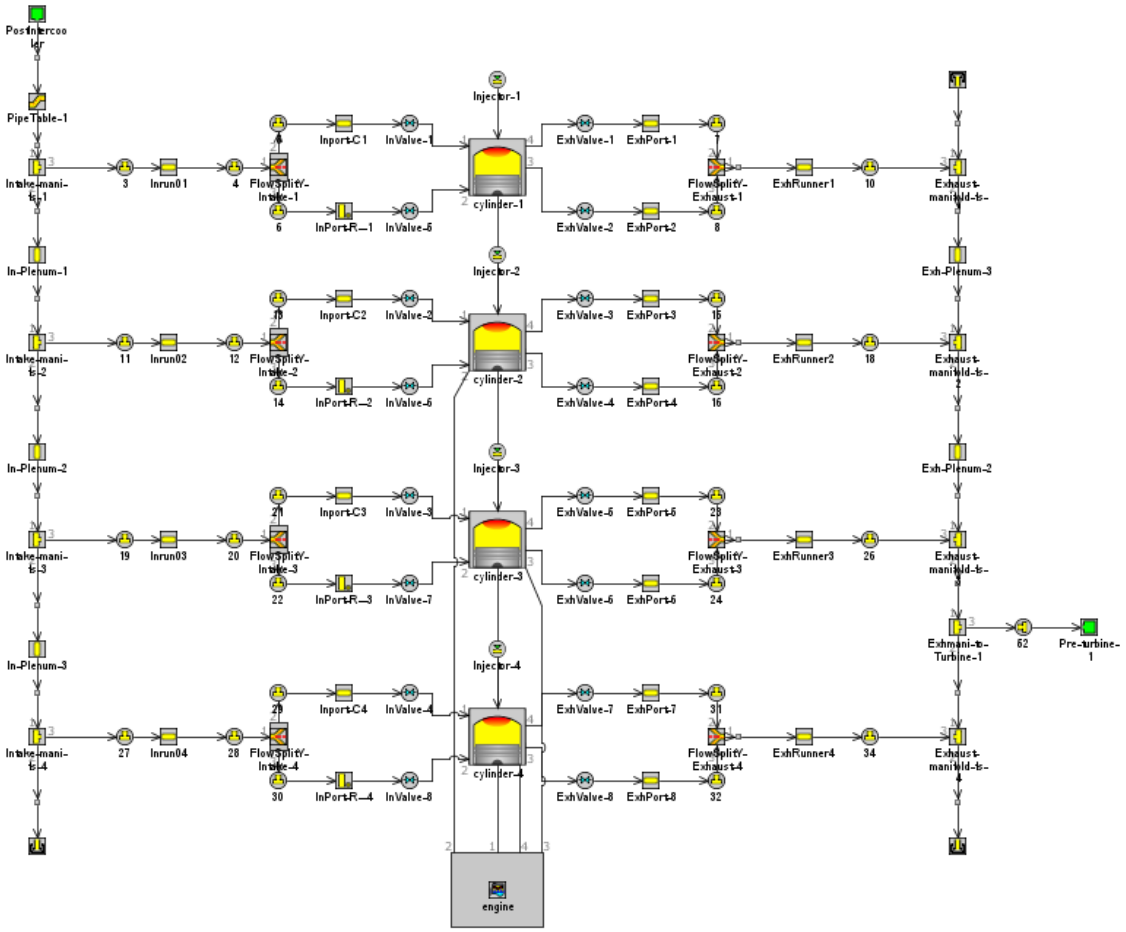

Fig. 3 Illustration of the engine model layout (conventional combustion mode).

3.2.1 Predictive Combustion Model

Proper treatment of combustion within the engine simulation is usually critical to achieve a well-predicted engine model. The engine simulation software provides the users with both predictive and non-predictive combustion modeling. A non-predictive combustion model simply imposes a burn rate as a function of crank angle. Such a prescribed burn rate profile can also be imposed with a given Wiebe function for spark-ignition engine simulations. Since the objective of this study is to develop an engine model having the capability of predicting engine performance at multiple operating conditions, predictive combustion modeling is an appropriate choice.

There are several predictive combustion models for both spark ignition and diesel engine simulations provided by the engine simulation software library. Direct-Injection Diesel Multi-Pulse Model (DIPulse) was chosen for this study due to its better prediction accuracy, fast runtime, and robustness as compared to other alternative diesel combustion models. DIPulse is capable of predicting the combustion rate and associated emissions for direct-injection diesel engines with single- and multi-pulse injection events. The cylinder contents are discretized into three thermodynamic zones in DIPulse model: (1) a main unburned zone which contains all cylinder mass at intake valve closing, (2) a spray unburned zone which contains injected fuel and entrained gas, (3) and a spray burned zone which contains combustion products. The basic idea of how DIPulse model predicts combustion behavior is to track the fuel injection, evaporation and mixing with surrounding gas, then the amount of burned fuel at each time step can be predicted, i.e., the burn rate at which fuel is moved from the unburned zone to the burned zone.

Afterwards, the particular combustion products are predicted from equilibrium chemistry. Thermodynamic relations are used to determine the temperature, heat release rate and pressure.

As a phenomenological, three-zone combustion model, four calibration multipliers — namely entrainment, ignition delay, premixed combustion rate, and diffusion combustion rate multipliers — are used to calibrate the DIPulse model. The following discussions provide more details of the associated submodels for different phases of combustion modeling.

i. Injection: Each discrete injection event is defined as a pulse in DIPulse model. There is no limit on the number of pulses and no distinction made among pilot, main, and post injections. It means that each pulse is tracked separately and added to the spray unburnt zone, accurate injection profiles and timings are required for each pulse. For example, Fig. 4 shows the injection profiles for the conventional case having an ECT of 90˚C. Injection rate, injected mass and solenoid current are included in this plot.

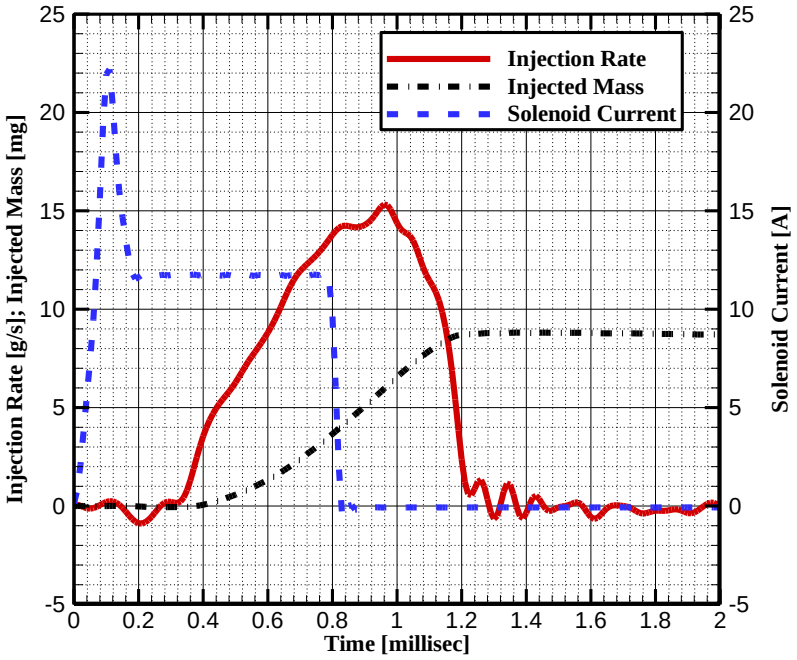

Fig. 4 Injection profiles for Case #4, conventional mode, rail pressure = 425 bar; solenoid energizing = 795 µs [76].

ii. Spray Penetration: The penetration model used in DIPulse model is modified based on empirical correlations for the spray-tip penetration [77]. Eqs. (5) and (6) give the spray penetration length s of a pulse at a time step before and after the occurrence of break up, respectively. The time to breakup of spray into droplets t_b is evaluated by Eq. (7).

$$s = u_{inj} \cdot t \cdot \left[1 - \frac{1}{16} \left(\frac{t}{t_b} \right)^8 \right] \qquad \frac{t}{t_b} \le 1 \tag{5}$$

$$s = u_{inj} \cdot t_b \cdot \frac{15}{16} \left(\frac{t}{t_b} \right)^{0.5} \qquad \frac{t}{t_b} \ge 1 \tag{6}$$

$$t_b = 4.351\sqrt{\frac{2\rho_l}{\rho_g}}\frac{d_n}{C_d u_{inj}} \tag{7}$$

$$u_{inj} = C_d\sqrt{\frac{2\Delta p}{\rho_l}} \tag{8}$$

u_{inj} represents the spray tip velocity and is determined from Eq. (8). ρ_l and ρ_g are the density of gas and liquid fuel, respectively. C_d is the discharge coefficient of the injector nozzle, d_n is the nozzle diameter, and Δp is the differential pressure between the injector tip and the chamber. The injector mounted on the engine is Bosch CRIP2.2, and the design specifications are listed in Table 6 [78]. The discharge coefficient was assumed to be 0.75 which is likely to be a lower limit for the injection conditions under this study, according to the research results presented in [79].

Table 6 Injector specifications

Injector type	Bosch CRIP2.2
Number of holes per nozzle	7
Nozzle hole diameter	0.141 mm
Included angle	149˚
Sac volume	0.23 mm^3

iii. Air Entrainment: As the spray develops, the surrounding air, residual gases, and gas from previous pulses are entrained into this current pulse and which consequently slows down the speed of jet. Such an entrainment process enables the intermixing of pulses, the rate of entrainment is modeled by applying conservation of momentum in DIPulse combustion model. As it is shown in Eq.

(9), the momentum of the spray tip, namely the initial spray momentum, should be equal to the momentum of the entrained mixture.

$$m_{inj}u_{inj} = mu \qquad or \qquad m = \frac{m_{inj}u_{inj}}{u} \tag{9}$$

m_{inj} is the initial mass of injected fuel packet. Taking the derivative of both sides of Eq. (9) yields the entrainment rate. The DIPulse model uses the entrainment rate multiplier to modify the rate of entrainment as shown in Eq. (10).

$$\frac{dm}{dt} = -C_{ent}\frac{m_{inj}u_{inj}}{u^2}\frac{du}{dt} \tag{10}$$

iv. Droplet Evaporation: The fuel evaporates as it is heated by the entrained gas, and the evaporation of droplets involves simultaneous heat and mass transfer processes. According to the energy balance theory, the change in internal energy of the droplet is the sum of heat convection transferred from the hot entrained gas and the heat lost through droplet's evaporation:

$$m_d c_{p,d}\frac{dT_d}{dt} = \frac{\delta Q_c}{dt} + \frac{\delta Q_e}{dt} \tag{11}$$

where m_d is the mass of the droplet, $c_{p,d}$ is the specific heat capacity of the droplet, T_d is the temperature of the droplet. Q_c and Q_e are the convective heat transfer and evaporation heat loss, respectively. The rate of convective heat transfer is namely determined from the Newton's cooling law, as shown by Eq. (12).

$$\frac{\delta Q_c}{dt} = h\pi d_d^2\left(T_g - T_d\right) \tag{12}$$

T_g is temperature of the hot entrained gas. The heat evaporated from the droplet, Q_e, can be obtained from the change in the droplet's enthalpy, which is given by Eq. (13).

$$\frac{\delta Q_e}{dt} = -\frac{dm_d}{dt}\Delta H_{v,d} \tag{13}$$

$\Delta \mathrm{H}_{v,d}$ is the latent heat of vaporization of the droplet, $\frac{dm_d}{dt}$ is the rate of evaporation of the droplet and can be modeled by applying mass transfer to the control volume of the droplet, see Eq. (14).

$$\frac{dm_d}{dt} = -\pi d_d \rho_g \alpha_g \mathrm{Sh} \cdot \ln\left(1 + \mathrm{B}_m\right) \tag{14}$$

α_g is the thermal diffusivity of the entrained gas, Sh is the Sherwood number for mass transfer and B_m is Spalding mass transfer number.

v. Ignition Delay: The mixture in each pulse undergoes an ignition delay modeled with an Arrhenius expression and calibrated by using the ignition multiplier C_{ign}, as it is shown in Eq. (15), the ignition delay τ_{ign} is the time between the start of injection and the start of combustion, which is modeled separately for each pulse as a function of EGR, $f\left(EGR\right)$, and bulk cylinder temperature T. The cetane number of the fuel also affects the ignition delay, where C_{ign2} and C_{ign3} are constants dependent on the fuel and the apparent activation energy.

$$\tau_{ign} = C_{ign}\rho^{C_{ign2}} \exp\left(\frac{C_{ign3}}{T}\right) f\left(EGR\right) \tag{15}$$

As a result, the ignition or the start of combustion occurs when

$$\int_{t_0}^{t_{ign}} \left(\frac{1}{\tau_{ign}} \right) dt = 1 \qquad \text{where } t_{ign} = t_0 + \tau_{ign} \tag{16}$$

vi. Premixed Combustion: After a pulse ignites, the mixture present at that time is set aside for premixed combustion. The rate of premixed combustion is assumed to be kinetically limited, and is modeled as a function of many other parameters such as kinetic rate constant for the combustion reaction k, gas temperature T, air-fuel equivalence ratio λ, and EGR fraction. The equation used for premixed combustion modeling in DIPulse model is shown in Eq. (17). C_{pm} is a tunable constant used for calibrating the combustion model, which is called the premixed combustion rate multiplier.

$$\frac{dm}{dt} = C_{pm} m \left(t - t_{ign} \right)^2 f\left(k, T, \lambda, EGR \right) \tag{17}$$

vii. Diffusion Combustion: After a pulse ignites, the remaining unmixed fuel and entrained gas in the pulse continue to mix and burn in a primarily diffusion-limited phase. Similar to premixed combustion, the rate of diffusion combustion is also modeled as a function of many other associated parameters including the kinetic rate constant for the combustion reaction k, cylinder volume V_{cyl}, EGR level, and oxygen concentration $[O_2]$, as shown in Eq. (18). C_{df} is a tunable constant used for calibrating the combustion model, which is called the diffusion combustion rate multiplier.

$$\frac{dm}{dt} = C_{df} m \frac{\sqrt{k}}{\sqrt[3]{V_{cyl}}} f\left(EGR, [O_2]\right) \tag{18}$$

3.2.2 Heat Transfer Model

For conventional engines, a large portion of the fuel energy leaves the combustion chamber as heat transfer; thus, examining in-cylinder heat transfer serves as an important role in assessing engine performance, efficiency and emissions. A large number of theoretical and experimental researches have been conducted to generate heat transfer coefficients and estimate heat fluxes in reciprocating engines. Depcik et al. [80] summarizes many of the empirical correlations developed since the 1920s. One of the most popular engine heat transfer correlations is proposed by Woschni [81]. Woschni's correlation can be summarized as:

$$h_c = 3.26 B^{-0.2} p^{0.8} T^{-0.55} w^{0.8} \tag{19}$$

where h_c is the in-cylinder heat transfer coefficient, B is cylinder bore, and p and T are the instantaneous cylinder pressure and gas temperature, respectively. The symbol w is the average cylinder gas velocity; for a four-stroke, water-cooled, four-valve direct-injection CI engine without swirl, w is defined as:

$$w = \left[C_1 \overline{S}_p + C_2 \frac{V_d T_r}{p_r V_r} \left(p - p_m \right) \right] \tag{20}$$

where $\overline{S}_p$ and V_d are the mean piston speed and the displaced volume, respectively. And p_r, V_r, and T_r are the cylinder gas pressure, volume, and temperature at intake valve

closing; p_m is the motored cylinder pressure at the same crank angle as p. Constants C_1 and C_2 vary at different cycle periods:

- For the gas exchange period: $C_1 = 6.18, \quad C_2 = 0$
- For the compression period: $C_1 = 2.28, \quad C_2 = 0$
- For the combustion and expansion period: $C_1 = 2.28, \quad C_2 = 3.24 \times 10^{-3}$

In high-speed engines where swirl and higher heat transfer occur, the average cylinder gas velocity is still given by Eq. (20) but with different definitions of C_1 and C_2 [2].

There are a number of heat transfer models provided in the engine simulation software packages, most of which stem from Woschni's model [81]. A modified Woschni model "WoschniGT" was selected for this study because of a lack of swirl data for the experimental engine. The convective heat transfer coefficient for "WoschniGT" model is defined as follows:

$$h_c = 3.01426 B^{-0.2} p^{0.8} T^{-0.5} w^{0.8} \tag{21}$$

Compared with the classic Woschni's correlation, see Eq. (17), the "WoschniGT" model has a slightly different exponent for the temperature term. The definition of the average cylinder gas velocity w is still same as given by Eq. (20), except that the constant C_1 is newly defined in "WoschniGT" by accounting for the trapping efficiency, as described by Eq. (22). It can be noticed from the comparison with Eq. (19) that the major difference lies in the treatment of C_1 during the period when the valves are open, where the heat transfer is increased by inflow velocities through the intake valves and by backflow through the exhaust valves [76].

$$C_1 = 2.28 + 3.9MIN\left(\frac{\text{Net mass flow into cylinder from valves}}{\text{Trapped mass} \times \text{Engine Frequency}}, 1\right) \quad (22)$$

In addition to obtaining the heat transfer coefficient, wall temperature calculation is a subsequent process for determining in-cylinder heat transfer of the simulation engine. When the temperature measurements are not available, the head, piston, and cylinder walls temperatures can be imposed for continuing the simulation. The suggested values by the engine simulation software at full load are:

- Head temperature: 550 – 600 K
- Piston temperature: 550 – 600 K
- Cylinder temperature: 400 K

Previous research efforts for piston temperature measurements show that the suggested values above can be considered to be reasonable estimates. Kruggel [82] measured the piston temperature distribution for an air-cooled two-stroke gasoline engine, the results show that the maximum temperature in the center of piston crown was 620 K at 2800 rpm. The piston crown center temperature gradually decreased as the engine speed decreased. Wu and Chiu [83] reported the temperature variations in piston at different engine speed and torque for a single-cylinder diesel engine. The maximum piston temperature was 633 K at maximum power and 600 K at maximum torque. When the engine is motoring, the temperature changed from 405 K to 454 K as the speed increased from 2000 to 2200 rpm. References [84, 85] investigated the piston and head temperatures for HCCI engine in light-duty engines, where the ensemble average temperatures are only around 430 K.

These studies indicate that the imposed wall temperature could be significantly different under different engine operating conditions; for this study, another associated problem with imposing wall temperatures is that the simulation would not be able to use ECT as the control parameter for extended simulation work on higher ECT conditions, which are difficult to attain on the instrumented engine due to the constraints of oil temperature [74]. As a result, an alternative method to implement the in-cylinder heat transfer modeling was recommended in this study, namely calculating wall temperatures with necessary geometry information input as well as boundary conditions (the coolant temperatures). The given cylinder head, piston, liner, and even the coolant jacket information specify a simplified and parameterized geometry, which allows the engine simulation to generate a finite element structure for calculating wall temperatures. In the meantime, the ECT information is used to define the boundary conditions; therefore, ECTs can be varied through the case setup. In this case, the simulation engine has the capability to keep using the same actuators as that set up in the experimental investigations.

3.2.3 Friction Model

In general, friction losses can be classified into two groups: 1) the friction between two metal surfaces in relative motion, with a lubricant in between, 2) and the turbulent dissipation [2]. The total friction work per cycle W_{tf} for a given engine geometry typically varies with speed according to:

$$W_{tf} = C' + C'' N + C''' N^2 \tag{23}$$

where N is the crankshaft rotational speed. Some of the lubrication friction and turbulent dissipation, however, can be dependent on mean piston speed rather than N. From Eq. (23), it is evident that avoiding high engine speeds is important for high mechanical efficiency.

One of the most widely-employed friction models is perhaps the Chen & Flynn model [86], which relates the total friction losses (friction mean effective pressure *FMEP*) to mean piston speed $\overline{S}_p$ and the peak in-cylinder pressure $p_{\max}$. Eq. (24) shows this relationship.

$$\begin{aligned} FMEP\left(bar\right) = a\left(bar\right) + b \cdot p_{\max}\left(bar\right) + c\left(bar \cdot s/m\right)\overline{S}_p\left(m/s\right) \\ + d\left(bar \cdot s^2/m^2\right)\overline{S}_p\left(m/s\right)^2 \end{aligned} \tag{24}$$

Constant a accounts for the energy drawn by accessories and all the other invariable factors [87]. Load effect is represented by the peak in-cylinder pressure through constant b. Constants c and d account for the effects of mean piston speed by means of a quadratic law. The engine simulation software uses this Chen-Flynn model to calculate engine friction. The recommended values of the four constants are shown in Table 7 for approximating the friction of a typical engine.

Table 7 Recommended values of friction model constants [75]

a	0.3 – 0.5 bar
b	0.004 – 0.006
c	0.08 – 0.10 bar·s/m
d	0.0006 – 0.0012 bar·s^2/m^2

3.2.4 Emissions Model

The engine simulation software predicts a number of species that typically are present in the combustion products, including N_2, O_2, CO_2, CO, H_2O, H, O, OH, NO, N, SO_2 (if sulfur exists in the fuel), by using equilibrium chemistry. Some particular species such as unburned hydrocarbons and soot may be calculated using chemical kinetics, but only for certain models. For example, only the predictive SI model has the capability to predict unburned hydrocarbons, while the predictive combustion models for diesel engine (e.g., DIPulse) do not predict unburned hydrocarbons. This section will discuss two submodels of emission formation, the NO_x model and the soot model. It should be noted that the engine simulation software predicts emissions on a wet basis. The measured dry concentrations from the experimental engine, therefore, need to be converted to the corresponding wet values for comparison to the simulation outputs.

i. NO_x Model: The NO_x emissions are calculated using the extended Zeldovich mechanism in the engine simulation, where the governing reaction equations [2] are shown as below:

$$O + N_2 \rightleftharpoons NO + N \tag{25}$$

$$N + O_2 \rightleftharpoons NO + O \tag{26}$$

$$N + OH \rightleftharpoons NO + H \tag{27}$$

The rate constants k_1, k_2, k_3 (in units of $m^3/(kmol \cdot sec)$) that used in the simulation software to calculate these three reaction rates are given by Eqs. (28)–(30) [75], respectively. F_1, F_2, and F_3 are the oxidation rate multipliers used to calibrate

the model, and A_1 and A_2 are the activation temperature multipliers for N_2 oxidation and N oxidation, respectively. T_b is the temperature of the burned zone mixture.

$$k_1 = F_1 \times 7.6 \times 10^{10} \times e^{-38000 A_1 / T_b} \tag{28}$$

$$k_2 = F_2 \times 6.4 \times 10^{6} \times e^{-3150 A_2 / T_b} \tag{29}$$

$$k_3 = F_3 \times 4.1 \times 10^{10} \tag{30}$$

ii. Soot Model: Only the predictive combustion models for diesel engines have the capability to predict soot concentrations in GT-Power. The DIPulse model provides the users with different soot modeling options, which are based on either Hiroyasu's model [88] or Nagle & Strickland-Constable model [89]. In Hiroyasu and Kadota's model, the concentration of soot in the exhaust is governed by two empirical rate equations, formation and oxidation. Previous works have revealed that the soot formation is primarily affected by pressure, temperature and equivalence ratio [18]. Both soot formation in vapor phase pyrolysis and in liquid phase were considered in this model. The first order reaction from the fuel vapor is assumed to be the soot formation mechanism, the second order reaction between the soot and oxygen is assumed to be the soot oxidation [90], which end up with the following equations to calculate soot.

$$\frac{dm_s}{dt} = \frac{dm_{sf}}{dt} - \frac{dm_{sc}}{dt} \tag{31}$$

$$\frac{dm_{sf}}{dt} = A_f m_{fg} p^{0.5} \exp\left(-\frac{12500}{RT}\right) \tag{32}$$

$$\frac{dm_{sc}}{dt} = A_c m_s \frac{p_{o_2}}{p} p^{1.8} \exp\left(-\frac{14000}{RT}\right) \tag{33}$$

m_s, m_{sf}, m_{sc}, m_{fg} are the mass of soot, mass of formed soot, mass of oxidized soot, and mass of fuel vapor. A_f and A_c are the constants determined from the model validation with the experimental measurements, and p_{o_2} is the partial pressure of the oxygen. Eq. (32) reveals that the soot formation is primarily affected by the pressure, temperature and equivalence ratio of the gas mixture.

The Nagle & Strickland-Constable (NSC) model is most-commonly introduced to describe high-temperature oxidation of soot. They measured the oxidation of a pyro graphite over temperatures from 1000 to 2000˚C and pressures from 0.1 to 0.6 atm. The NSC model assumes two types of active sites presenting on the carbon surface available for oxygen attack, the more reactive type A and the less reactive type B sites [2, 89]. Eqs. (34) and (35) describe the reactions between oxygen and these two different types of sites, and a thermal rearrangement of A sites into B sites is also allowed, see Eq. (36).

$$\mathrm{A} + \mathrm{O_2} \rightarrow \mathrm{A} + 2\mathrm{CO} \qquad \text{at a rate given by } \frac{k_A p}{1 + k_Z p} x \tag{34}$$

$$\mathrm{B} + \mathrm{O_2} \rightarrow \mathrm{A} + 2\mathrm{CO} \qquad \text{at a rate of } \mathrm{k}_B p(1-x) \tag{35}$$

$$\mathrm{A} \rightarrow \mathrm{B} \qquad \text{at a rate of } \mathrm{k}_T x \tag{36}$$

Parameter x in the equations above is defined as $x = \frac{1}{1+\left(k_T / k_B\right) p}$. k_A, k_B, k_T, k_Z are the rate constants for the NSC soot oxidation mechanism, which are assigned values listed in Table 8.

Table 8 Rate constants for Nagle and Strickland-Constable soot oxidation mechanism [2]

$k_A = 20\exp\left(-15{,}000 / T\right)$	g/cm^2·s·atm
$k_B = 4.46\times10^{-3}\exp\left(-7640 / T\right)$	g/cm^2·s·atm
$k_T = 1.51\times10^{5}\exp\left(-48{,}800 / T\right)$	g/cm^2·s
$k_Z = 21.3\exp\left(2060 / T\right)$	atm^{-1}

3.3 Calibration Strategy

A predictive engine model should have the capability to automatically adjust to different operating conditions (e. g., ECT, EGR rate, load, and speed) with no change in calibration constants. As a result, a robust and logical calibration procedure is needed such that a single set of model constants can be generated to predict the engine performance over a wide variety of operating points. As mentioned earlier, the engine model shown in Fig. 3 is only applied to conventional combustion mode, the LTC mode will be simulated using a slightly different engine model which includes the exhaust gas recirculation modeling. The calibration procedure introduced in this section was developed based on the conventional engine model, but the methodology is generally consistent as it proceeds to the LTC model calibration. The simulation results presented in this section will focus on the conventional mode, and the validation work for LTC mode will be comprehensively discussed in Section 5.

The general calibration methodology is illustrated in Fig. 5. Two different types of engine simulation models were established to complete the model validation. The first stage is called Cylinder Pressure Only Analysis (CPOA), where calibration constants for the combustion and the heat transfer sub-models are determined. Such a process is carried out in a single-cylinder model, termed as COPA model. The model constants calibrated from the CPOA are then applied to the full four-cylinder model (i.e., Fig. 3 for the conventional mode) for the second stage of calibration work. In the full engine model, the friction model is further calibrated and simulation is validated against experimental data at different ECTs. These two stages are illustrated by the left box and right box of Fig. 5, respectively. The calibration details for each step shown in Fig. 5 will be further discussed in the following.

It is likely that there are errors in experimental measurement of parameters that are used as simulation inputs, which in turn can bring some amount of inaccuracies in model predictions. Consequently, the primary benefit of using CPOA is to check the consistency of input data prior to calibrating combustion model. This is realized by running the CPOA model with measured pressure data and performing a set of automatic checks that indicate a cumulative error in the burn rate calculation. This feature is not

available in the multi-cylinder engine model. Likewise, a preliminary calibration constant for the heat transfer model can be obtained by running motoring case. Fig. 6 shows the motored pressure trace at 1500 rpm from the CPOA model compared to measured data. The other two motoring cases at 1500 and 1750 rpm are displayed in Appendix I, which also show that the simulated pressures from the CPOA model are in good agreement with the measurements.

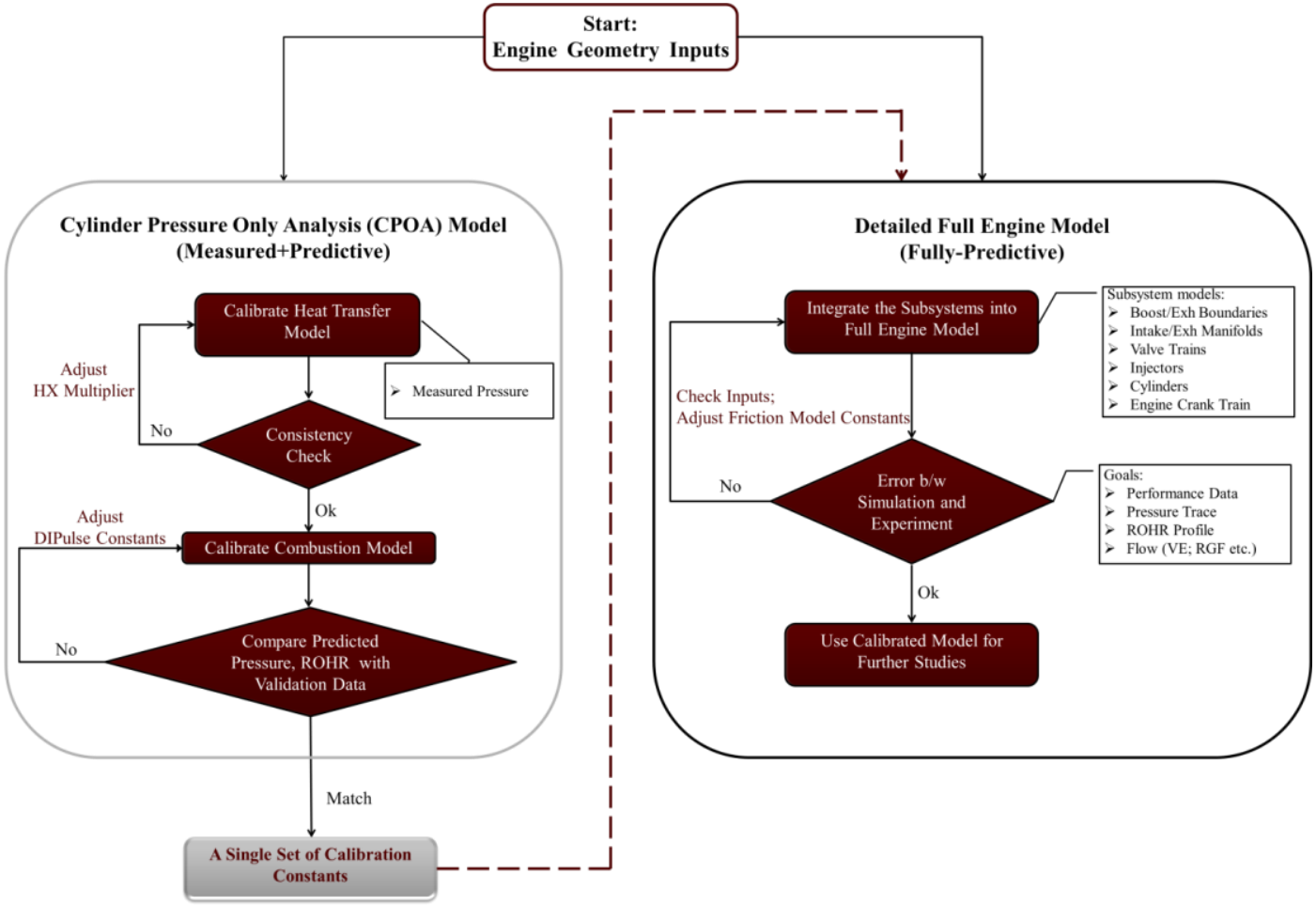

Fig. 5 Flowchart of calibration strategy.

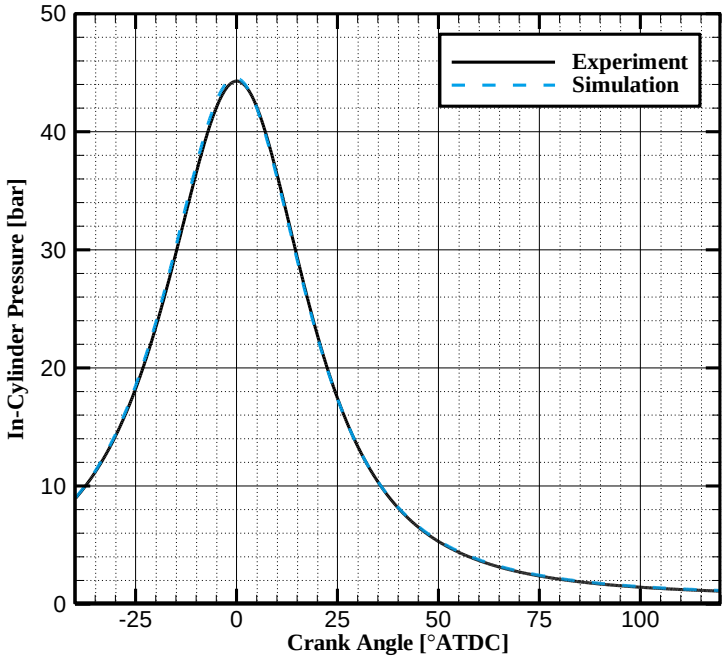

Fig. 6 Cylinder pressure comparison of motoring case at 1500 rpm.

With the preliminarily calibrated heat transfer model, the firing case with an ECT of 90°C (Case #4) was used in the CPOA model to further calibrate the combustion model. This resulted in a set of DIPulse model constants that can provide the best possible match for the remaining cases. Generally, the cylinder pressure during expansion stroke tends to be more sensitive than the compression pressure to the heat transfer model constants. Therefore, the heat transfer model constant determined from motoring cases may not work ideally for a firing case; in that case, the heat transfer model still needs fine-tuning as calibrating combustion model, but the adjustment is only around 2–3% in this study.

The next step is applying the calibrated combustion and heat transfer model constants obtained from the CPOA to a full engine model, which consists of four cylinders and detailed parts of the studied engine. Different from the CPOA model, the full engine model does not require the inputs of measured pressure data for consistency check; rather, using the calibrated combustion and heat transfer model from the CPOA simulation makes it become a fully predictive model. With this now being an engine-level simulation, the friction model needs to be calibrated at this step. As mentioned in Section 3.2.3, the Chen-Flynn friction model [86] built in the engine simulation software package was used. Furthermore, small adjustments in flow resistance parameter may be made to fine-tune the model so the predictions match measurements more closely. As a result, the predicted cylinder pressure, rates of heat release (ROHR) or other quantities by the full engine model are unlikely to be exactly same as that predicted by the CPOA model, but the discrepancies are meant to be small and ideally insignificant.

The predictions of Case #4 are compared with validation data in Fig.7. The predicted cylinder pressures match the experimental data well. However, the simulation slightly overestimates the ROHR during the diffusion phase causing the difference in peak heat release rate. These discrepancies do not cause a major concern since much of the use of the simulation is to capture thermodynamic parameters of the engine system where precise match in pressure is the first priority [91]. At this point, the calibration procedure is completed and a full set of calibration constants of heat transfer, combustion, and friction are generated for studying the remaining cases. The sweep of ECT is used to validate this full model; similar phenomena shown in Case #4 (ECT =

90°C) have also been observed from the other four cases, see Appendix I. Computed cylinder pressure and ROHR are compared with experimental measurements since they are closely correlated with combustion behavior and the thermodynamic routines employed by the engine simulation software. In spite of that, there are still some more engine parameters such as intake/exhaust manifold pressure, temperature and volumetric efficiency that need to be validated.

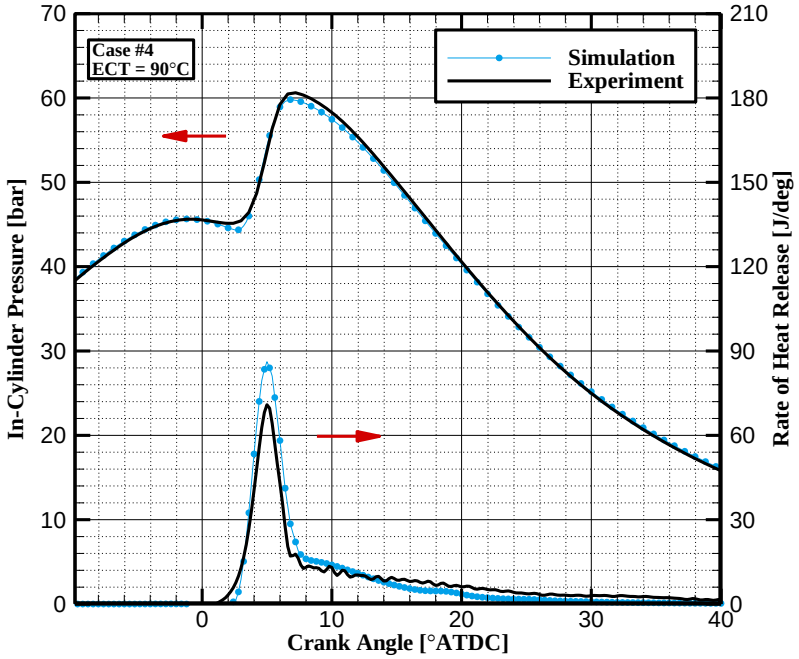

Fig. 7 Cylinder pressure and ROHR comparisons for Case #4, conventional mode.

Given that NO_x emissions are closely associated with the combustion rate, the combustion model needs to be calibrated with measurements prior to integrating the NO_x model into the engine simulation. The NO_x model used for this simulation study is established based on the extended Zeldovich mechanism, and the kinetic rate constants

are taken from the recommended values published in [14]. Fig. 8 shows the simulated NO_x concentration (in units of ppm) and brake specific NO_x ($BSNO_x$) of conventional mode validated against the measurements. The error bars in all data plots are created from different sets of measurements on two separate days. It should be noted that there are no error bars for Case #1 (ECT = 56.5˚C), since only one set of measurements was attained. In general, the variations of simulation results have similar patterns to that observed from the experimental data. The predicted NO_x concentrations seem to be overestimated by around 2–3% compared to the measurements, but both results show an increase with increasing ECT due to the retained energy causing higher in-cylinder temperatures. The Zeldovich NO formation mechanism is sensitive to both pressure and temperature, but more so temperature than pressure. Because the simulated pressures match the validation data well, it is likely that the two-zone temperature calculation of the simulation model does not capture the maximum temperature of the burned zone very accurately. Both the simulation and experiment show gradual decreases in $BSNO_x$ due to the improvement in brake power exceeding the increase of NO_x emissions as ECT increases. The underprediction of $BSNO_x$ relative to experimental BSNOx (compared to the overprediction of NOx concentration) results from an underprediction in total mass flow rate through the simulated engine.

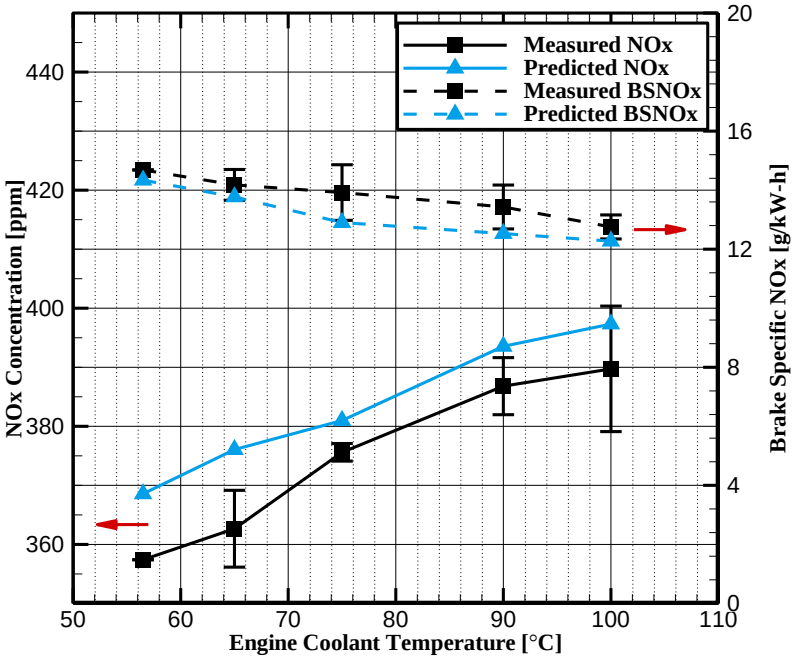

Fig. 8 validations of predicted NO_x concentration and $BSNO_x$ (conventioinal mode).

4. LHR CONCEPT IMPLEMENTED INTO CONVENTIONAL ENGINE*

4.1 Conventional-LHR Engine Simulation Validation

This section is structured such that validation comparisons between simulation and experiment are made along with analysis of the impact of ECT on engine parameters in conventional combustion engine. As mentioned before, the simulation work for the LTC combustion mode will be addressed in Section 5. It is known from the previous section that the predicted pressures and measurements are generally in good agreement with experimental measurements. Noticeable discrepancies in ROHR during the diffusion phase, however, remain among all cases.

The validation work for instantaneous cylinder pressures and ROHR has been previously discussed. This section attempts to mainly validate the flow characteristics and engine performance. Since the universal metrics to quantify the quality of GT-Power model predictions are rarely found in the existing literature, relative errors under ±5% are considered to be good/acceptable predictions in this study. It is usually difficult to simultaneously achieve good accuracies for all parameters; the model validation therefore attempts to primarily attain better accuracies for the parameters that mostly represent the engine performance and combustion behavior. The factors causing inaccuracies of more than ±5%, however, will be further explored to provide clues about the sources of these differences.

---

* Part of the data reported in this chapter is reprinted with permission from "Energy distributions in a diesel engine using low heat rejection (LHR) concepts" by Li T, Caton JA, and Jacobs TJ, 2016. Energy Conversion and Management, vol. 130, pp. 14-24, Copyright (2016) by Elsevier.

4.1.1 Flow Characteristics

i. Volumetric efficiency (VE): Validation of volumetric efficiency is significant for the engine simulation since it impacts the accuracy of simulated manifold pressures as well as air/fuel ratio, and the subsequent combustion behavior in the chamber. Likewise, a well-predicted amount of intake air can avoid unreasonable tuning of the model constants. Hence, VE is necessary to be validated before attempting to correlate other engine performance predictions to measured data. Fig. 9 shows the comparison of VE between simulation and experiment. The predictions are lower than experimental calculations by 3–5%. Eq. (37) gives the definition of the volumetric efficiency (VE) for a four-stroke engine. The freshly charged air flow rate $\dot{m}_{air}$ is measured twice – once using a laminar flow element and then using the stock mass air flow sensor. V_d represents the displacement volume and N is the engine speed, both of which are constant for the studied cases. The air density ρ_{air} is calculated from measured ambient temperature and barometric pressure by using ideal gas equation.

$$VE = \frac{\dot{m}_{air}}{2\rho_{air}V_d}\left(\frac{1}{60N}\right) \tag{37}$$

The experimental VE is observed to decrease slightly with elevated ECT. Simulation results are basically following a similar variation trend, except that VE for Case #5 (ECT = 100°C) occurs to slightly exceed that of Case #4 (ECT = 90°C), but which is still smaller than the other three cases. The volumetric efficiency shortfall is considered to be produced by higher operating temperature

conditions where heat losses are expected to be lower; hence, the hotter cylinder walls and residual gas decrease the density of the inducted air. From this point of view, reduction in VE is one of the common concerns that limit the improvement in the overall performance of LHR engines [92, 93].

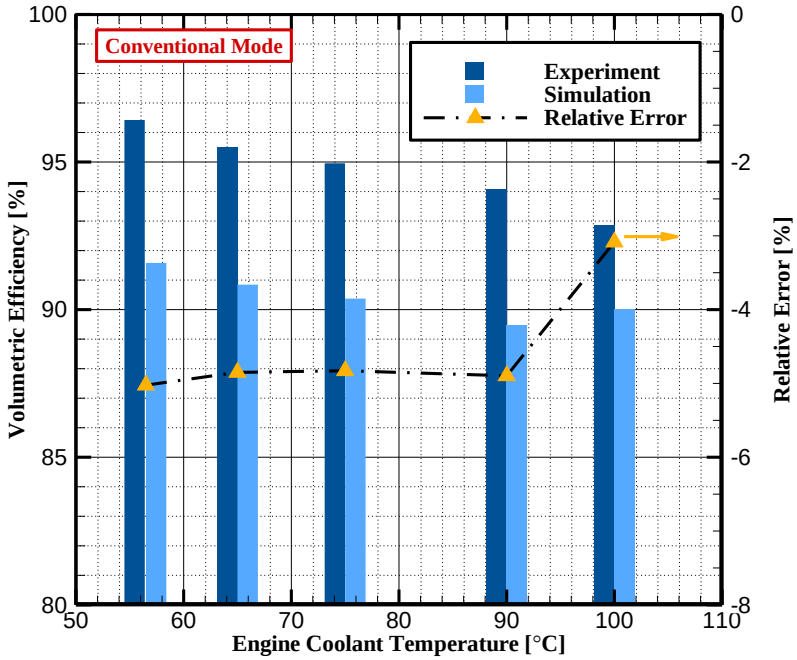

Fig. 9 Comparisons of VE between simulation and experiment (conventional mode).

ii. Residual gas fraction (RGF): RGF influences the combustion behavior, engine performance, emissions and volumetric efficiency; yet accurate prediction or even measurement of this quantity is difficult to do. Fox et al. [94] proposes a zero-dimensional method to estimate residual gas fraction (RGF) for gasoline engines; later, Senecal et al. [95] modified the correlation proposed in [94] to extend its application in diesel engines, which achieved satisfactory agreement

with experiment. This empirical model postulates two contributions to the RGF, cylinder content at intake valve opening and backflow during valve overlap. An overlap factor (OF) and pressure difference between intake port and exhaust port are the primary parameters utilized to evaluate RGF. Due to the limitations on test bench under the study, RGF measurement is not available. The zero-dimensional empirical correlation presented in [95] is used to estimate the RGFs from measured quantities, and a comparison with simulation is conducted to roughly examine the accuracy of the engine model. The empirical correlation is depicted as Eq. (38):

$$
\begin{aligned}
x_r = {} & 3.3089 \cdot 10^5 \cdot \left(\frac{RT_1}{P_5}\right)^{1/2} \cdot \left(\frac{P_5}{P_1}\right)^{\frac{g+1}{2g}} \cdot \frac{r_c - 1}{r_c} \cdot \\
& \frac{\left(1 + b_{RGF}\right)^{\frac{g-1}{2g}}}{\left(1 + b_{RGF} + w\right)^{1/2}} \cdot \sqrt{\left|P_5 - P_1\right|} \cdot \frac{OF}{N} \\
& + 2.2662 \cdot \frac{1}{r_c} \cdot \left(\frac{P_5}{P_1}\right)^{1/g} \cdot \frac{\left(1 + b_{RGF}\right)^{\frac{g-1}{g}}}{1 + b_{RGF} + w} \cdot \\
& \left(f^2 - 0.5295 f + 0.5295\right)
\end{aligned}
\tag{38}
$$

where the variables b_{RGF} and ω are quantities defined in [95], which are directly dependent on the conditions of mixture gas in the chamber as well as fuel properties. The definitions of b_{RGF} and ω are provided in the Appendix II.

Table 9 compares the RGFs predicted from engine simulation to the estimations from the empirical model, which shows that the simulated RGFs are lower than

the empirical estimations by around 1.7%. The discrepancy between the simulation and the empirical model can be attributed to the following reasons:

- Correctly capturing the gas exchange process is important to the prediction of RGF in the engine simulation, which means it would be difficult to obtain accurate residuals at IVC when there are flow characteristics uncertainties within the simulation.
- Since the empirical model results are calculated based on measured quantities, the discrepancies of relevant parameters, such as in-cylinder pressures and gas temperatures, between the engine simulation and experimental measurements can also likely result in the differences observed in Table 9.

Table 9 Simulated RGFs compared to calculations from empirical model

Case #	ECT	Engine Simulation	Empirical Model
1	56.5°C	8.89%	10.63%
2	65°C	8.86%	10.69%
3	75°C	8.80%	10.57%
4	90°C	8.74%	10.44%
5	100°C	8.73%	10.61%

It can be noticed that there is little change in RGF when the ECT varies from 56.5 to 100°C. Eq. (38) implies that pressure differential between the exhaust and intake, OF and equivalence ratio are the critical parameters that determine the residual fraction; the cases under this study are designed to have nearly constant

operating loads, thus the parameters discussed above should not change much with altering ECT.

4.1.2 Engine Performance

Figs. 10 and 11 compare the simulated predictions and experimental measurements of IMEP and BMEP, respectively. All the indicated quantities presented in this study represent the net indicated values, which include IMEP, indicated SFC, and indicated fuel conversion efficiency. As shown in Fig. 10, the differences in IMEP between the simulation and experiment are maintained over the range within 6–8% at the five different operating ECTs; the prediction accuracy of BMEP reveals to be better than that of IMEP, the relative errors are consistently lower than 4%.

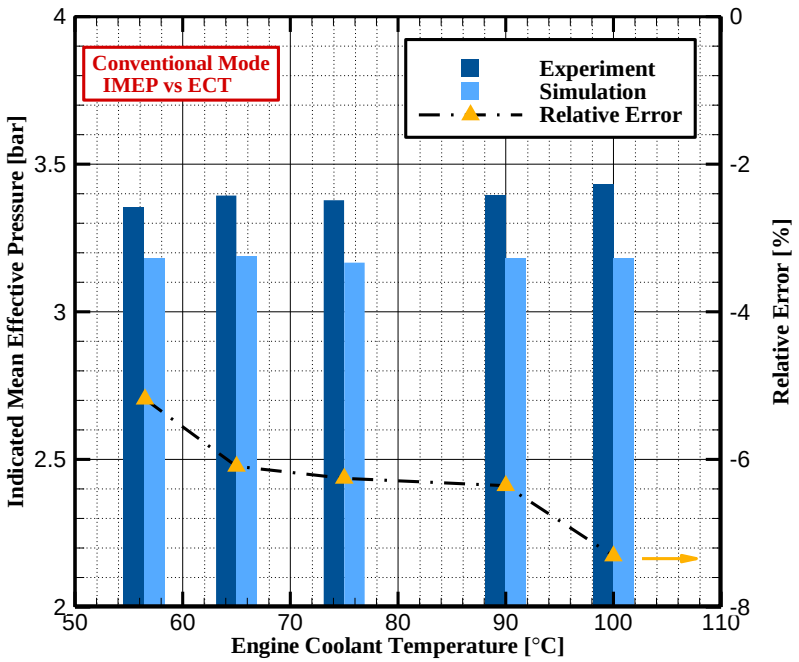

Fig. 10 Comparison of IMEP between simulation and experiment (conventional mode).

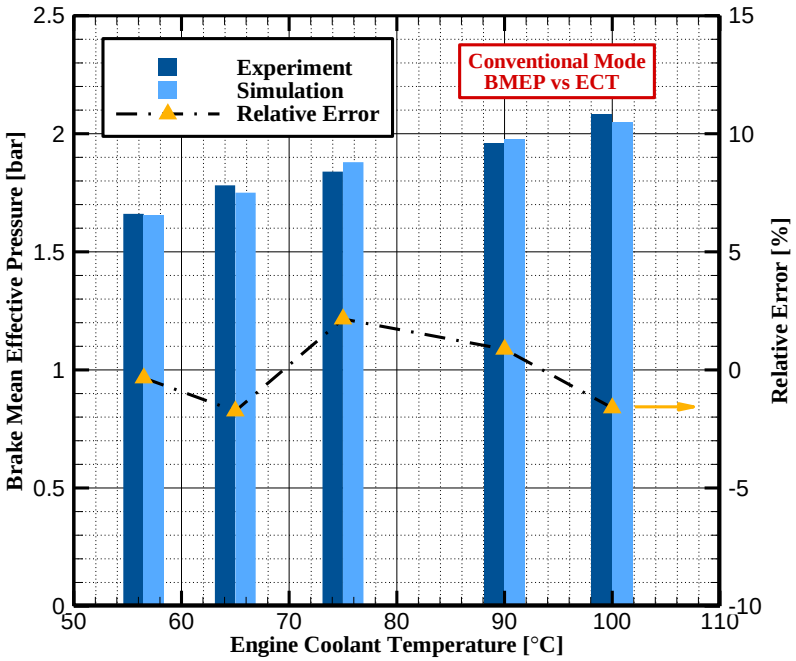

Fig. 11 Comparison of BMEP between simulation and experiment (conventional mode).

Uncertainties in the flow characteristics of intake valve train are considered as the dominant source that degrades the accuracy in IMEP. The discharge coefficients of the engine valves are typically measured from experiment; it is required to know the air pressure drop across the valves, which however is difficult to obtain from the test bench under this study. Therefore, the experimental discharge coefficients as a function of the valve lift presented in [96] are scaled by the studied engine valve dimensions for this work. Both VE and air flow rate are predicted within tolerated uncertainties by using this approximation, but it may cause relatively significant inaccuracy in the flow

characteristics during valve opening which consequently impacts the accuracy in computing indicated work.

4.2 Conventional-LHR Energy Balance Analyses

Energy efficiency is one of the most significant assessment factors concerned with the internal combustion engine. From the perspective of thermodynamics, the IC engine may theoretically approach 100% efficiency because the IC engine converts chemical energy to mechanical energy, since the chemical energy is fully available to do useful work [2]. As it has been stated in Section 1.1, the IC engine will still be limited, however, by second law considerations [1]. Actual IC engines generally convert only approximately one-third of the fuel energy to useful work; the rest is rejected in the form of thermal energy to the coolant and exhaust. This section aims at providing a detailed consideration of the energy balance for the LHR engine realized by elevated coolant temperatures under the conventional combustion mode. It has been shown in Section 4.1.2 that increasing ECT yields slight increase of IMEP but relatively greater improvements of BMEP. The reason for this will be described in this section by leveraging the energy balance analyses along with the discussions on the fuel conversion efficiencies.

4.2.1 Energy Path Analysis

In some previous studies on engine energy balances, the engine block has been considered as the steady-state control volume (CV) with air and fuel energy entering the open system and four energy flows leaving the system [97-99]. As can be seen from Fig.

12, these four energy flows leaving the control volume are brake power ($\dot{W}_b$), heat losses to the coolant ($\dot{Q}_{cool}$), exhaust energy ($\dot{m}_{exh}h_{exh}$), and the unaccounted energy ($\dot{Q}_{unac}$).

$$\dot{m}_f h_{fuel} + \dot{m}_{air} h_{air} = \dot{W}_b + \dot{Q}_{cool} + \dot{m}_{exh} h_{exh} + \dot{Q}_{unac} \quad (39)$$

The terms on the left represent input fuel energy and air energy, $\dot{m}_f$, $\dot{m}_{air}$, and $\dot{m}_{exh}$ are corresponding to the mass flow rates of injected fuel, inducted air, and exhaust gas. h_{fuel} stands for the enthalpy of fuel (#2 diesel), which may be approximated with the lower heating value since the sensible enthalpy is almost negligible as compared to the lower heating value. h_{air} and h_{exh} represent the enthalpies of air and exhaust gas, respectively. The unaccounted energy ($\dot{Q}_{unac}$) includes the heat rejected to the oil plus convection and radiation dissipated to the environment through the engine's external surfaces.

The described energy flows above provide a straightforward way to develop the energy balance study based on usual engine measurements. Whereas this study attempts to compare the energy distributions between the simulation and experiment, the lack of information on turbocharger, intercooler and exact engine external structures (e.g., engine block surfaces) prevents the simulation from capturing the unaccounted energy. To ensure the experimental energy balance analyses follow a consistent fashion of energy paths that the simulation can provide, a different thermodynamic system (by taking the combustion chamber as the control volume) was selected to develop the energy balance analyses in this study. Fig. 13 depicts the energy flows of this internal system, and Eq. (40) is the overall energy balance that provides information on the

disposition of the input energy. It is noted that blowby losses and crevice flows are neglected in this control system.

$$\dot{m}_f h_{fuel} + \dot{m}_{air} h_{air} = \dot{W}_{i,net} + \dot{Q}_{HT} + \dot{m}_{exh} h_{exh} \tag{40}$$

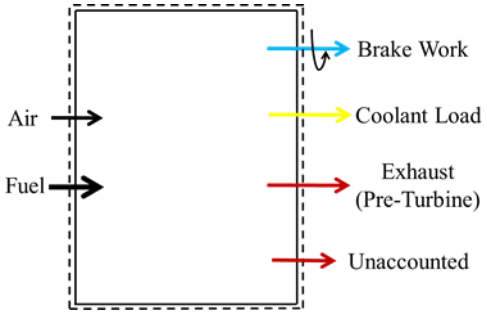

Fig. 12 The engine block as a thermodynamic open system operating in a steady-state fashion.

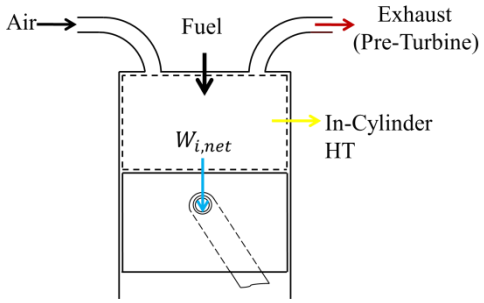

Fig. 13 The engine combustion chamber as a thermodynamic open system operating in a steady-state fashion.

The major difference between Eq. (39) and Eq. (40) is the energy flows leaving the control volume, which consists of net indicated power ($\dot{W}_{i,net}$), heat transfer from gases to the chamber walls (in-cylinder heat transfer rate, $\dot{Q}_{HT}$), and exhaust energy ($\dot{m}_{exh} h_{exh}$) for the second system. The engine simulation is capable of providing complete information for these energy flows. The following subsections will briefly review the methodologies used to experimentally determine the net indicated work, in-cylinder heat transfer, and exhaust energy.

i. Net Indicated Work: The net indicated work is the sum of the gross work and the pumping work, which are evaluated from in-cylinder gas pressures by taking an integral over an engine's mechanical cycle:

$$W_{i,net} = \oint p dV \tag{41}$$

It can also be expressed as a relationship of different forms of work:

$$W_{i,net} = W_b + W_f \tag{42}$$

where W_f represents friction work, and the brake work, W_b, is obtained from the direct dynamometer measurement. All the work terms discussed in this paper are referred to as the absolute values without accounting for the sign convention, and it is evident that the relationship can also be applied to the corresponding power parameters.

ii. In-Cylinder Heat Transfer: Directly measuring the in-cylinder heat transfer rate is usually complicated and typically requires temperature measurements of multiple positions on the cylinder liner in order to obtain the temperature field. An alternative way to obtain $\dot{Q}_{HT}$ is by considering the engine's overall heat rejection to the environment (e.g., coolant system and other convective and radiative surface losses). Comparing the two different control volume systems described at the beginning of Section 3, and rearranging Eqs. (39), (40), and (42) yields the $\dot{Q}_{HT}$ as given by Eq. (43). Namely, the in-cylinder heat transfer rate can be estimated by subtracting the friction power from the total heat rejection.

$$\dot{Q}_{HT} = \dot{Q}_{cool} + \dot{Q}_{unac} - \dot{W}_f \tag{43}$$

The heat rejection to the coolant is determined from the temperature rise in the coolant $(T_e - T_i)$ as it passes through the engine and the mass flow rate of coolant, $\dot{m}_{cool}$.

$$\dot{Q}_{cool} = \dot{m}_{cool} c_{p,c} (T_e - T_i) \tag{46}$$

The dominant source of the unaccounted losses is the environmental heat losses [2], i.e., the heat transfer from engine external surfaces to the surroundings by conduction, convection and radiation. The calculations of the surface heat losses have been detailed in [25].

In contrast to the other two energy flows that are directly derived from experimental measurements, using Eq. (43) to calculate $\dot{Q}_{HT}$ may carry errors from the computations of the involved terms ($\dot{Q}_{cool}$, $\dot{Q}_{unac}$, and $\dot{W}_f$) in addition to errors from relevant measurements. Alkidas [100]and Moore, et al. [101] also employ this approach to estimate the net in-cylinder heat transfer rate for their LHR engine studies.

iii. Exhaust Energy: For steady state, the mass flow rate of the exhaust gas is known in terms of the measured mass flow rates of air and fuel. Therefore, the exhaust gas energy can be determined from the balance:

$$\dot{m}_{exh}h_{exh} = \left(\dot{m}_f + \dot{m}_{air}\right)h_{exh} \tag{45}$$

where the h_{exh} is the enthalpy of the exhaust gas, which is referenced to 298 K. The exhaust gas is a known mixture of numerous constituent species, thus the exhaust enthalpy is namely the mixture enthalpy determined from exhaust temperature and species concentrations. It should be noted that the heat of combustion is aggregated into the exhaust enthalpy for species that have not been completely oxidized, i.e. carbon monoxide (CO) and unburned hydrocarbon (HC) emissions.

The second control volume selected for this study (Fig. 13) specifies that the target exhaust energy is the energy corresponding to a pre-turbine temperature, but only the post-turbine gas temperature is attained from the experimental measurements. To better relate the experimentally derived exhaust energy to that calculated by the simulation, it is necessary to analyze the temperature difference or the difference of energy carried by the exhaust gas between pre-turbine and post-turbine. The difference in the energy between the two states consists of the work output from the turbine and the heat transfer between the turbo surfaces and the environment. Because of the lack of pre-turbine temperature and related gas velocity information, the turbine work cannot be directly calculated from the changes in stagnation enthalpies between the states; solving the work consumed by compressor (W_C), however, is more straightforward with Eq. (46) and the following assumptions:

- Negligible elevation difference;
- The surface heat losses across the compressor are usually small [28], which allows the compressor to be approximated as an adiabatic control volume.

$$\dot{W}_C = \dot{m}_{air}(h_{02} - h_{01}) \tag{46}$$

Given that the minimum work transfer rate produced by turbine is namely $\dot{W}_C$ when the mechanical efficiency of the turbocharger system is assumed to be 100%, the work output from the turbine can be consequently estimated from Eq. (46). The heat rejection from the turbine surfaces to the environment has been

investigated in [25], adding the total energy losses across the turbine, i.e., the sum of turbine work and surface heat losses, onto the exhaust enthalpy calculated from the post-turbine temperature yields the pre-turbine exhaust energy.

4.2.2 Energy Distributions

The methods described in the previous section are now applied to the experimental energy balance analyses by using the control volume shown by Fig. 13. These results are subject to the constraints of the experimental measurements and to the approximations involved in the methodology. This section compares the experimental results to the predictions from the simulation and attempts to explain the possible factors causing the disparities in the relevant energy terms.

Fig.14 compares the simulated energy fractions with the experimentally derived results for Case #4 (ECT = 90˚C). The comparisons for the remaining cases are displayed in the Appendix III, which appear to have similar pattern to that shown in Fig. 14. The changes in the three different energy flows with ECT are summarized in Fig. 15.

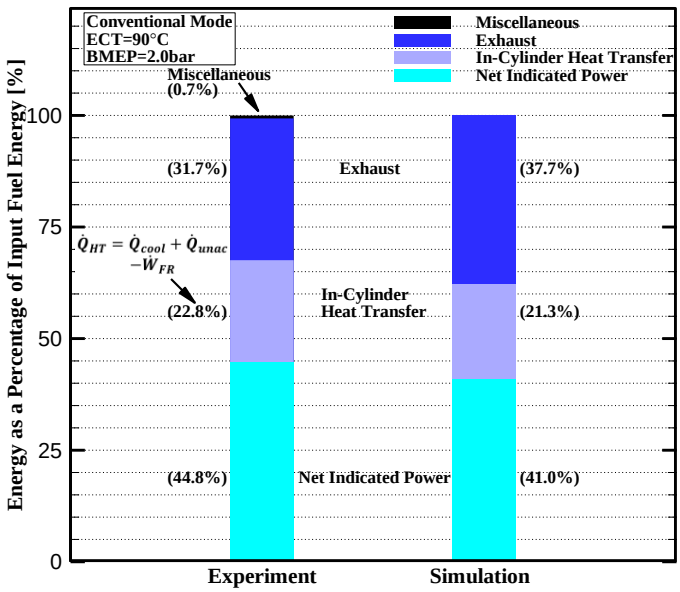

Fig. 14 Energy distributions of experiment and simulation for Case #4.

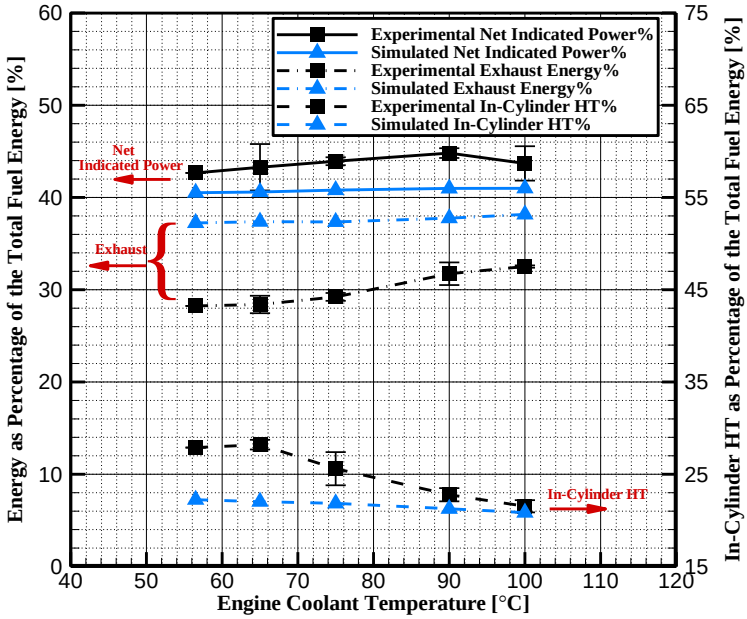

Fig. 15 Summarized energy distributions at five different ECTs (conventional mode).

In general, it is found from both simulation and experiment that more than 40% of the input fuel energy is converted into net indicated power. The net indicated power slightly increases as the ECT increases – more discussions on this will be detailed in Section 4.2.3 along with discussions of the fuel conversion efficiency. The simulation results of net indicated power fractions are underestimated by approximately 2–3%, which do not deviate from the experimental results as much as the other two terms (in-cylinder heat transfer and exhaust energy) do. Typically precise predictions in cylinder pressures can avoid significant inaccuracies of $W_{i,net}$, because the net indicated work is derived from the pressure-volume analysis (see Section 4.2.1). Because the simulated pressure is in good agreement with the validation data as indicated in Fig. 7, the uncertainties of the flow characteristics are suspected to be the primary reason causing the errors in predicted net indicated power [102].

Similar to the previous studies on LHR engines [36, 48, 49], raising ECT also yields gradually decreased net in-cylinder heat transfer. Compared to the term of net indicated power, there are more significant discrepancies in heat transfer existing between the simulation and experimentally derived results. The in-cylinder heat transfer fractions determined from Eq. (43) reveal to be higher than the simulation by about 2-6%. As discussed in the previous section, using Eq. (43) to estimate the in-cylinder heat transfer will likely result in substantial inaccuracies since the process tends to introduce additional errors from calculating $\dot{Q}_{cool}$ and $\dot{Q}_{unac}$. For example, the $\dot{Q}_{cool}$ is calculated based on the assumption of constant coolant properties, i.e., constant pressure specific heat. In addition, the friction power is obtained by subtracting brake power from net

indicated power rather than directly measuring from motoring engine. In this work, a more significant source of errors is likely to be the computation of $\dot{Q}_{unac}$. It is usually difficult to accurately capture the heat losses to the environment, especially when operating the engine under LHR conditions since higher engine surface temperature yields more radiative heat transfer occurring between external surfaces and the environment. In addition, the heat transfer coefficients used for the calculations are collected from empirical correlations. Because a direct measurement of heat flux is not available in this study, an alternative way to further examine the simulation results is calculating the cylinder heat transfer from measured pressures by using Hohenberg's correlation [103]. Fig. 16 compares the instantaneous heat transfer rates calculated from Hohenberg's model and the simulated rates predicted from WoschniGT model.

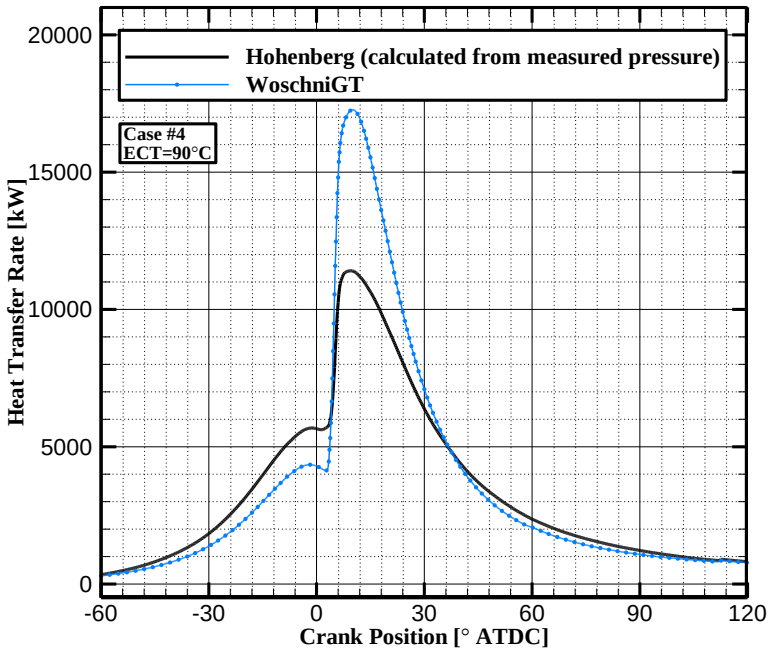

Fig. 16 Heat transfer rates predicted from Hohenberg and WoschniGT models.

The estimations from Hohenberg's correlation show to be higher than the WoschniGT simulation results during the compression stroke, but which are significantly lower as combustion starts. The average heat flux calculated from Hohenberg's correlation is lower than the WoschniGT simulation results by about 3–5%, see Fig. 17. These comparisons are consistent with previous studies on the heat transfer modeling between Hohenberg's model and the classic Woschni's model [103].

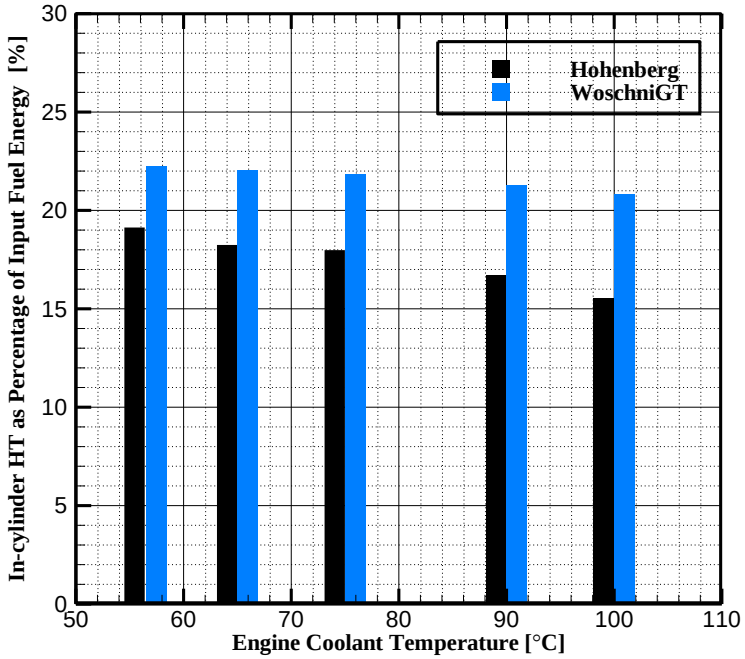

Fig. 17 Average heat transfer predicted from Hohenberg and WoschniGT models.

It should be noted that typically the heat transfer modeling does not account for heat transfer between the hot gases and valve back. The heat transferred from the gas through the intake/exhaust port walls is also excluded from both modeling results, which is unavoidably lumped into the experimental analyses due to the constraint in exhaust

temperature measurements. Therefore, the experimentally derived in-cylinder heat transfer is likely to be a little overestimated compared to the simulation results.

On the contrary, experimental exhaust energy fractions tend to be lower than the simulation results by 6–7%, which nearly offsets the disparity found in the heat transfer term. The methodology used to calculate experimental exhaust energy has been introduced in Section 4.2.1. The primary source of errors in the exhaust energy estimation is suspected to be the location of exhaust temperature measurement. Based on the energy systems depicted in Figs. 12 and 13, the actual exhaust energy should be calculated from the pre-turbine exhaust temperature. More specifically, the target temperature should be measured at a position near the exhaust valve or the upstream end of the exhaust manifold, i.e., State 1 shown in Fig. 18. As discussed previously, the post-turbine temperature (temperature at State 3, see Fig. 18) is the only available measurement from the instrumented engine. Although the experimental data has been corrected to be the pre-turbine exhaust energy (State 2), the experimentally calculated exhaust energy is still not a completely "parallel" reference to the simulation-based counterpart. The latter is, therefore, higher than the former due to the lower exhaust gas temperature used for the experimental analyses. As mentioned earlier, such a constraint in temperature measurement consequently causes the heat transfer occurring between exhaust gases and exhaust port walls to be counted toward the in-cylinder heat transfer in the experimental calculations, which yields a corresponding difference from the simulated heat transfer.

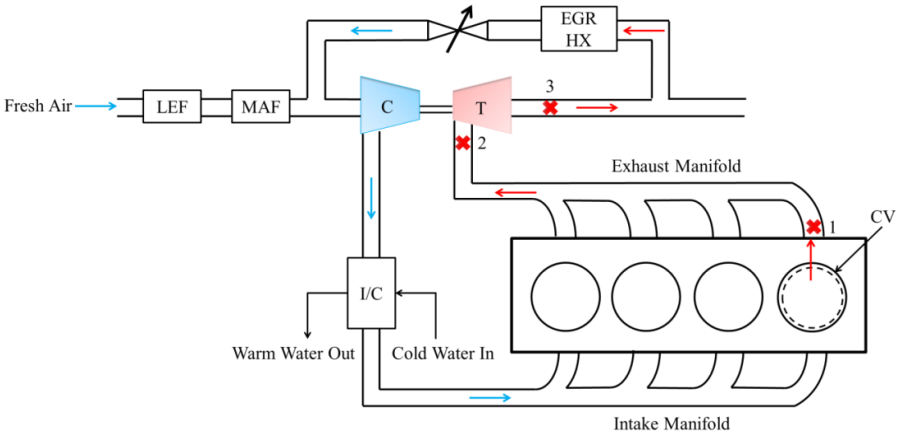

Fig. 18 Illustration of the turbocharged engine
1) target state, 2) pre-turbine, 3) post-turbine.

A sensitivity study was completed to evaluate how much the exhaust temperature affects the level of exhaust energy. Fig. 19 gives the exhaust energy fractions at different exhaust temperatures, where the baseline measurement refers to the result computed from the post-turbine exhaust temperature and the maximum temperature 500 K is set to be the simulated temperature at the target position, i.e. state 1. Changing the exhaust temperature, from post-turbine temperature 418 to 500 K, yields different exhaust energy fractions being denoted by the bars in Fig. 19, which tend to increase linearly with the temperature. Square symbols represent the relative changes in exhaust energy with respect to the baseline case, which appear to be about 2.5 times faster than the rate of relative change in exhaust temperature, as denoted by the triangle symbols. In general, the exhaust energy is shown to be very sensitive to the temperature. For Case #4, the exhaust energy fraction rises by 48.1% (from 25.1 to 37.2%) as the exhaust temperature relatively increases by 19.6% (from 418 to 500 K).

Such analysis confirms the need to have proper exhaust temperature measurement when calculating the exhaust enthalpy. Apart from the uncertainties

involved in experimental analyses, there are also some potential inaccuracies existing in the simulation work. For example, generally the combustion models provided by the engine simulation software do not have the capability to predict the hydrocarbon emissions for compression ignition engine models. This means that the simulated exhaust energy does not account for the portion carried by the unburned hydrocarbons.

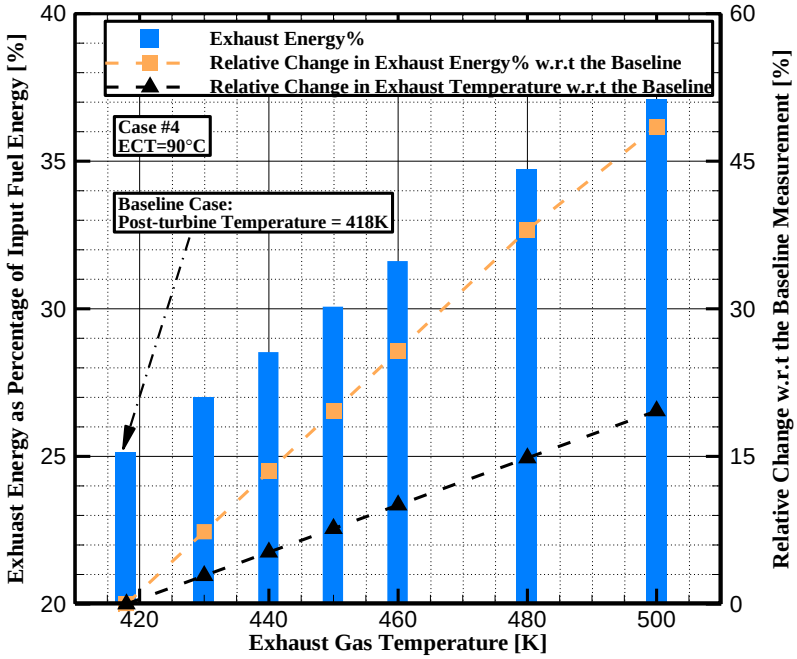

Fig. 19 Sensitivity study on exhaust temperature for ECT=90˚C (Case #4).

4.2.3 Fuel Conversion Efficiency

Similar to the BMEP changing with ECT as reported in Section 4.1.2, significant improvements in brake fuel conversion efficiency were observed in both the simulation and experimental studies, as shown in Fig. 20. The simulation results indicate that over

20% relative improvement in the brake fuel conversion efficiency (from 21.1 to 26.4%) is achieved as ECT changes from 56.5 to 100°C; the experimental results also indicate a similar level of improvement (~23.5%). The net indicated fuel conversion efficiency, however, reveals only slight improvement compared to the brake efficiency. Increasing ECT from 56.5 to 100 ˚C causes only 2.7% relative improvement in the experimental net indicated efficiency. Similar results were also found in the simulation study.

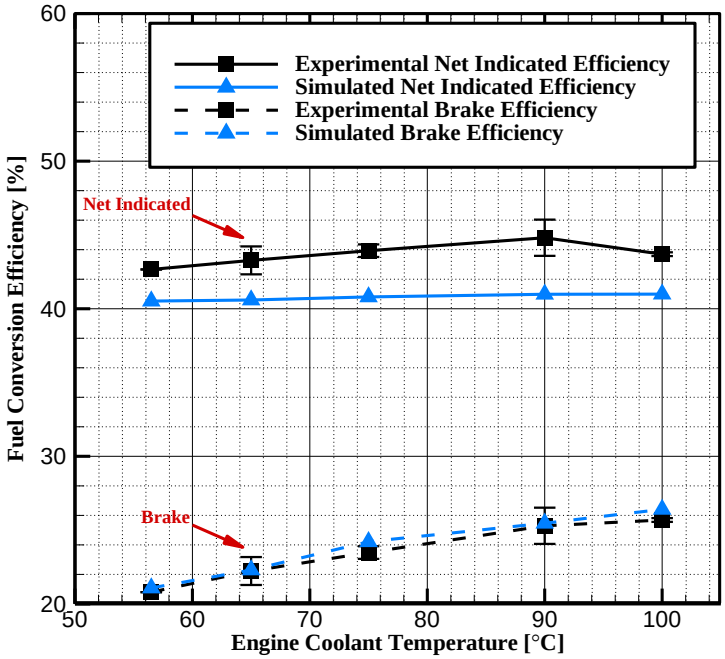

Fig. 20 Fuel conversion efficiencies as functions of ECT (conventional mode).

In general, the LHR application improves the fuel conversion efficiencies, which may be attributed to several beneficial phenomena caused by elevated ECT:

i. Reduced in-cylinder heat transfer resulting in higher gas temperatures promotes the combustion toward completeness. It has been reported in [26] that increasing

ECT reduces CO and HC pollutants. They serve as indicators of an increase in combustion efficiency. Such efficiency gains would be observed in both brake and indicated fuel conversion efficiencies. This may partly explain the slight increase in experimental indicated efficiency, which would not appear in the simulated indicated efficiency as the simulation does not capture CO and HC.

ii. Retained energy from the LHR operation yields shorter ignition delay (ID), which might result in an increased effective expansion ratio depending on the influence of ignition delay on the combustion duration. Fig. 21 shows how the ignition delay, defined as the interval between start of injection (SOI) and 10% mass fraction burned (MFB), and combustion duration (10–90% MFB) change with the engine coolant temperature. The ignition delay gradually decreases as ECT increases. The injection timing for the studied cases is constant at 8˚bTDC. The high-temperature condition facilitates the start of combustion to be advanced and consequently the ignition delay tends to become shorter at higher ECTs. A subsequent extension of the combustion duration is due to the shorter ignition delay causing the fraction of burned gases in the premixed combustion phase to reduce, and the fraction of diffusion combustion consequently increases. Generally, diffusion combustion burns at a slower rate such that, for a fixed amount of fuel, increased diffusion burning at the expense of premixed burning will increase the combustion duration. The predicted combustion durations deviate from validation data significantly, which likely results from the overestimated burn rates from the engine simulation. Fig. 22 compares the

experimental burn rates with that calculated by the engine simulation having a prescribed pressure history. This indicates that the engine simulation cannot achieve perfect MFB matching even with measured pressures as the input. It is likely because the simulation code is using different methodologies or assumptions to calculate the burn rate. Whereas the simulation results do characterize a variation pattern consistent with the experiment, providing clues to help explain the gains in engine efficiency. In summary, changes to combustion phasing will impact both indicated and brake efficiencies; even though combustion phasing may change slightly at various ECTs, the changes do not appear to be substantial enough to cause significant changes to indicated efficiency.

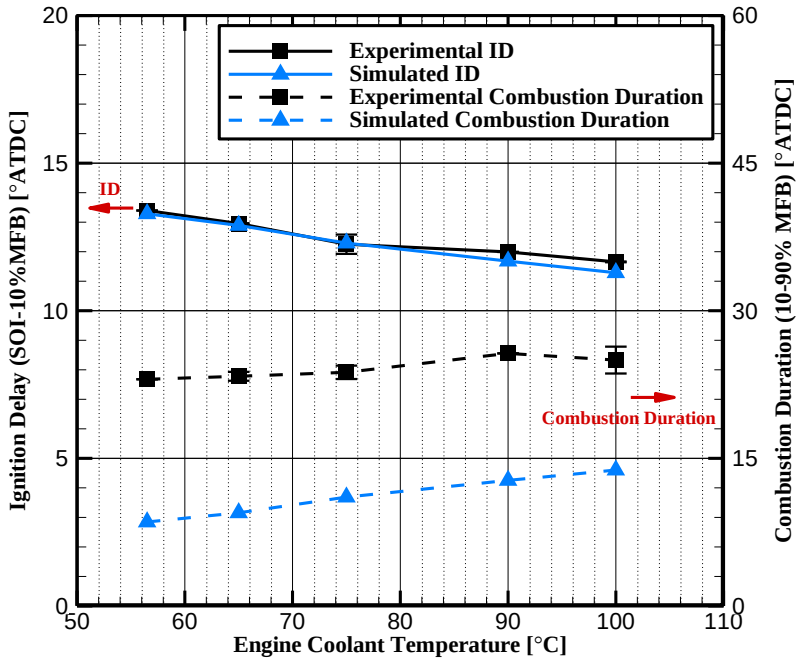

Fig. 21 Ignition delay and combustion duration as functions of ECT.

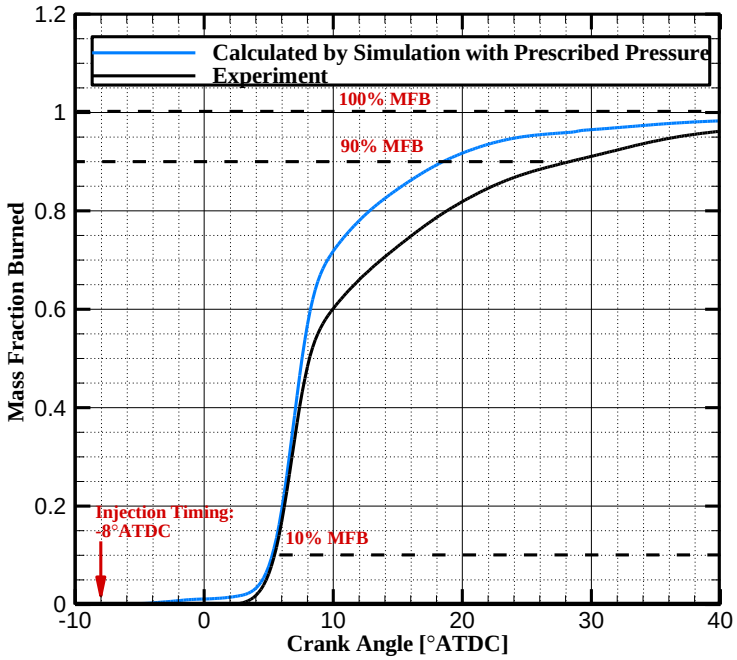

Fig. 22 Comparison of burn rates (mass fraction burned), Case #1.

iii. Frictional losses decrease at higher temperature conditions. For the conventional low load condition, the reduction in friction is likely to be the dominant factor causing the noticeable improvement in brake efficiency. Robinson [74] also points out that increasing the coolant temperature of a conventional cooling system usually yields a fuel consumption benefit via reduced crank train friction. This is perhaps due to lowered lubricant viscosity as wall and oil temperatures increase with higher ECTs, decreasing the hydrodynamic friction in bearings, valve trains, along liners, and in the oil pump.

5. LHR CONCEPT COMBINED WITH LTC ENGINE

The objective of the second phase of this study is to investigate how the engine performance will be affected by the interaction of elevated ECT and LTC operation. In the previous experimental investigations [25-27], five different ECTs varying from 75˚C to 100˚C have been studied in order to establish the trends in the improvements of fuel conversion efficiency and emissions. These results were further compared to that of conventional combustion mode to evaluate the benefits of integrating LTC and LHR. Therefore, this section is structured to discuss the difference in the effects of varying ECT on engine performance between the two modes. The general operating conditions of LTC mode are previously listed in Table 5.

5.1 LTC-LHR Engine Model

All the LTC cases are operated with EGR at roughly 35%, which is cooled by the EGR cooler prior to mixing with the fresh charged air. Because of the need of simulating EGR, the engine model used in the conventional combustion mode (see Fig. 3) needs to be modified with the EGR loop, as shown in Fig. 23. Compared to the conventional combustion mode, the LTC engine model can be used to model the engine operating at any arbitrary level of EGR, which is implemented via the EGR valve controller.

The EGR valve controller is used to attain the desired EGR rate by controlling the throttle angle – 35% is set as the target for each case in this study. Due to the lack of performance characteristics and geometry information of the actual EGR cooler, estimates are used by the simulation. Given that the target mass percent of EGR must be achieved as the EGR valve controller eventually converges, the uncertainties of cooler

structure therefore are of no concern to the model predictions if the temperature at the EGR cooler outlet is well calibrated. Essentially, the mass flow rate and temperature of the cooled EGR are the factors that mostly determine the mixing with freshly charged air; hence, inaccurate EGR cooler information supposedly does not influence the state of intake mixture and the subsequent combustion phasing. The EGR cooler of the LTC engine model therefore serves as a temperature corrector, which helps in achieving well-predicted post-EGR temperature in order to guarantee the accuracy of modeling intake mixing. The post-EGR cooler temperature is not directly measured from the instrumented engine, but can be experimentally determined from other available measurements at states of intake mixture and fresh air. The details of back-calculating the post-EGR cooler temperature are listed in the Appendix IV. When the geometric information of the EGR cooler is not available or not accurate, it is feasible to enable the LTC engine simulation by adjusting the heat transfer calibration constants of the "virtual" EGR cooler until post-EGR temperature matching is achieved.

The remaining objects and model components are almost the same as for the conventional model. Heat transfer between in-cylinder gas and the chamber walls is predicted from the same modified Woschni model "WoschniGT." The engine simulation software uses the same Chen-Flynn model to calculate engine friction. The combustion model "DI Pulse" is used to predict the combustion rate with the assumption of three thermodynamic zones. With given inputs and defined boundary conditions, sub-models (i.e., heat transfer model, combustion model, and friction model) are calibrated by

reproducing the experimental data at the five test points, i.e., Cases 6–10 listed in Table 5.

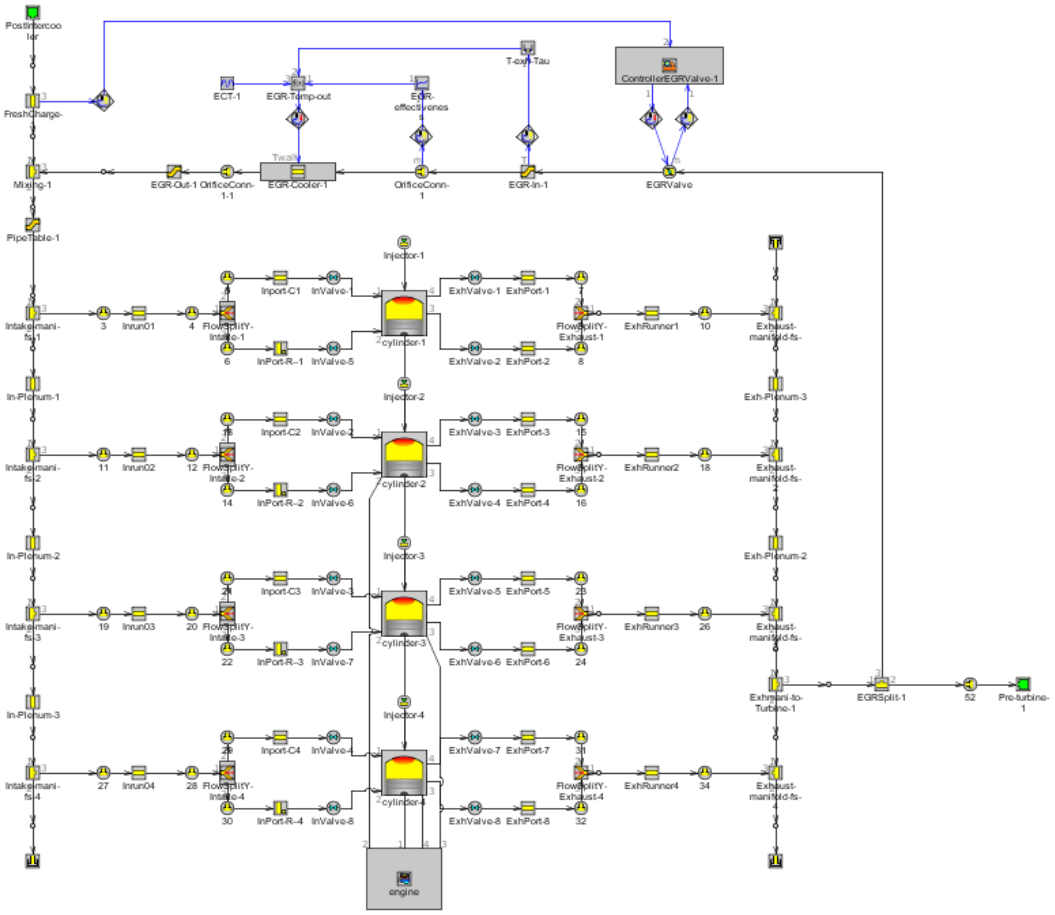

Fig. 23 Illustration of the engine model layout (LTC mode).

The simulated cylinder pressures and rates of heat release (ROHR) are compared to experimental results showing general agreements for all five cases (see Fig. 24 for Case #9). Similar shapes of cylinder pressure, ROHR profiles, and comparative behavior are also observed in cases of ECT = 90°C and ECT = 100°C, which are displayed in Appendix V. Different from these three cases, the combustion appears to be weaker as the ECT gets lower, as is shown in Fig. 25 where the ECT is 82.5°C. In contrast with the

results of Case #9, the predicted pressures of Case #7 are still mostly in agreement with the measured pressures. The simulation seems to slightly overestimate the ROHR and such discrepancy tends to be more significant as ECT reduces to 75°C, the comparison of which is also shown in Appendix V. It is inferred based on substantial calibration work that the built-in combustion model (DIPulse model) may not be fully capable of predicting weak or unstable combustion conditions. As it is observed in the conventional mode, these discrepancies in ROHR do not cause a major concern since much of the use of the simulation is to capture thermodynamic parameters of the engine system where precise match in pressure is the first priority.

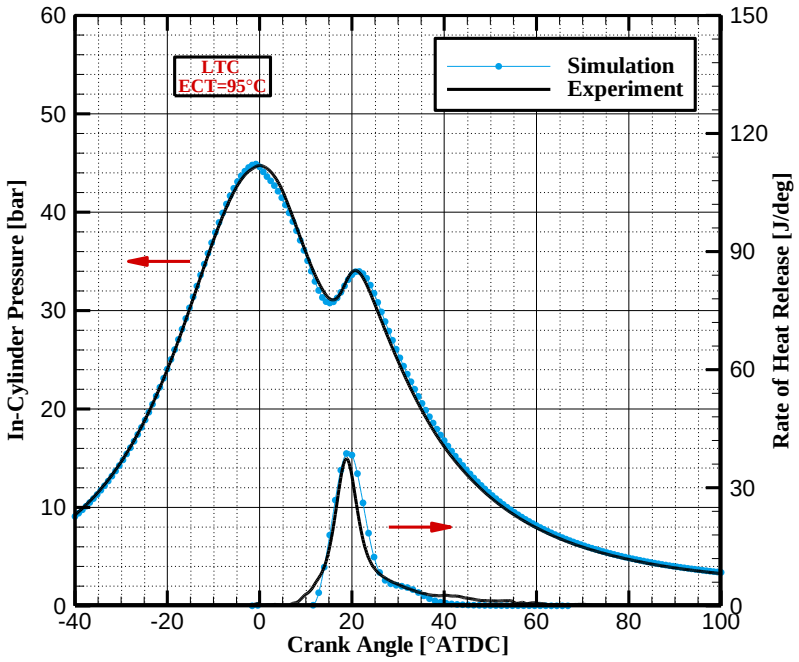

Fig. 24 Comparisons of cylinder pressure and ROHR for Case #9.

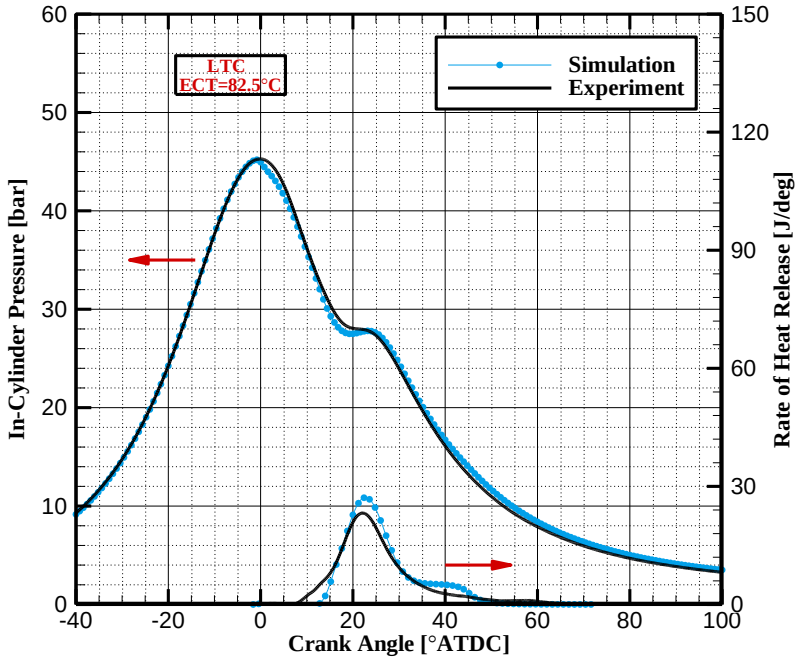

Fig. 25 Comparisons of cylinder pressure and ROHR for Case #7.

5.2 LHR-LTC Engine Simulation Validation

The simulation validation work for LTC mode will be addressed in this section from three major perspectives, i.e., flow characteristics, engine performance, and combustion phasing. In Section 4, the energy balance analyses are conducted to illustrate how varying ECT influences the energy fuel conversion efficiency, which provides the clues for the observed improvements in engine performance. In addition to the LHR-LTC engine simulation validation, this section will also compare the different levels of fuel economy improvements produced by the proposed LHR concept between conventional and LTC modes, and attempts to analyze the potential factors causing these differences based on the analyses of combustion phasing.

5.2.1 Flow Characteristics

i. Fig. 26 shows the predicted volumetric efficiency compared to the experimental calculations from Eq. (37). In general, the predictions are lower than experimental calculations by 5–8%. Both results show that the VE is maintained at around 60% as the level of EGR remains at 35%.

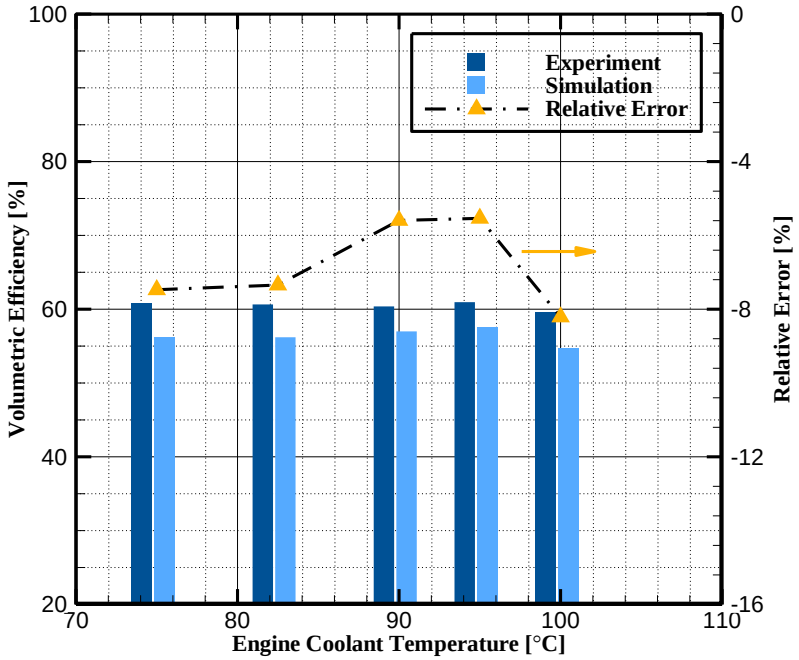

Fig. 26 Comparison of VE between simulation and experiment (LTC mode).

In addition to the potential inaccuracies in the engine model, particularly in the valve train characteristics, the estimated air density in the experimental calculations may likely yield slightly higher VE values than if the pressure of compressed air is used for the calculation. As mentioned in Section 4.1.1, one of the common concerns in traditional LHR engines is VE reduction, which limits

the improvement in the overall performance of LHR engines. Such a VE shortfall as ECT increases is also observed in the previously studied conventional-LHR mode, see Fig.9. The VEs under LTC-LHR mode, however, appear to be almost unchanging. Due to a significantly high level of EGR that is used to achieve LTC, the VE under this mode is likely to be less sensitive to the changes in ECT. It can be inferred from this result that the LTC-LHR combination seems to partly resolve the issue commonly existing in the traditional LHR engines.

ii. It has been mentioned in Section 5.1 that the mass flow rate and temperature of the cooled EGR influence the mixing of recirculated exhaust gas and fresh air, which in turn affects the combustion and engine performance. As a result, matching cooled EGR temperature is important for the validation of flow characteristics. Fig. 27 compares the simulation to the experimentally derived results; the predictions are consistently higher than the experimental calculations by less than 2%. With now the EGR% and cooled EGR temperature being validated, the following discussions will focus on parameters that are determined from the processes taking place in the cylinder.

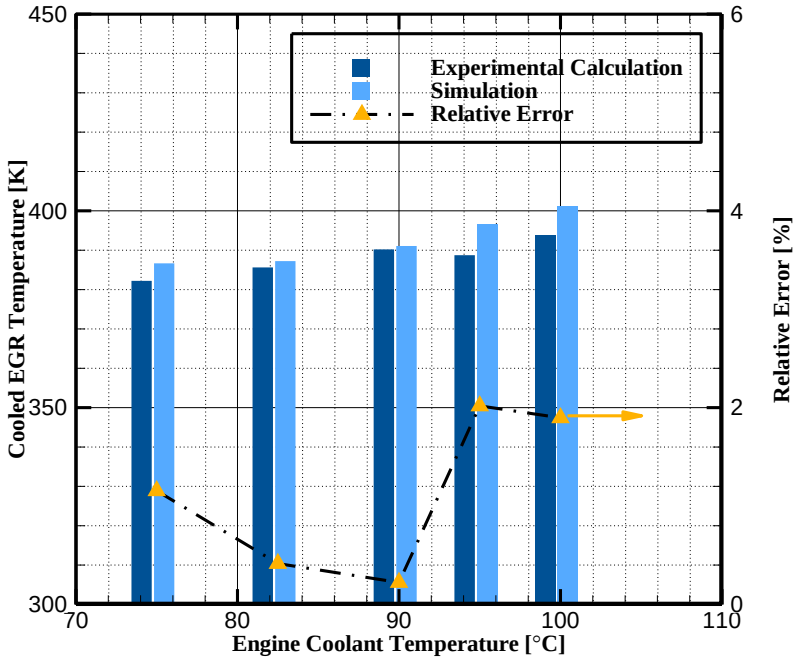

Fig. 27 Comparison of cooled EGR temperature between simulation and experiment.

5.2.2 Engine Performance

Analyses of mean effective pressure (MEP) and specific fuel consumption (SFC) are completed to examine the engine performance under LTC-LHR conditions. Figs. 28 and 29 show the indicated mean effective pressure (IMEP) and brake mean effective pressure (BMEP), respectively, changing as the ECT increases. Again, it should be noted that all the indicated quantities presented in this work refer to net indicated values instead of gross indicated values.

As it is shown in Fig. 28, the simulation tends to underestimate the IMEP by 2–8% except the first case of ECT = 75°C where the simulated IMEP is higher than its experimental counterpart by ~2%. The inaccuracies in predicted BMEPs are generally

within ±5%, see Fig. 6. In addition to the errors in previously discussed VE, these discrepancies are also likely caused by the uncertainties in some of the constituent model components, e.g., estimations of the valve lift profiles. Nevertheless, the simulation results show the consistent trend-wise behaviors with that observed from the experimental measurements. From ECT = 75 to 100°C, the IMEP increases from 2.43 to 3.13 bar, approximately 28.8% of IMEP gain. More significant gains in BMEP are achieved according to Fig. 6; the BMEP at 100°C is more than doubled as compared to the 0.87 bar at the minimum ECT. The increases in MEPs indicate the corresponding improvements in fuel conversion efficiencies and fuel economy (i.e., SFC), as shown by Figs. 30 and 31, respectively.

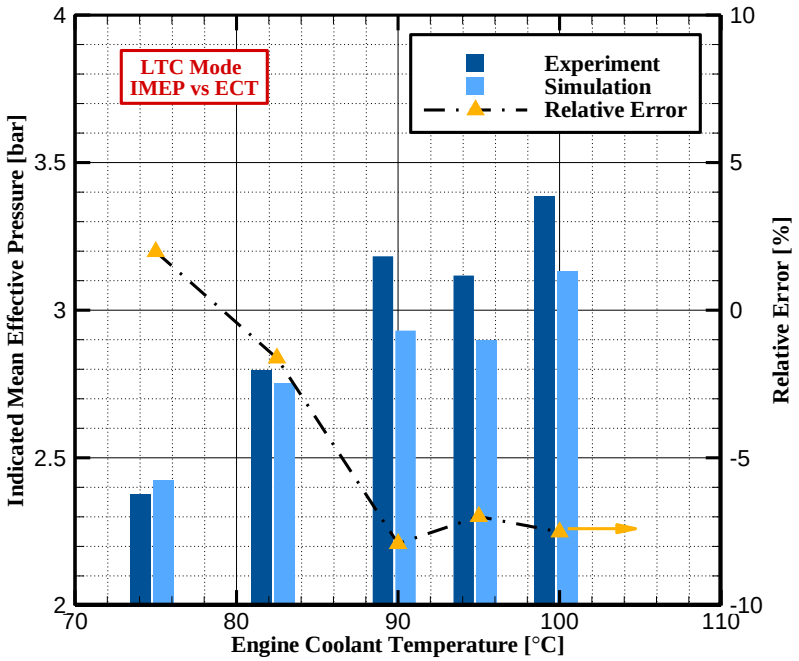

Fig. 28 IMEP changing as ECT (LTC mode).

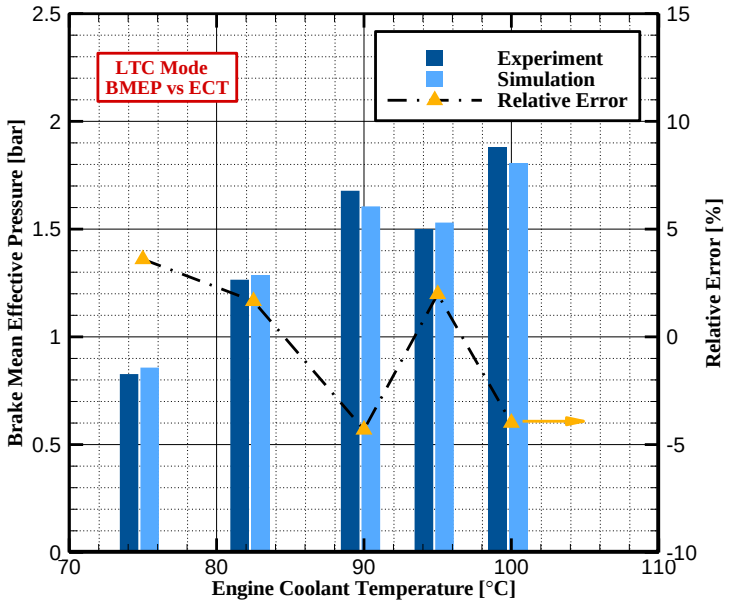

Fig. 29 BMEP changing as ECT (LTC mode).

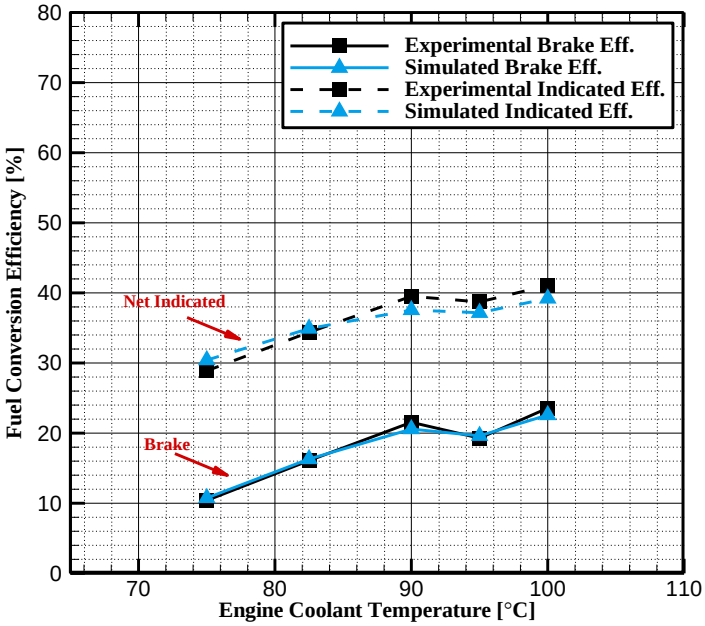

Fig. 30 Fuel conversion efficiencies changing as ECT (LTC mode).

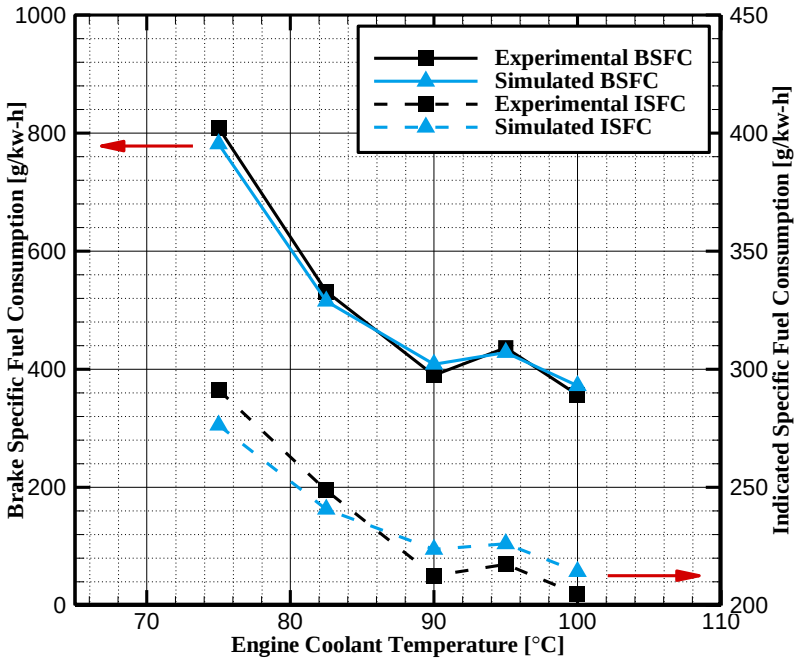

Fig. 31 Specific fuel consumptions changing as ECT (LTC mode).

The simulated efficiencies and SFCs show the same variation behaviors as experimental results. The indicated efficiency increases from 30.4% to 39.2% as the ECT changes from 75 to 100°C; similar to the gains in BMEP, the improvements in brake efficiency turns out to be more significant (from 10.8% to 22.6%). The SFC is correlated to efficiency through the following equation:

$$\eta = \frac{1}{SFC \times LHV} \tag{47}$$

where η refers to the fuel conversion efficiency, and LHV is the lower heating value of the fuel. Because LHV is typically constant, it is evident that the SFC is inversely proportional to fuel conversion efficiency. As a result, the SFCs correspondingly reduce as ECT increases, as shown in Fig. 31.

The previous studies on varying ECT in conventional combustion mode show that increasing ECT achieves insignificant improvements in indicated fuel conversion efficiency, the comparisons of indicated and brake efficiencies between conventional mode and LTC mode are shown in Figs. 32 and 33, respectively. As compared to conventional-LHR mode, raising ECT yields more drastic improvements in both MEPs and fuel conversion efficiencies in LTC-LHR mode, pointing to a higher sensitivity to variations in ECT. From Table 5, the injected fuel mass, engine speed, and injection timing are the same for these five conditions under LTC mode; since the EGR is maintained at ~35%, the nearly constant VE indicates that changes in air flow rate should be small. In particular, the changes in ECT under LTC mode (varying from 75 to 100°C) are even smaller than in conventional mode, i.e., 56.5–100°C. In this case, the interesting question is what makes the huge difference/improvement in LTC engine performance with such small increase in ECT. This question will be answered in the following section.

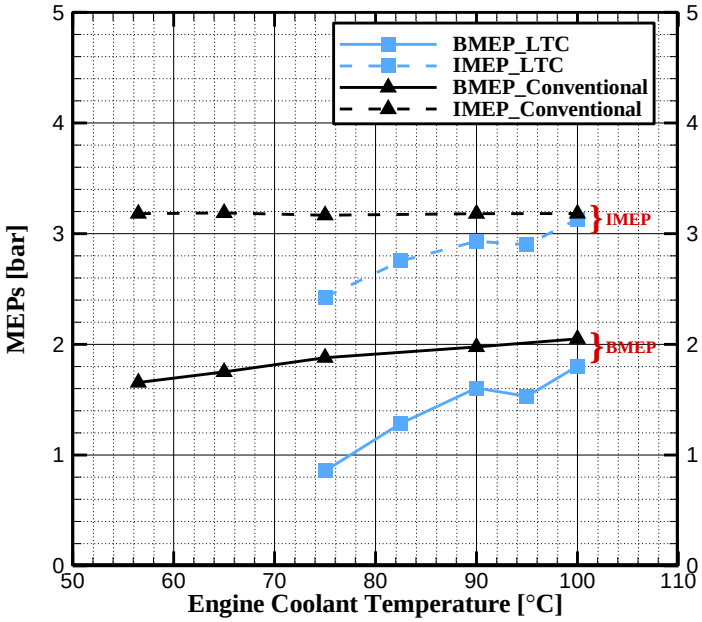

Fig. 32 MEPs comparison between two modes.

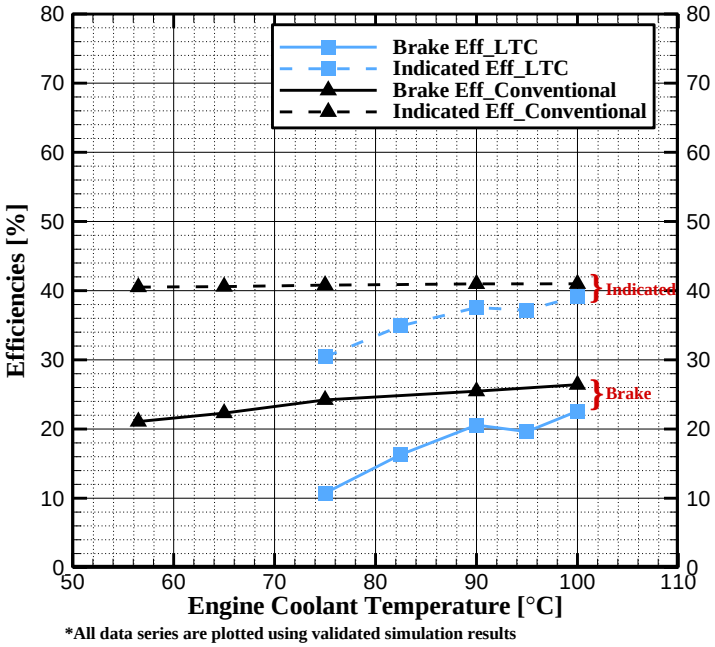

Fig. 33 Efficiencies comparison between two modes.

5.2.3 Combustion Phasing

Combustion phasing is known to influence the thermal efficiency because the cylinder pressure due to combustion yields the production of engine work. From the comparison between Figs. 24 and 25, it can be seen that the combustion at higher ECT is more intense than that at lower ECT under LTC mode. This section is therefore structured to provide some insights on the question posed in the previous section with the findings on the phasing of the combustion event.

Combustion phase is a relatively complex term/phenomenon which includes start of combustion, ignition delay period, rate of pressure rise, etc. For compression ignition engines, the combustion process is further divided into three stages: premixed combustion phase, mixing-controlled combustion phase (diffusion combustion phase), and late combustion phase [2]. In this study, the 50% of mass fraction burned (CA50) point was used to represent the combustion phasing; CA50 has been recognized to play a key role in LTC operation through other work [104-106]. Phase of CA10 and CA90 reflect 10% and 90% of mass fraction burned (MFB), which are regarded as start of combustion and end of combustion. The combustion duration therefore is defined as the interval of CA10 and CA90, termed as B1090 in this work.

The validation work on LTC engine model combustion predictions is shown in Figs. 34 and 35. Fig. 34 shows the gradual decreases in both CA10 and CA50 as ECT increasing. The trend-wise behaviors observed from simulation are in good agreement with experimental results, and the maximum deviation is ~2.5 crank angle degrees (CADs) in CA10. The deviations of predicted B1090 from dyno data shown in Fig. 35

are also observed in conventional mode, which have been analyzed in Section 4.2.3 primarily pointing toward the difference in the burn rate calculation methodology or assumptions used by the simulation code. Because the injection timing is constant, the advanced CA10 indicates shorter ignition delay (ID) at elevated ECTs, which can be seen from Fig. 12 where the solid lines represent the ignition delay period. In the meantime, the CA50 is also getting more advanced as the ECT increases. In Fig.11, it can be inferred from the gap between solid lines (CA50) and dashed lines (CA10) that the duration of the first-stage combustion from CA10 to CA50 is shorter at higher ECTs, which explains the reason why the premixed combustion rate is faster at higher temperature conditions, as shown by the comparison of ROHR profiles between Figs. 1 and 2. The cylinder pressure rise is known to be caused by combustion and volume change; the faster premixed combustion rate yields the significantly higher peak pressure (after TDC), which partly contributes to more engine work output. Consequently, the application of LHR in LTC engines results in the observed improvements of MEPs shown in Figs. 28 and 29.

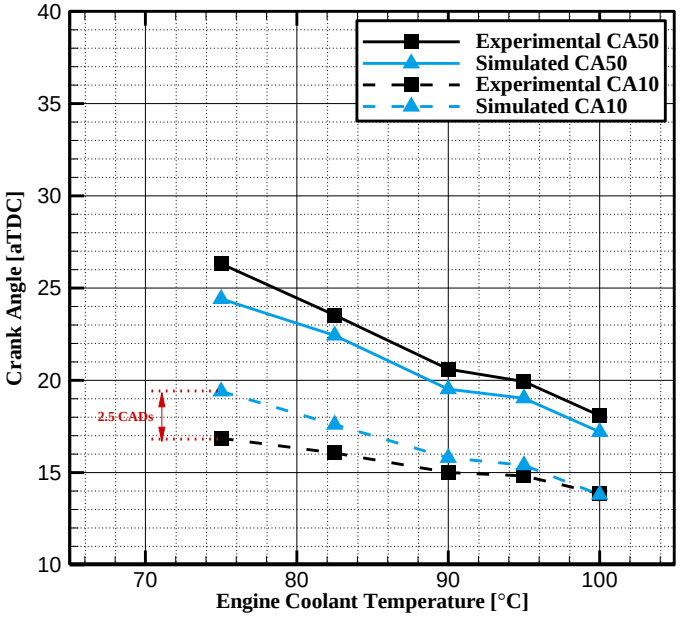

Fig. 34 CA50 and CA10 changing as ECT (LTC mode).

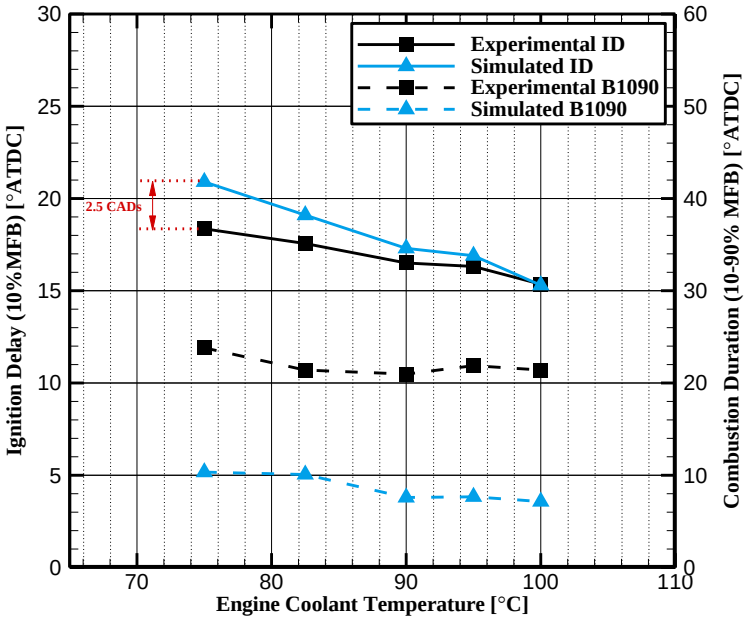

Fig. 35 ID and B1090 changing as ECT (LTC mode).

Generally the combined effects of incomplete combustion, heat transfer losses, and exhaust losses contribute to the indicated fuel conversion efficiency. The LHR operation tends to increase the exhaust losses due to increased exhaust gas temperature. The combustion efficiency gradually decreases with retarded CA50 [107]. Such conclusion has been verified by the studied LTC-LHR operation, as shown in Fig. 36; in contrast, the favorable effects of elevated ECT on combustion efficiency are not yet seen in the conventional-LHR mode. The combustion efficiencies plotted in Fig. 36 come from experimental data due to the lack of unburned HC predictions in simulation engine. The combustion model provided by the simulation software does not include HC emission model. Since the combustion duration B1090 remains to be almost constant under the LTC-LHR operation, as seen in Fig. 35, the heat transfer duration is expected to be not too much different as ECT increases; in this case, the in-cylinder heat transfer will reduce due to the smaller temperature difference between cylinder gases and combustion chamber walls at high ECTs. The researches by Rezaei et al. [105] and Caton [108] suggest that CA50 around 10° aTDC would lead to higher/optimal thermal efficiency, the CA50 trend shown in Fig. 11 seems to develop towards the suggested value if the ECT keeps increasing much more. Based on the discussions above, the favorable changes in combustion phasing (particularly advanced CA50) and increase in combustion efficiency are ascribed to the significant improvements in fuel conversion efficiencies of the proposed LTC-LHR strategy.

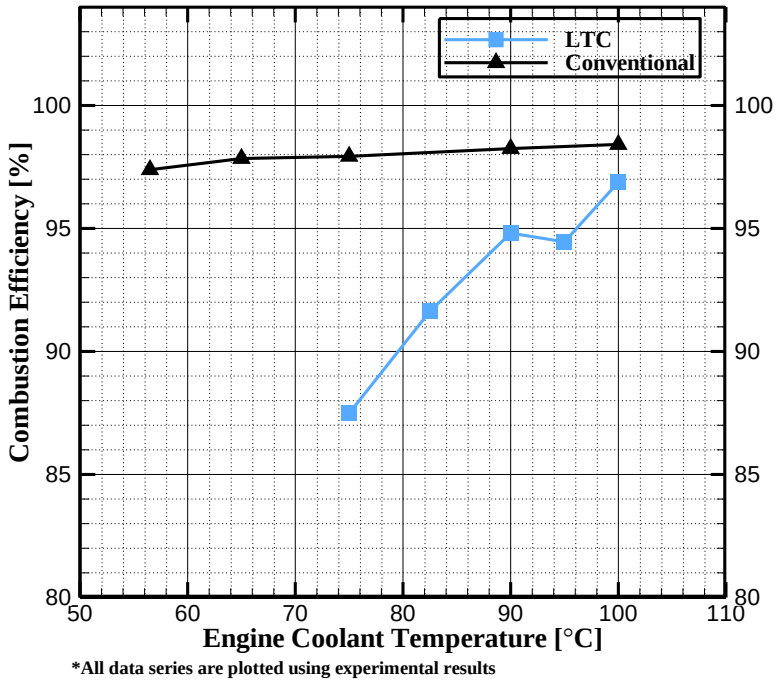

Fig. 36 Combustion efficiency changing as ECT under different modes.

With now the combustion predictions in LTC mode being validated against experimental data, the comparison of phasing between two modes are carried out in Figs. 37 and 38 to further explain why varying ECT yields more significant changes to the LTC mode than it does to the conventional mode. As it can be seen in Fig. 37, CA50 is advancing by almost 7 CADs as ECT increases from 75 to 100°C under the LTC mode; the conventional mode, however, appears to have only ~1° of advancement with the same level of variation in ECT. Similarly, the significant difference in ignition delay is also observed in Fig. 38 indicating a higher sensitivity to ECT variations for LTC mode. From the aforementioned discussions, the combustion phasing is considered to be closely correlated with the MEPs and fuel conversion efficiencies. Different from the

LTC mode, the phasing of the conventional combustion events seems to be almost unchanging as ECT increases. As a result, the proposed LHR strategy by varying ECT produces promising improvements in engine performance for LTC mode while relatively insignificant improvements seen in conventional mode. The corresponding variations in cylinder pressures of the two modes are shown in Figs. 39 and 40, respectively.

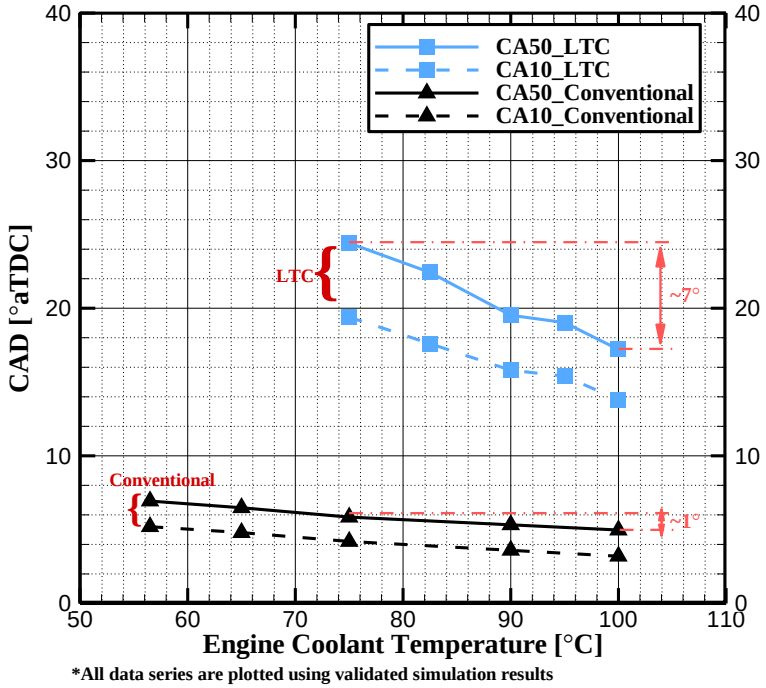

Fig. 37 CA50 and CA10 comparisons between two modes.

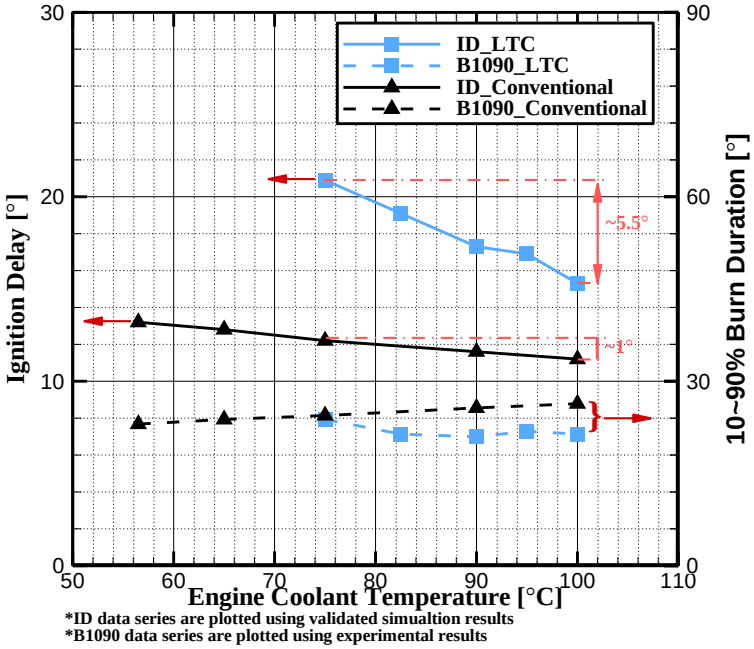

Fig. 38 ID and B1090 comparisons between two modes.

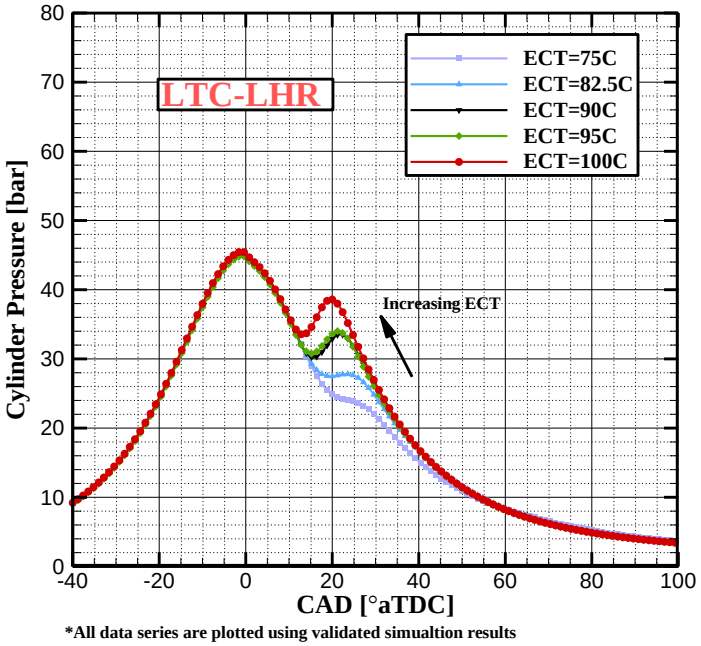

Fig. 39 Cylinder pressure changing as ECT (LTC mode).

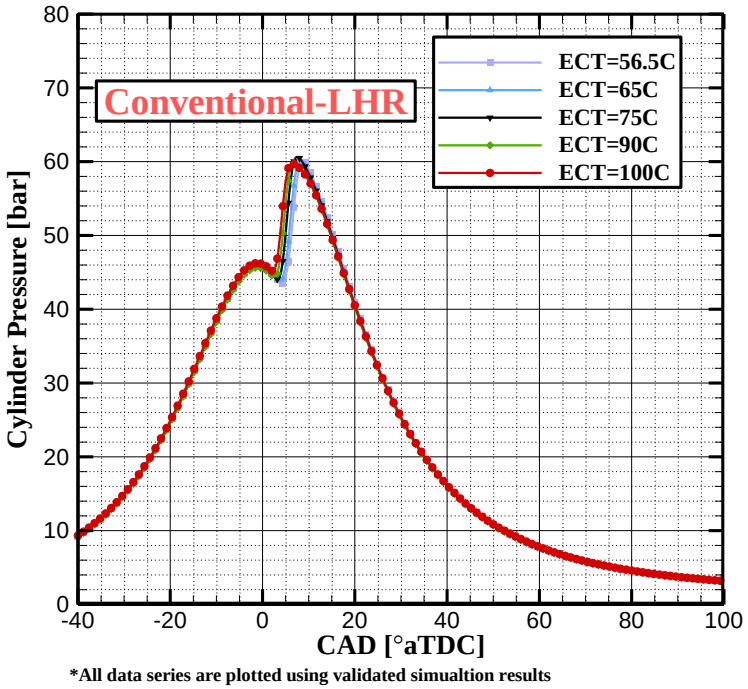

Fig. 40 Cylinder pressure changing as ECT (conventional mode).

6. SUMMARY AND CONCLUSIONS

6.1 Summary

The current study examined the use of increasing engine coolant temperature for a light-duty diesel engine to devise a version of LHR engine. A simulation-based investigation for conventional combustion mode and LTC mode was completed to reproduce experimental cases having different ECTs, a systematic calibration methodology was developed for engine model validation work. This study also quantified the potential improvements of engine performance and fuel conversion efficiency by the use of the proposed LHR concept under both combustion modes.

For the conventional combustion mode, simulated cylinder pressure and ROHR profiles and experimental data are compared to evaluate the combustion prediction capabilities of the engine simulation, which indicate good agreement in pressure; the discrepancies in ROHR are small and do not cause concern as cylinder pressure is the primary parameter influencing the thermodynamics of interests in this study. The effects of ECT on engine operating parameters including VE, MEPs, and RGF were further discussed. Then, with the use of combustion chamber based control volume, a comparative study between simulation and experiment was further carried out to investigate the disposition of initial input energy at different ECTs. Due to the constraints involved in the measurements, the methodology used for the experimental energy balance analyses was carefully scrutinized to better analyze the simulation results.

The objective of the second phase of this study is to computationally investigate how the engine performance will be affected by the interaction of elevated ECT and LTC operation. The conventional-LHR engine model was slightly modified to further simulate the version of LTC-LHR engine where ECT was increased from 75°C to 100°C. The predicted cylinder pressures are also in good agreement with the measured pressures, and noticeable discrepancies in ROHR profile are observed. It can be seen from the pressure trace and ROHR that the combustion tends to be weaker at lower ECTs, the heat release rate and pressure rise due to combustion show to be considerably small particularly at 75 and 82.5°C.

A comparative study between conventional-LHR engine and LTC-LHR engine was further carried out to investigate the influences of ECT in combustion phasing based on 1-D simulation method. Different from implementing LHR into conventional combustion mode, the results show that increasing ECT yields more significant improvements in fuel conversion efficiency under LTC-LHR mode, pointing to a higher sensitivity to variations in ECT. The potential reasons causing the difference in engine performance are also addressed from the perspective of combustion phasing changing as ECT.

6.2 Conclusions

6.2.1 Conventional-LHR Engine

i. Simulated BSFC and brake fuel conversion efficiency improved by 16.07% (from 382.4 to 320.9 g/kWh) and 19.14% (from 21.97 to 26.19%), respectively, when raising ECT from 56.5 to 100°C; the application of LHR concept also results in lowered ISFC and increased indicated fuel conversion efficiency. However, the improvement in indicated fuel conversion efficiency was proved to be insignificant.

ii. Both the experimental and simulation results indicate that more than 40% of the input fuel energy is converted to net indicated work, about 1/3 of the energy is rejected to the exhaust gases and the rest is transferred as thermal energy through the combustion chamber walls. Regarding to the net indicated power as a percentage of the total fuel energy, simulation results are generally in agreement with the validation data. Noticeable disparities were found in exhaust energy fractions due to the constraint of the exhaust temperature measurement, which also partly causes the likely overestimation of experimental in-cylinder heat transfer. Potential uncertainties involved in the engine simulation are also examined to explain the observed disparities.

iii. It is found that increasing ECT yields reduction in cylinder heat transfer but almost equivalent increase in the exhaust losses, which explained why varying ECT achieves slight improvements in net indicated fuel conversion efficiency. The brake fuel conversion efficiency, however, shows to be significantly

improved at the higher ECT conditions where the substantial reductions in frictional losses may occur, which may be partly caused by the associated gains in combustion efficiency, effective expansion ratio and friction at higher ECTs.

6.2.2 LTC-LHR Engine

i. The application of LHR (using increasing ECT) produces significant improvements in MEPs and fuel conversion efficiencies. Approximately 28.8% of indicated efficiency and 110.0% of brake efficiency gains are achieved as ECT increases from 75 to 100°C. The changes in IMEP are suspected to be primarily resulted from the favorable combustion phasing at elevated ECT. The change in BMEP is due to a combination of the improved IMEP and reduced FMEP, which is calculated from a correlation thus should be carefully scrutinized. The results show that CA50 is gradually shifting toward TDC as ECT increases, i.e., advanced CA50 at high ECTs. The advanced CA50 and shorter ignition delay period promotes the burn rate, especially premixed combustion rate, to be faster; in addition, advanced CA50 also potentially benefits for combustion efficiency. As a result, the combined effects of LTC-LHR on the combustion phasing contribute to the observed gains in engine performance.

ii. Both the simulation and experimental results show that the volumetric efficiency is almost maintained at 60% due to the use of high-level of EGR (~35%). Different from conventional LHR engines, the decrease in volumetric efficiency was not observed in the LTC-LHR operation. It indicates that the LTC

combining with LHR likely compensate the undesired influences in engine performance caused by LHR.

iii. By comparing the effects of varying ECT on combustion phasing between LTC and conventional modes, it can be concluded that CA50 and ignition delay have higher sensitivities to changes in ECT under LTC conditions. As a result, the proposed LHR concept is considered to be more promising as being coupled with LTC engine as developing high-efficiency engine technologies.

Although the reduction of heat transfer by raising ECT is limited in this work, these results offer a promising vision for extended studies on LTC-LHR concept. Further studies exploring the application of the proposed technique to different load conditions would be helpful in better understanding the feasibilities of this technology.

REFERENCES

[1] Caton JA. Thermodynamic considerations for advanced, high efficiency IC engines. Journal of Engineering for Gas Turbines and Power. 2014;136(10).

[2] Heywood JB. Internal combustion engine fundamentals: McGraw-Hill; 1988.

[3] Smith P, Heywood J, Cheng W. Effects of compression ratio on spark-ignited engine efficiency. SAE Technical Paper 2014-01-2599; 2014.

[4] Funayama Y, Nakajima H, Shimokawa K. A study on the effects of a higher compression ratio in the combustion chamber on diesel engine performance. SAE Technical Paper 2016-01-0722; 2016.

[5] Caton JA. A comparison of lean operation and exhaust gas recirculation: thermodynamic reasons for the increases of efficiency. SAE Technical Paper 2013-01-0266; 2013.

[6] Osada H, Uchida N, Shimada K, Aoyagi Y. Reexamination of multiple fuel injections for improving the thermal efficiency of a heavy-duty diesel engine. SAE Technical Paper 2013-01-0909; 2013.

[7] Nathan S, Mallikarjuna JM, Ramesh A. An experimental study using single and multiple injection strategies in a diesel fuelled HCCI engine with a common rail system. The Automotive Research Association of India; 2009.

[8] Aoyagi Y, Osada H, Misawa M, Goto Y, Ishii H. Advanced diesel combustion using of wide range, high boosted and cooled EGR system by single cylinder engine. SAE Technical Paper 2006-01-0077; 2006.

[9] Aoyagi Y, Yamaguchi T, Osada H, Shimada K, Goto Y, Suzuki H. Improvement of thermal efficiency of a high-boosted diesel engine with focus on peak cylinder pressure. International Journal of Engine Research. 2011;12:227-37.

[10] Woods M, Kamo R, Bryzik W. High Pressure Fuel Injection for High Power Density Diesel Engines. SAE Technical Paper 2000-01-1186; 2000.

[11] Deng J, Stobart R. BSFC Investigation using variable valve timing in a heavy duty diesel engine. SAE Technical Paper 2009-01-1525; 2009.

[12] Parvate-Patil GB, Hong H, Gordon B. Analysis of Variable Valve Timing Events and Their Effects on Single Cylinder Diesel Engine. SAE Technical Paper 2004-01-2965; 2004.

[13] Reitz RD, Duraisamy G. Review of high efficiency and clean reactivity controlled compression ignition (RCCI) combustion in internal combustion engines. Progress in Energy and Combustion Science. 2015;46:12-71.

[14] Bowman CT. Kinetics of pollutant formation and destruction in combustion. Progress in Energy and Combustion Science. 1975;1:33-45.

[15] Cornelius W, Wade WR. The formation and control of nitric oxide in a regenerative gas turbine burner. SAE Technical Paper 700708; 1970.

[16] Mellor AM. Emissions from continuous combustion system. In: Walter Cornelius WGA, editor. Warren, Michigan: Springer; 1971.

[17] Ya. B. Zeldovich PYS, and D. A. Frank-Kamenetskii. Oxidation of nitrogen in combustion. Moscow-Leningrad: Academy of Sciences of USSR; 1947.

[18] Tree DR, Svensson KI. Soot processes in compression ignition engines. Progress in Energy and Combustion Science. 2007;33:272-309.

[19] Glassman I. Soot formation in combustion processes. Symposium (International) on Combustion. 1989;22:295-311.

[20] Ciajolo A, D'Anna A, Barbella R, Tregrossi A, Violi A. The effect of temperature on soot inception in premixed ethylene flames. Symposium (International) on Combustion. 1996;26:2327-33.

[21] Li T, Ogawa H. Analysis of the trade-off between soot and nitrogen oxides in diesel-like combustion by chemical kinetic calculation. SAE Int. J. Engines 5(2):94-101; 2011.

[22] Kamimoto T, Bae M-h. High combustion temperature for the reduction of particulate in diesel engines. SAE Technical Paper 880423; 1988.

[23] S. Gowthaman APS. A review of Homogeneous charge compression ignition (HCCI) engine. International Journal of Scientific & Engineering Research. 2015;6:779-98.

[24] Alriksson M, Denbratt I. Low temperature combustion in a heavy duty diesel engine using high levels of EGR. SAE Technical Paper 2006-01-0075; 2006.

[25] Penny MA. Efficiency improvements with low heat rejection concepts applied to low temperature combustion (MS thesis). College Station, Texas: Texas A&M University; 2014.

[26] Penny MA, Jacobs TJ. Efficiency improvements with low heat rejection concepts applied to diesel low temperature combustion. International Journal of Engine Research. 2015;17:631-45.

[27] Penny MA, Jacobs TJ. Energy balance analysis to assess efficiency improvements with low heat rejection concepts applied to low temperature combustion. Combustion Science and Technology. 2017;189:595-622.

[28] Wade WR, Havstad PH, Ounsted EJ, Trinker FH, Garwin IJ. Fuel economy opportunities with an uncooled DI diesel engine. SAE Technical Paper 841286; 1984.

[29] Wallace FJ, Way RJB, Vollmert H. Effect of partial suppression of heat loss to coolant on the high output diesel engine cycle. SAE Technical Paper 790823; 1979.

[30] Thring RH. Low heat rejection engines. SAE Technical Paper 860314; 1986.

[31] Reddy CS, Domingo N, Graves RL. Low heat rejection engine research status: Where do we go from here? SAE Technical Paper 900620; 1990.

[32] Pawar AN, Jajoo BN, Nandgaonkar MR. Combustion analysis and performance of low heat rejection diesel engine with different thermal insulation coating. The Automotive Research Association of India; 2004.

[33] Islam R, Subrahmanyam JP, Babu MKG. Computer simulation studies of an alcohol fueled low heat rejection direct injection diesel engine. SAE Technical Paper 972976; 1997.

[34] Miyairi Y. Computer simulation of an LHR DI diesel engine. SAE Technical Paper 880187; 1988.

[35] Tovell JF. The reduction of heat losses to the diesel engine cooling system. SAE Technical Paper 830316; 1983.

[36] Morel T, Keribar R, Blumberg PN, Fort EF. Examination of key issues in low heat rejection engines. SAE Technical Paper 860316; 1986.

[37] Savliwala MN, Hakim NS. Statistically optimized performance predictions of low heat rejection engines with exhaust energy recovery. SAE Technical Paper 860315; 1986.

[38] Gatowski JA, Jones JD, Siegla DC. Evaluation of the fuel economy potential of the low-heat-rejection diesel engine for passenger-car application. SAE Technical Paper 870024; 1987.

[39] Sharma JK, Gaur RR. Some analytical investigations on a four stroke diesel engine for high specific output and low heat rejection. SAE Technical Paper 900618; 1990.

[40] Kamo R, Bryzik W. Cummins/TACOM advanced adiabatic engine. SAE Technical Paper 840428; 1984.

[41] Hoag KL, Brands MC, Bryzik W, Army US. Cummins/TACOM adiabatic englue program. SAE Technical Paper 850356; 1985.

[42] Cole RM, Alkidas AC. Evaluation of an air-gap-insulated piston in a divided-chamber diesel engine. SAE Technical Paper 850359; 1985.

[43] Schwarz E, Reid M, Bryzik W, Danielson E. Combustion and performance characteristics of a low heat rejection engine. SAE Technical Paper 930988; 1993.

[44] Woschni G, Spindler W. Heat transfer with insulated combustion chamber walls and its influence on the performance of diesel engines. Journal of Engineering for Gas Turbines and Power. 1988;110:482-8.

[45] Alkidas AC. Performance and emissions achievements with an uncooled heavy-duty, single-cylinder diesel engine. SAE Technical Paper 890144; 1989.

[46] Mahmoud AH, Saeed MN, Attia AE, Abdelfattah AI. Spray visualization in a partially insulated combustion chamber and performance of a low heat rejection diesel engine. SAE Technical Paper 920839; 1992.

[47] Kawamura H, Higashino A, Sekiyama S. Combustion and combustion chamber for a low heat rejection engine. SAE Technical Paper 960506; 1996.

[48] Kamo R, Mavinahally NS, Kamo L, Bryzik W, Schwartz EE. Injection characteristics that improve performance of ceramic coated diesel engines. SAE Technical Paper 1999-01-0972; 1999.

[49] Modi AJ, Gosai DC. Experimental study on thermal barrier coated diesel engine performance with blends of diesel and palm biodiesel. SAE Int. J. Fuels Lubr. 3(2):246-259; 2010.

[50] Caton JA. Thermodynamic advantages of low temperature combustion (ltc) engines using low heat rejection (LHR) concepts. SAE Technical Paper 2011-01-0312; 2011.

[51] Caton JA. On the importance of specific heats as regards efficiency increases for highly dilute ic engines. Energy Conversion and Management. 2014;79:146-60.

[52] Tunér M. Studying the potential efficiency of low heat rejection HCCI engines with a stochastic reactor model. SAE Technical Paper 2009-24-0032; 2009.

[53] Büyükkaya E, Engin T, Cerit M. Effects of thermal barrier coating on gas emissions and performance of a lhr engine with different injection timings and valve adjustments. Energy Conversion and Management. 2006;47:1298-310.

[54] Hoag KL. Measurement and analysis of the effect of wall temperature on instantaneous heat flux. SAE Technical Paper 860312; 1986.

[55] Torregrosa AJ, Olmeda P, Martín J, Degraeuwe B. Experiments on the influence of inlet charge and coolant temperature on performance and emissions of a DI diesel engine. Experimental Thermal and Fluid Science. 2006;30:633-41.

[56] Burke R, Brace C. The effects of engine thermal conditions on performance, emissions and fuel consumption. SAE Technical Paper 2010-01-0802; 2010.

[57] Christensen M, Johansson B. Influence of mixture quality on homogeneous charge compression ignition. SAE Technical Paper 982454; 1998.

[58] Christensen M, Johansson B. Supercharged homogeneous charge compression ignition (HCCI) with exhaust gas recirculation and pilot fuel. SAE Technical Paper 2000-01-1835; 2000.

[59] Yao M, Chen Z, Zheng Z, Zhang B, Xing Y. Study on the controlling strategies of homogeneous charge compression ignition combustion with fuel of dimethyl ether and methanol. Fuel. 2006;85:2046-56.

[60] Dec JE. Advanced compression-ignition engines—understanding the in-cylinder processes. Proceedings of the Combustion Institute. 2009;32:2727-42.

[61] Eng JA. Characterization of pressure waves in HCCI combustion. SAE Technical Paper 2002-01-2859; 2002.

[62] Doosje E, Willems F, Baert R, Van Dijk M. Experimental study into a hybrid PCCI/CI concept for next-generation heavy-duty diesel engines. SAE Technical Paper 2012-01-1114; 2012.

[63] Hasegawa R, Yanagihara H. HCCI combustion in DI diesel engine. SAE Technical Paper 2003-01-0745; 2003.

[64] Kook S, Bae C. Combustion control using two-stage diesel fuel injection in a single-cylinder PCCI engine. SAE Technical Paper 2004-01-0938; 2004.

[65] Noehre C, Andersson M, Johansson B, Hultqvist A. Characterization of partially premixed combustion. SAE Technical Paper 2006-01-3412; 2006.

[66] Okude K, Mori K, Shiino S, Moriya T. Premixed compression ignition (PCI) combustion for simultaneous reduction of NO_x and soot in diesel engine. SAE Technical Paper 2004-01-1907; 2004.

[67] Iwabuchi Y, Kawai K, Shoji T, Takeda Y. Trial of new concept diesel combustion system - premixed compression-ignited combustion. SAE Technical Paper 1999-01-0185; 1999.

[68] Simescu S, Ryan TW, Neely GD, Matheaus AC, Surampudi B. Partial pre-mixed combustion with cooled and uncooled EGR in a heavy-duty diesel engine. SAE Technical Paper 2002-01-0963; 2002.

[69] Kokjohn SL, Hanson RM, Splitter DA, Reitz RD. Experiments and modeling of dual-fuel HCCI and PCCI combustion using in-cylinder fuel blending. SAE Int. J. Engines 2(2):24-39; 2009.

[70] Splitter D, Kokjohn S, Rein K, Hanson R, Sanders S, Reitz RD. An optical investigation of ignition processes in fuel reactivity controlled PCCI combustion. SAE Int. J. Engines 3(1):142-162 ; 2010.

[71] Zheng M, Kumar R. Implementation of multiple-pulse injection strategies to enhance the homogeneity for simultaneous low-NO_x and -soot diesel combustion. International Journal of Thermal Sciences. 2009;48:1829-41.

[72] Dahodwala M, Joshi S, Koehler EW, Franke M. Investigation of diesel and cng combustion in a dual fuel regime and as an enabler to achieve RCCI combustion. SAE Technical Paper 2014-01-1308; 2014.

[73] Curran S, Hanson R, Wagner R, Reitz RD. Efficiency and emissions mapping of RCCI in a light-duty diesel engine. SAE Technical Paper 2013-01-0289; 2013.

[74] Robinson K. IC engine coolant heat transfer studies (Ph.D. thesis). Bath, UK: bath University; 2001.

[75] Gamma Technologies. GT-SUITE engine performance application manual (Version 7.5). 2015.

[76] Busch S. Personal communication (Email). In: Li T, editor. 2016.

[77] H. Hiroyasu TK, M. Arai. Supplementary comments: fuel spray characterization in diesel engines. In: Mattavi J. N. ACA, editor. Combustion Modeling in Reciprocating Engines New York: Plenum Press; 1980. p. 369–408.

[78] Perini F, Dempsey A, Reitz RD, Sahoo D, Petersen B, Miles PC. A computational investigation of the effects of swirl ratio and injection pressure on mixture preparation and wall heat transfer in a light-duty diesel engine. SAE Technical Paper 2013-01-1105; 2013.

[79] Seykens XLJ Xander SLB, and Baert RSG Rik. Modelling of common rail fuel injection system and influence of fluid properties on injection process. International Conference on Vehicle Alternative Fuel Systems and Environmental Protection. Dublin, Ireland. 2014.

[80] Depcik C, Jacobs T, Hagena J, Assanis D. Instructional use of a single-zone, premixed charge, spark-ignition engine heat release simulation. International Journal of Mechanical Engineering Education. 2007;35:1-31.

[81] Woschni G. A universally applicable equation for the instantaneous heat transfer coefficient in the internal combustion engine. SAE Technical Paper 670931; 1967.

[82] Kruggel O. Calculation and measuring of piston temperatures of air-cooled two-stroke gasoline engines. SAE Technical Paper 710578; 1971.

[83] Wu H, Chiu C. A study of temperature distribution in a diesel piston - comparison of analytical and experimental results. SAE Technical Paper 861278; 1986.

[84] Chang J, Güralp O, Filipi Z, Assanis DN, Kuo T-W, Najt P, et al. New heat transfer correlation for an HCCI engine derived from measurements of instantaneous surface heat flux. SAE Technical Paper 2004-01-2996; 2004.

[85] Gingrich E, Ghandhi J, Reitz RD. Experimental investigation of piston heat transfer in a light duty engine under conventional diesel, homogeneous charge compression ignition, and reactivity controlled compression ignition combustion regimes. SAE Int. J. Engines 7(1):375-386; 2014.

[86] Chen SK, Flynn PF. Development of a single cylinder compression ignition research engine. SAE Technical Paper 650733; 1965.

[87] Pipitone E. A new simple friction model for S. I. engine. SAE Technical Paper 2009-01-1984; 2009.

[88] Hiroyasu H, Kadota T. Models for combustion and formation of nitric oxide and soot in direct injection diesel engines. SAE Technical Paper 760129; 1976.

[89] Nagle J. S-CRF. Oxidation of carbon between 1000 and 2000 C. The fifth conference on carbon;1962.

[90] Nishida K, Hiroyasu H. Simplified three-dimensional modeling of mixture formation and combustion in a D.I. diesel engine. SAE Technical Paper 890269; 1989.

[91] Li T, Caton J, Jacobs T. Use of an engine simulation to study low heat rejection (LHR) concepts in a multi-cylinder light-duty diesel engine. SAE Techncial Paper 2016-01-0668; 2016.

[92] Jaichandar S, Tamilporai P. Low heat rejection engines – An overview. SAE Technical Paper 2003-01-0405; 2003.

[93] Gatowski JA. Evaluation of a selectively-cooled single-cylinder 0.5-L diesel engine. SAE Technical Paper 900693; 1990.

[94] Fox JW, Cheng WK, Heywood JB. A model for predicting residual gas fraction in spark-ignition engines. SAE Technical Paper 931025; 1993.

[95] Senecal PK, Xin J, Reitz RD. Predictions of residual gas fraction in IC engines. SAE Technical Paper 962052; 1996.

[96] Abdul Rahim Ismail S, Rosli Abu Bakar. Valve flow discharge coefficient investigation for intake and exhaust port of four stroke diesel engines. Journal of Engineering and Applied Sciences. 2007;2:1807-11.

[97] Taymaz I. An experimental study of energy balance in low heat rejection diesel engine. Energy. 2006;31:364-71.

[98] Wallace SJ, Kremer GG. Diesel engine energy balance study operating on diesel and biodiesel fuels. In: Proceedings of ASME 2008 International Mechanical Engineering Congress and Exposition. 2008.

[99] Modi AJ. Experimental study of energy balance in thermal barrier coated diesel engine. SAE Technical Paper 2012-01-0389; 2012.

[100] Alkidas AC. The use of availability and energy balances in diesel engines. SAE Technical Paper 890822; 1989.

[101] Moore CH, Hoehne JL. Combustion chamber insulation effect on the performance of a low heat rejection Cummins V-903 engine. SAE Technical Paper 860317; 1986.

[102] Li T, Caton JA, Jacobs TJ. Energy distributions in a diesel engine using low heat rejection (LHR) concepts. Energy Conversion and Management. 2016;130:14-24.

[103] Hohenberg GF. Advanced approaches for heat transfer calculations. SAE Technical Paper 790825; 1979.

[104] Yousefzadeh A, Jahanian O. Using detailed chemical kinetics 3D-CFD model to investigate combustion phase of a CNG-HCCI engine according to control strategy requirements. Energy Conversion and Management. 2017;133:524-34.

[105] Rezaei J, Shahbakhti M, Bahri B, Aziz AA. Performance prediction of HCCI engines with oxygenated fuels using artificial neural networks. Applied Energy. 2015;138:460-73.

[106] Mack JH, Butt RH, Chen Y, Chen J-Y, Dibble RW. Experimental and numerical investigation of ion signals in boosted HCCI combustion using cesium and potassium acetate additives. Energy Conversion and Management. 2016;108:181-9.

[107] Li Y, Jia M, Chang Y, Kokjohn SL, Reitz RD. Thermodynamic energy and exergy analysis of three different engine combustion regimes. Applied Energy. 2016;180:849-58.

[108] Caton JA. Combustion phasing for maximum efficiency for conventional and high efficiency engines. Energy Conversion and Management. 2014;77:564-76.

[109] Bittle J. Insights into conventional and low temperature diesel combustion using combustion trajectory prediction model (Ph.D. thesis). College Station, TX: Texas A&M University; 2014.

[110] McBride BJ, Gordon S, Reno MA. Coefficients for calculating thermodynamic and transport properties of individual species. NASA Technical Report NASA-TM-4513, published by National Aeronaotics and Space Administration. 1993.

[111] Stivender DL. Development of a fuel-based mass emission measurement procedure. SAE Technical Paper 710604; 1971.

APPENDIX I

Model Validation for Conventional Mode

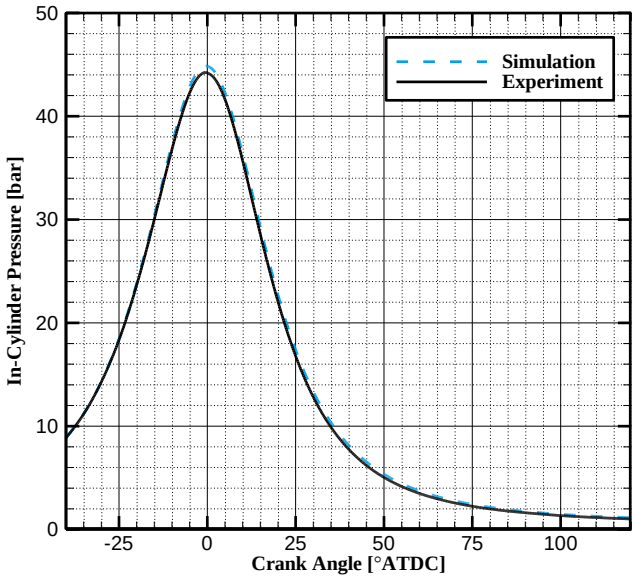

Fig. 41 Cylinder pressure comparison of motoring case at speed of 1000 rpm.

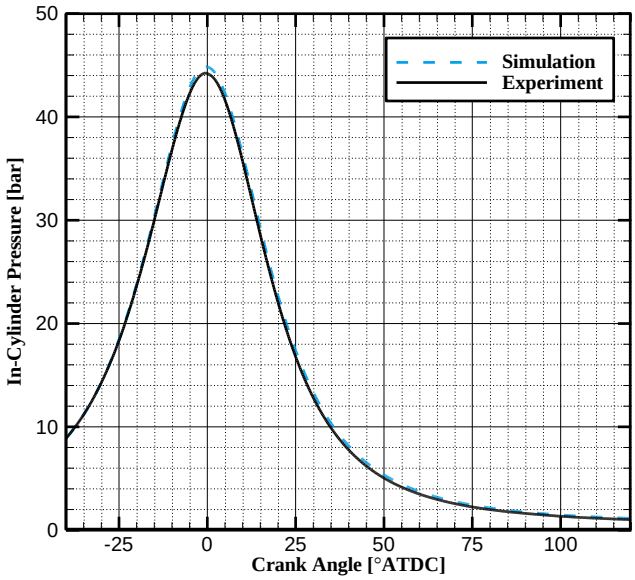

Fig. 42 Cylinder pressure comparison of motoring case at speed of 1750 rpm.

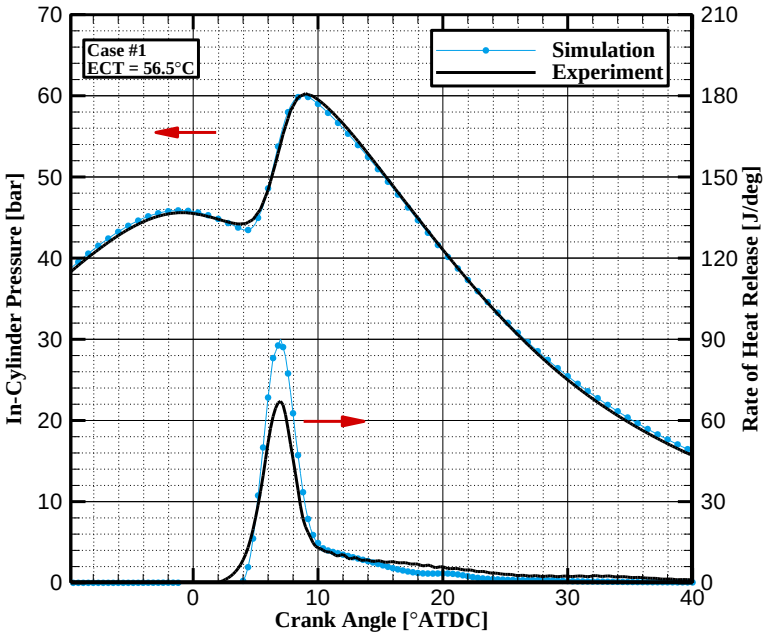

Fig. 43 Comparisons of cylinder pressure and ROHR profiles for Case #1.

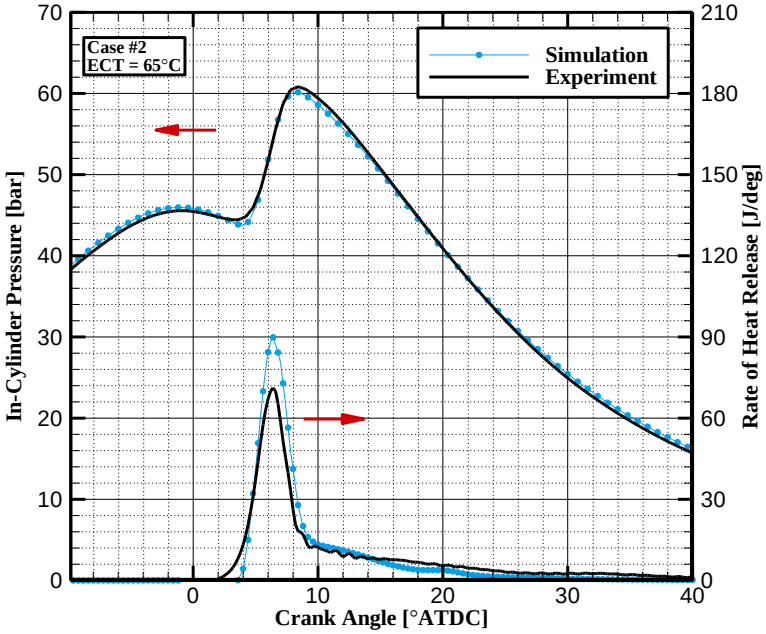

Fig. 44 Comparisons of cylinder pressure and ROHR profiles for Case #2.

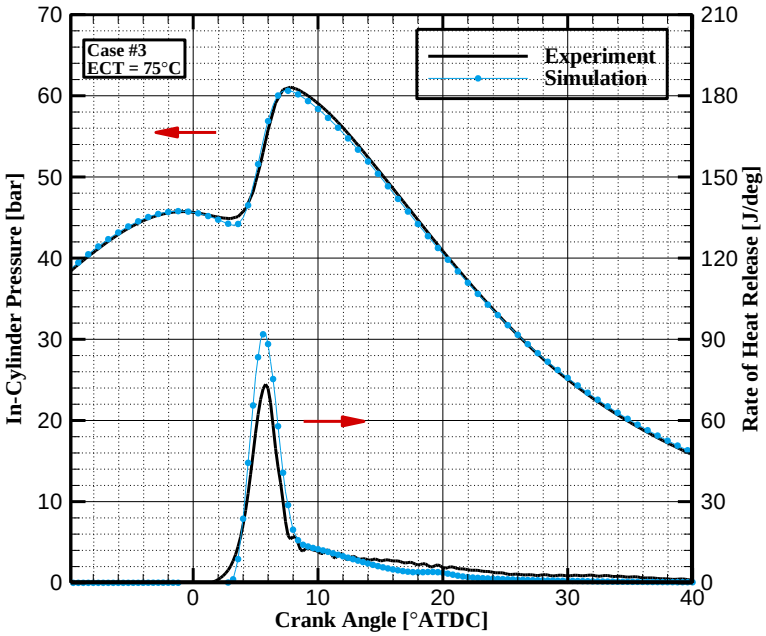

Fig. 45 Comparisons of cylinder pressure and ROHR profiles for Case #3.

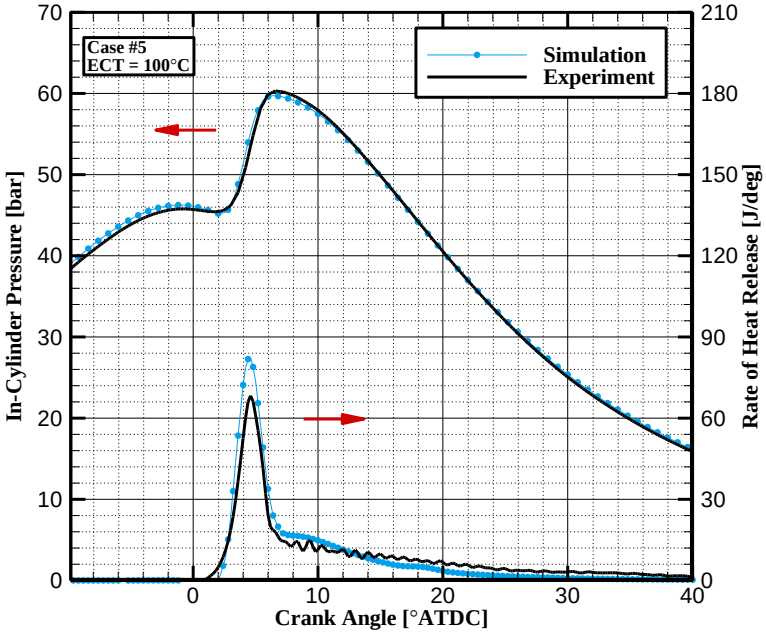

Fig. 46 Comparisons of cylinder pressure and ROHR profiles for Case #5.

APPENDIX II

Definition of RGF Model Constants

Eqs. (50) and (51) give the definitions of β_{RGF} and ω [98], respectively.

$$\beta_{RGF} = \frac{m_{f,cv} Q_{hv}}{m c_v r_c^{\gamma-1} T_1} \tag{48}$$

$$\omega = \frac{(m_f - m_{f,cv}) Q_{hv}}{m c_p r_c^{\gamma-1} T_1} \tag{49}$$

where $m_{f,cv}$ represents the mass of fuel burned during the constant volume process of an ideal dual combustion cycle; Q_{hv} is the reaction heat of fuel; m is the in-cylinder air mass; m_f is the total mass of the burned fuel; c_v and c_p are specific heats at constant volume and constant pressure, respectively. These two quantities are defined in [95] for the use of calculating the mass of burned gas from the exhaust port back to the cylinder during the valve overlap period. The physical meanings of these two quantities are not illustrated in [95], but they can be deduced from the mathematical definitions and the ideal dual combustion cycle illustrated in Fig. 47.

From the isentropic relations, the temperature at the start of constant volume process (T_2) can be determined from:

$$T_2 = T_1 \left(\frac{v_1}{v_2} \right)^{\gamma-1} = T_1 (r_c)^{\gamma-1} \tag{50}$$

where v_1 and v_2 are the specific volumes at 1 and 2, respectively. Then, it can be seen from Eq. (48) that the denominator $m c_v r_c^{\gamma-1} T_1$ represents the internal energy of the in-

cylinder air; therefore, β_{RGF} is the ratio of the burned fuel energy to the in-cylinder air energy during the constant volume process. Likewise, ω is the ratio of the burned fuel energy to in-cylinder air energy during the constant pressure process.

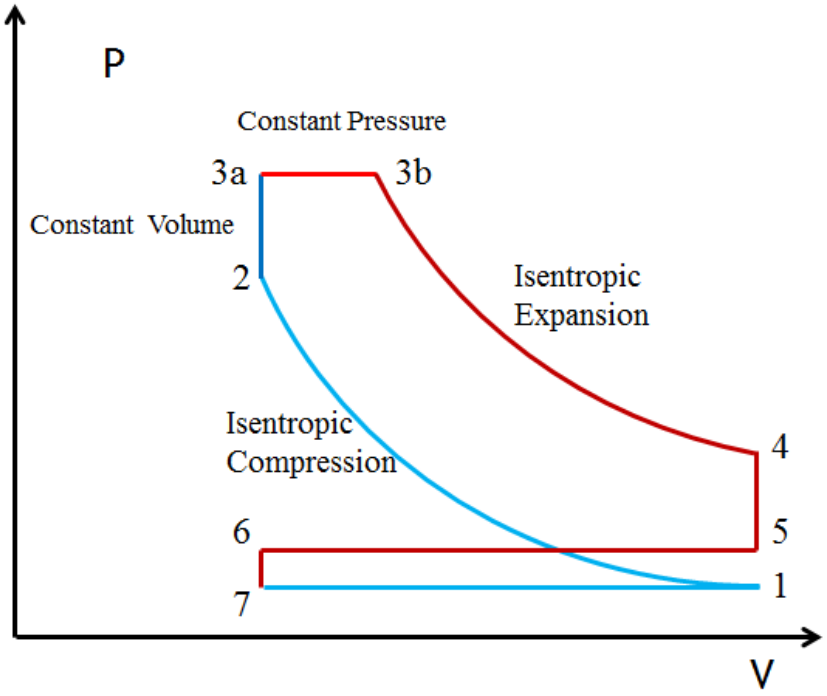

Fig. 47 Schematic of the ideal dual combustion cycle.

APPENDIX III

Energy Distributions (Conventional Mode)

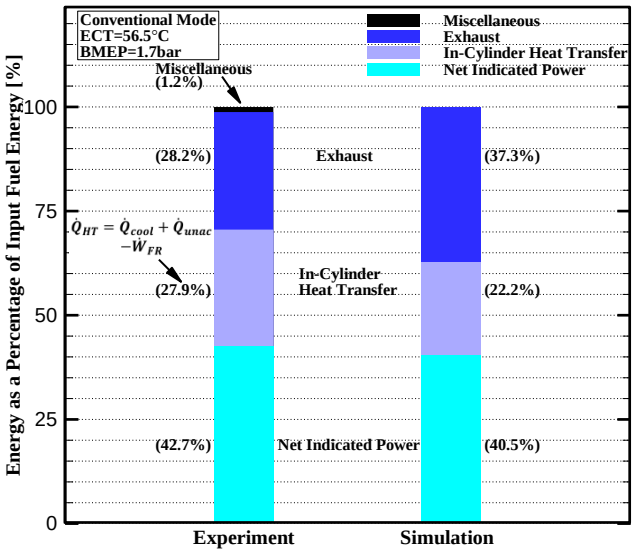

Fig. 48 Energy distributions of experiment and simulation for Case #1.

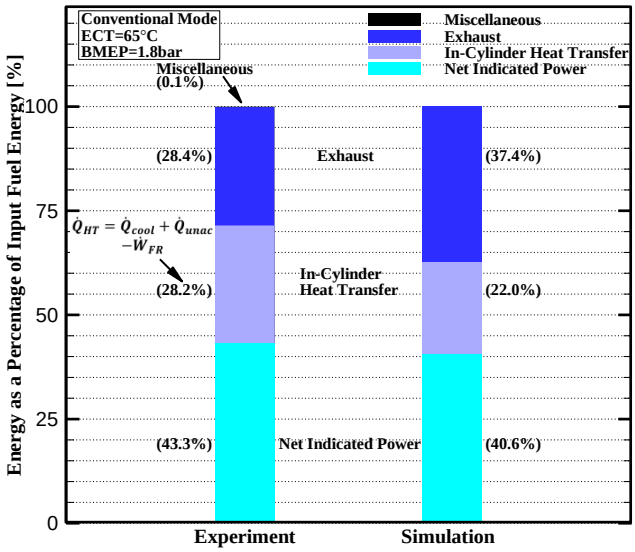

Fig. 49 Energy distributions of experiment and simulation for Case #2.

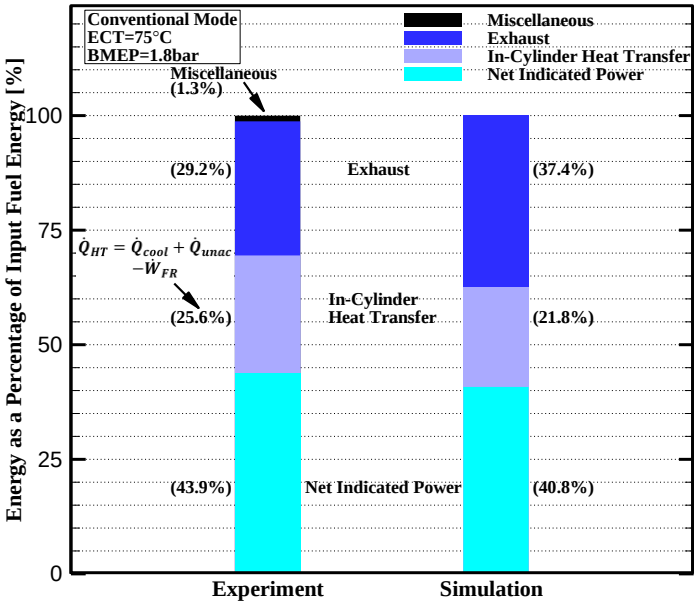

Fig. 50 Energy distributions of experiment and simulation for Case #3.

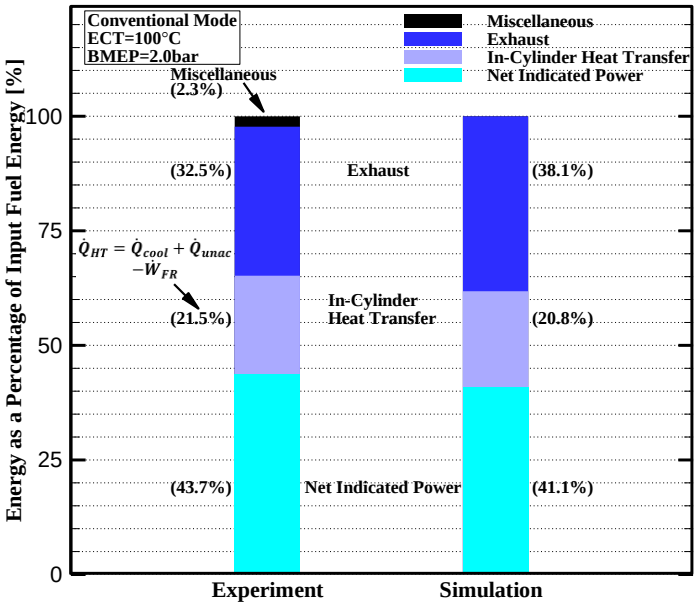

Fig. 51 Energy distributions of experiment and simulation for Case #5.

APPENDIX IV

Post-EGR Cooler Temperature Calculation

The thermodynamic model of cooled EGR/air mixing process is illustrated in Fig. 52 where each gas flow path is correspondingly labeled in Fig. 53 with cross mark.

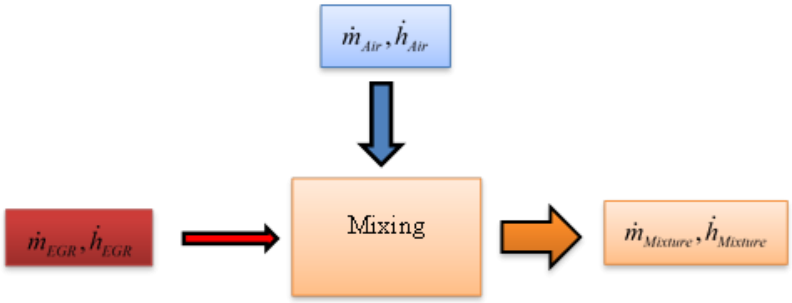

Fig. 52 Thermodynamic model of cooled EGR/air mixture.

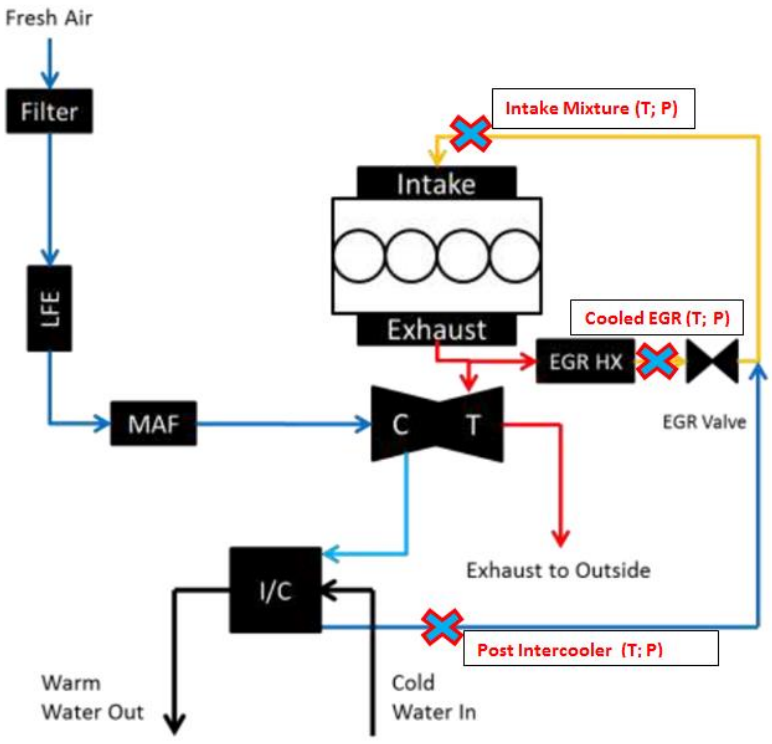

Fig. 53 Gas flow path through the engine, adapted from [109].

The freshly charged air is compressed by turbocharger and then cooled by intercooler; part of the high pressure and temperature exhaust gas is transferred from pre-turbine to EGR cooler, cooled EGR mixes with pressurized inducted air, serving as the intake mixture and being delivered into intake manifold. To back calculate the temperature of cooled EGR, energy balance analyses are developed based on the thermodynamic model shown in Fig. 52. The mass conservation is depicted as below:

$$\dot{m}_{air} + \dot{m}_{EGR} = \dot{m}_{mix} \tag{51}$$

$$\dot{m}_{EGR} / \dot{m}_{mix} = EGR\% \tag{52}$$

where the air flow rate $\dot{m}_{air}$ is measured twice by using a laminar flow element (LFE) and stock mass air flow sensor (MAF); the mass flow rate of EGR $\dot{m}_{EGR}$ can be determined from given EGR fraction. It is mentioned in Section 5 that the studied cases are operating with EGR level of around 35%, while the exact fractions for each case are not available from the recorded data sets; thus, a constant fraction of 35% is approximated for this calculation procedure.

Eqs. (53) through (55) describe the energy conservation of this mixing process, heat losses through pipes, kinetic energy and elevation difference were neglected because the mixing process is considered to be quick; and these terms are insignificant as compared to be enthalpy.

$$\dot{m}_{air} h_{air} + \dot{m}_{EGR} h_{EGR} = \dot{m}_{mix} h_{mix} \tag{53}$$

$$h_{mix} = \frac{1}{MW_{mix}} \sum_{i=1}^{mix} Y_i \overline{h_i} \tag{54}$$

$$h_i = \frac{\bar{h}_i}{MW_i} \tag{55}$$

It can be seen from Eq. (53) that h_{EGR} is the critical element that correlates with the temperature of cooled EGR. The temperatures of fresh air and intake mixture are measured and defined as "post intercooler" temperature and "intake manifold" temperature in the original data sets. The mass flow rates of three gas flows are known from mass conservation. Then, the objective of this calculation procedure is namely looking for the temperature of cooled EGR that can satisfy the energy balance shown by Eq. (53).

The enthalpy of each gas flow is calculated based on the concentrations of constituent species and their enthalpies at that particular flow temperature, as shown in Eqn. (54). Y_i and $\bar{h}_i$ are the molar fraction and enthalpy of each species, respectively; MW_{mix} is the molecular weight of the mixture. Eq. (55) shows how the molar enthalpy of a constituent gas is converted to its mass basis counterpart. The following sections will detail the enthalpy calculations of each gas flow.

i. Fresh Air

Likewise, the air enthalpy can be calculated from what shown in Ens. (54) and (55). Air is known mixture of numerous gases with disparate properties; to simplify the calculation, it is assumed to consist of 76.7% (mass) N_2 and 23.3% (mass) O_2. For better accuracy in estimation of the constituent enthalpies, the NASA Glenn polynomials are used, as it is shown in Eq. (56).

$$\bar{h}_i^0(T) = RT\left[a_1 + \frac{a_2 T}{2} + \frac{a_3 T^2}{3} + \frac{a_4 T^3}{4} + \frac{a_5 T^4}{5} + \frac{a_6}{T}\right] \tag{56}$$

R and T are the universal gas constant and bulk gas (or air) temperature; coefficients $a_1 - a_6$ are the least-squares fit constants specified by the NASA Glenn Research Center [110], the values for different species are listed in Table 10. It should be noted that $\bar{h}_i^0(T)$ is calculated on mole basis, which is the enthalpy accounts for both the enthalpy of formation and sensible enthalpy change. To maintain the reference temperature consistent to the experimental study, all the gas enthalpies are referenced to 298 K by using the following:

$$\bar{h}_i(T) = \bar{h}_i^0(T) - \bar{h}_i^0(298K) \tag{57}$$

where $\bar{h}_i^0(298)$ is the molar enthalpy at 298 K. With measured temperature and known mass concentrations of constitutive gases, the enthalpy of fresh air is determined.

Table 10 Numerical coefficients of NASA Glenn Polynomials [110]

Species	a_1	a_2	a_3	a_4	a_5	a_6	Enthalpy of formation (kJ/kmol)
O	3.58E+00	–6.10E-04	1.02E-06	9.07E-10	–9.04E-13	–1.43E+04	–1.11E+05
CO_2	2.36E+00	8.98E-03	–7.12E-06	2.46E-09	–1.44E-13	–4.83E+04	–3.94E+05
O_2	3.78E+00	–3.00E-03	9.85E-06	–9.68E-09	3.24E-12	–1.06E+03	0.00E+00
THC	9.34E-01	2.64E-02	6.11E-06	–2.20E-08	9.51E-12	–1.40E+04	–1.04E+05
NO_x	3.94E+00	–1.58E-03	1.67E-05	–2.05E-08	7.84E-12	2.90E+03	3.32E+04
H_2O	4.20E+00	–2.03E-03	6.52E-06	–5.49E-09	1.77E-12	–3.03E+04	–2.42E+05
N_2	3.30E+00	1.41E-03	–3.96E-06	5.64E-09	2.45E-12	–1.02E+03	0.00E+00

ii. Cooled EGR

The compositions of exhaust gas and corresponding concentrations are known from the measurements. Similar to the fresh air, the enthalpy of the exhaust mixture is calculated using the procedure detailed above. However, the concentrations of some species are measured on a dehumidified (dry) basis due to water vapor interacting with the measurement techniques. As a result, those measurements need to be first converted to a wet basis.

$$Y_{i,wet} = (1 - Y_{H_2O}) Y_{i,dry} \tag{58}$$

Water concentration in the exhaust is not directly measured; instead, it is estimated from the equilibrium state of the water-gas shift reaction:

$$CO_2 + H_2 \leftrightarrow CO + H_2O \tag{59}$$

Based on the empirical equilibrium constant recommended by Stivender [111], the molar fraction of water vapor can be determined from Eq. (60).

$$Y_{H_2O} = \frac{Y_{CO} + Y_{CO_2}}{2r_{H/C}\left(1 + \frac{Y_{CO}}{K \cdot Y_{CO_2}}\right) + Y_{CO} + Y_{CO_2}} \tag{60}$$

where $r_{H/C}$ is the molar hydrogen-carbon ratio of the fuel, which is 23/12 for Diesel #2 under this study; Y_{CO} and Y_{CO_2} are the molar fractions of CO and CO_2 measured on dry basis, respectively. The following calculation process is similar to fresh air; the difference from calculating air enthalpy is the temperature of cooled EGR is unknown here, consequently an initial guess of the temperature is required to input into the calculation routine and further adjusted until the energy balance, Eq. (53), is satisfied

within an acceptable accuracy, which is set to be 10^{-5} in this work. In addition, to properly account for the energy still available in the exhaust, the heat of combustion need to be added for CO and unburned HC emissions, which have not been completely oxidized. For these species, Eq. (57) is modified to be:

$$\bar{h}_i(T) = \bar{h}_i^0(T) - \bar{h}_i^0(298K) + \Delta\bar{h}_{i,c}^0 \tag{61}$$

where $\Delta\bar{h}_{i,c}^0$ is the heat of combustion of species.

iii. Intake EGR/Air Mixture

Calculating the enthalpy of the mixture gas flow is the most complicated since the intake mixture consists of numerous species and their concentrations are unknown. As a result, the compositions of intake mixture are considered to be same as that of EGR; however, the concentrations of each species will be different.

To obtain the mass/molar fractions of each species in the intake mixture, the molar concentration of CO_2 in the mixture needs to be first determined. Typically, the molar fraction of CO_2 are measured downstream of the mixing of cooled EGR and fresh air to establish the dilution ratio, namely the EGR fraction; though this measurement is not recorded in the test data sets, which can be back calculated with the approximation of 35% EGR level. The procedure can be illustrated using the relations shown in Eqs. (62)–(64).

$$X_{i,intake} = \frac{Y_{CO_2,intake}}{Y_{CO_2,exhaust}}\left(X_{i,exhaust}\right) \tag{62}$$

$$X_{i,exhaust} = \frac{Y_{i,exhaust} MW_i}{MW_{mix,exhaust}} \tag{63}$$

$$EGR\% = \sum X_{i,intake} \tag{64}$$

The measured concentrations of each species in the exhaust give the corresponding mass fractions with Eq. (63). The initial guess of molar fraction of CO_2 in the intake mixture is input into the calculation routine to obtain the mass fractions of constituent gases of the intake mixture based on Eq. (62), and the guess value is gradually adjusted until the EGR fraction calculated using Eq. (64) reaches 35%. Then, the concentrations of constituent gases are ready for calculating the mixture enthalpy. The entire process of back-calculating cooled EGR temperature is illustrated using a flow diagram, as shown in Fig. 54.

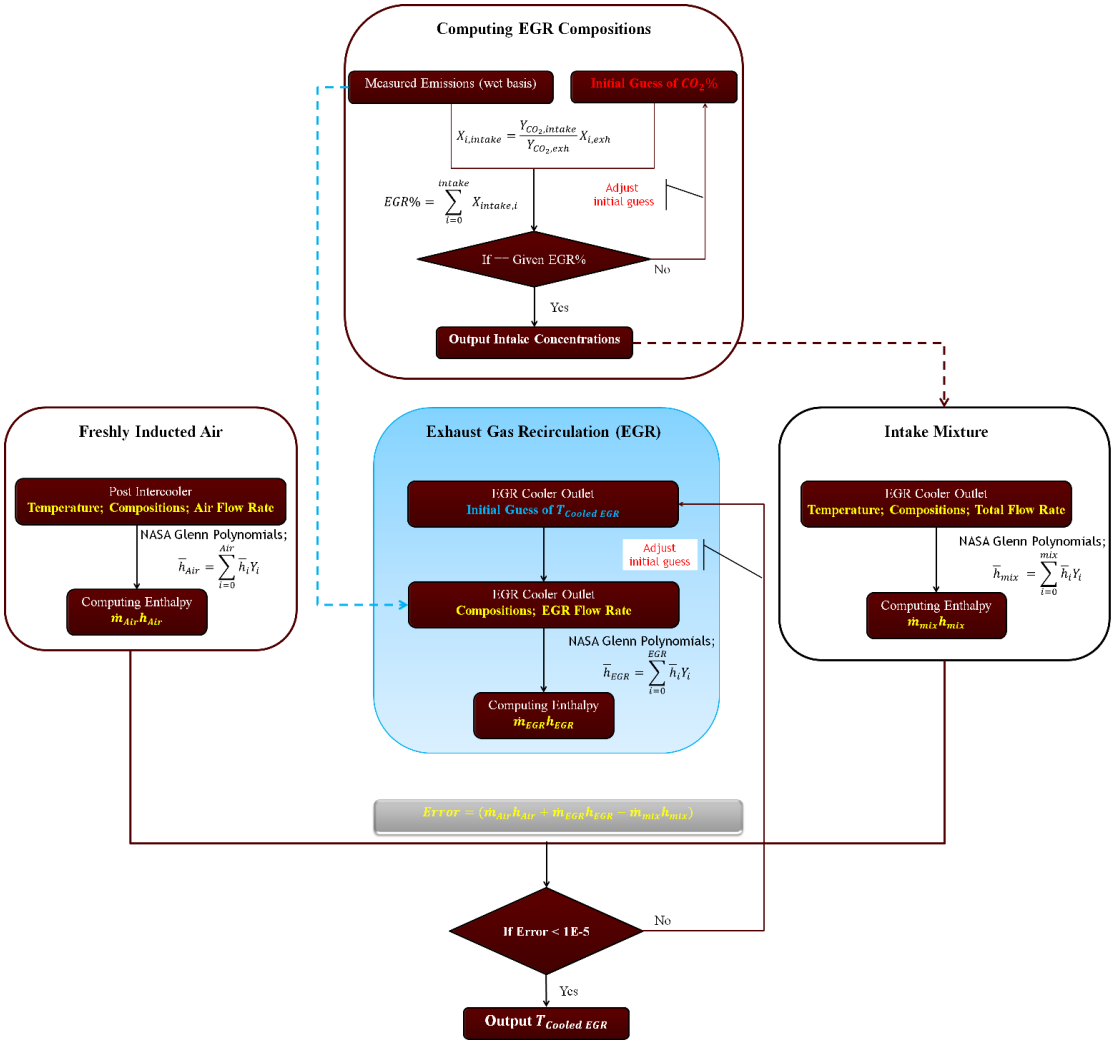

Fig. 54 Flow diagram for the computation of cooled EGR temperature.

APPENDIX V

Model Validation for LTC Mode

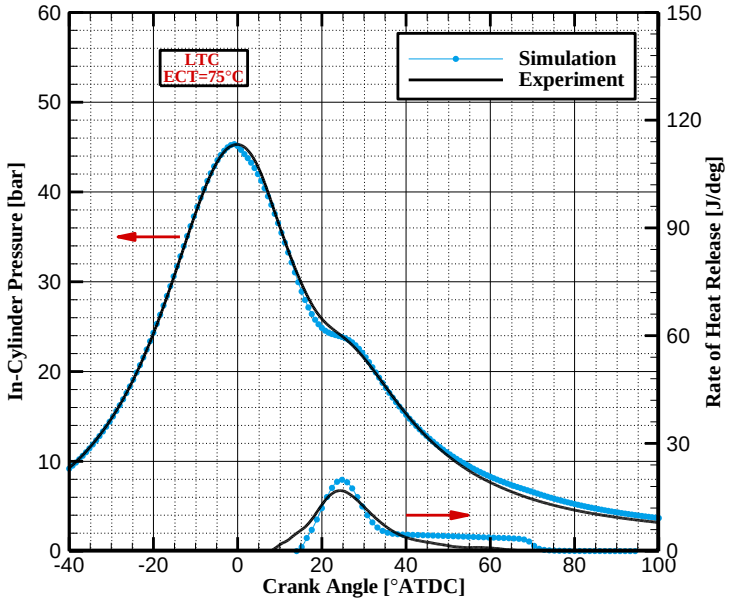

Fig. 55 Comparisons of cylinder pressure and ROHR for Case #6.

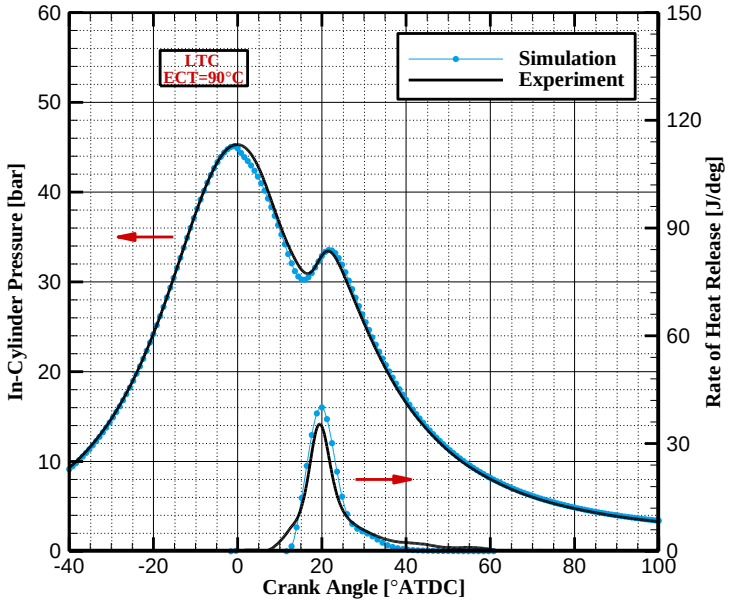

Fig. 56 Comparisons of cylinder pressure and ROHR for Case #8.

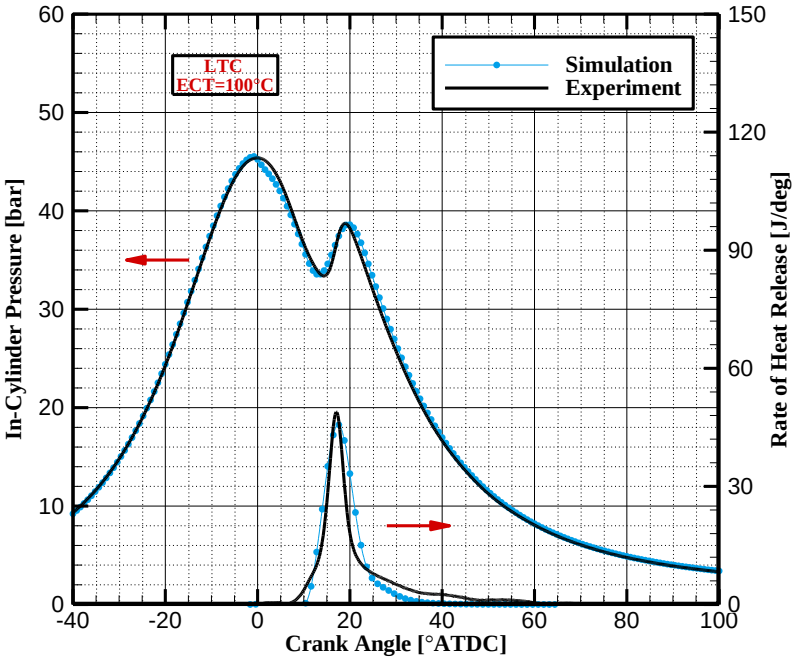

Fig. 57 Comparisons of cylinder pressure and ROHR for Case #10.